Compound Meta-optics for Complete Wavefront Control

By

Hanyu Zheng

Dissertation

Submitted to the Faculty of the

Graduate School of Vanderbilt University

in partial fulfillment of the requirements

for the degree of

DOCTOR OF PHILOSOPHY

in

Electrical Engineering

May 12, 2023

Nashville, Tennessee

Approved:

Jason G. Valentine, Ph.D.

Joshua Caldwell, Ph.D.

Sharon M. Weiss, Ph.D.

Justus Ndukaife, Ph.D.

Yuankai Huo, Ph.D.

To my beloved mom and dad.

ACKNOWLEDGEMENTS

Vanderbilt University has been a special place for me in the past five years when I pursued a Ph.D. in electrical engineering. I would like to express my heartfelt gratitude to this place for providing me with an exceptional educational experience. The resources and opportunities available at this prestigious campus have significantly impacted my current achievements and shaped me into the present person. This fantastic platform also offers me a balanced work-life environment so that I can conduct my research readily.

I would like to thank my Ph.D. advisor, Dr. Jason Valentine, one of the most intelligent scientists I have ever met, who offered me the opportunity to research at Vanderbilt. During my Ph.D. career, Dr. Valentine inspired me a lot, not only in conducting hands-on experiments but also the critical thinking to be an independent investigator. Through weekly discussions with Dr. Valentine, I developed solid research skills and visionary ideas so that we can always conduct projects at the frontiers of metasurface realms. Besides, Dr. Valentine is also extremely helpful to my academic career and supports me in attending major conferences to build networks with peers. I learned a lot from his scientific skills and personality that shaped me into the person I would like to be as an academic researcher.

I would also like to thank Dr. Jousha Caldwell, Dr. Sharon Weiss, Dr. Justus Ndukaife, and Dr. Yuankai Huo, who served as my committee members and supported me during my research projects. Thanks to their helpful feedback, my Ph.D. dissertation has become more solid and comprehensive. I benefited greatly through communications with them over the past five years. From the classes of Dr. Weiss and Dr. Ndukaife, I built up the fundamentals of photonics, which assisted me in further understanding my research projects. I also learned a lot from collaborating with Dr. Caldwell and Dr. Huo, as we proposed many frontiered research projects together.

I want to thank our research collaborators, Dr. Anthony Grbic and Dr. Brian O. Raeker from Michigan University. Thanks for your diligent effort in the compound meta-optic research. The collaboration inspired me a lot so that I could build basic concepts and experimental skills around compound meta-optic devices. I also want to thank Mingze He and Quan Liu from Vanderbilt University, who shared plenty of ideas from the computer science aspects so that we could readily develop the optimization platform.

Besides, I would like to thank my labmates in Dr. Valentine's group. Your optimism toward research and life encourages me a lot so that I can enjoy my Ph.D. career. Specifically, I want to thank You Zhou, a visionary and intelligent person mentoring me at the beginning of my Ph.D. who can always generate great ideas during our discussions. I also want to thank Chibuzor Fabian Ugwu, Elena Kovalik, Janna Eaves, Scott Criswell, Brandon Swartz, Andrew Du, and Xiaomeng Zhang. I learned a lot while working with you, not only in research but also in our friendly communications about daily life. I want to offer special thanks to Tao Hong, who taught me solid fishing skills. Hope you can catch the dream fish very soon.

Moreover, I want to thank the staff in the VINSE family. I want to thank Kurt Heinrich, William Martinez, Alice Leach, Benjamin W. Schmidt, Christina L. McGahan, James R. McBride, Dmitry S. Koktysh, and Megan K. Dernberger. Thank you for your strong technical support during my research so I could finish my experiments smoothly. I also want to thank Sarah Ross, Jamie L. Kuntz, Daniel Myrtles, and Cassidy Slabaugh for their exceptional administrative support, including filling out the purchase order and scheduling the events.

Lastly, I want to thank my family members, my mon, my dad, my girlfriend Lexi, and my kittens, Iri and Luna. Thank you for your tolerance and patience with me. I cannot finish my Ph.D. without your support. You are the most valuable treasure in my life.

TABLE OF CONTENTS

LIST OF TABLES

Table **Page**

LIST OF FIGURES

Figure **Page**

LIST OF ABBREVIATIONS

α-Si	Amorphous Silicon
Al_2O_3	Aluminum Oxide
CCD	Charge-coupled Device
CNNs	Convolutional Neural Networks
Cr	Chromium
CV	Coefficient of Variation
DI	Deionized
DMD	Digital Micromirror Device
DNA	Deoxyribonucleic Acid
DNNs	Deep Neural Networks
DOF	Degree of Freedom
DUV	Deep Ultraviolet
EBL	Electronic Beam Lithography
FLOPs	Floating Point Operations
FOV	Field of View
FWHM	Full Width at Half Maximum
GDSII	Graphic Data System 2
GS	Gerchberg-Saxton
HCTAs	High-contrast Transmit-arrays
InGaAs	Indium Gallium Arsenide
LCP	Lefthand-circular-polarized
LP	Linear Polarized

LPCVD	Low-pressure Chemical Vapor Deposition
MNIST	Modified National Institute of Standards and Technology database
MSE	Mean Square Error
NA	Numerical Aperture
NIR	Near-infrared
NNs	Near Infrared
PDMS	Polydimethylsiloxane
PECVD	Plasma Enhanced Chemical Vapor Deposition
PMMA	Polymethyl Methacrylate
RCP	Righthand-circular-polarized
RCWA	Rigorous Coupled Wave Analysis
ReLU	Rectified Linear Unit
RGB	Red Green Blue
RIE	Reactive Ion Etching
SDM	Spatial Division Multiplexing
SEM	Scanning Electron Microscope
SGD	Stochastic Gradient Descent
SLM	Spatial Light Modulator
Si	Silicon
Si_3N_4	Silicon Nitride
SiO_2	Silicon Dioxide
TE	Transverse Electric
TM	Transverse Magnetic

THz	Terahertz
TiO_2	Titanium Dioxide
UP	Unpolarized
USAF	U.S. Air Force
UV	Ultraviolet
VINSE	Vanderbilt Institute of Nanoscale Science and Engineering
VO_2	Vanadium Dioxide

LIST OF PUBLICATIONS

(1) **Zheng H**, He M, Zhou Y, Kravchenko II, Caldwell JD, Valentine JG. Compound Meta-Optics for Complete and Loss-Less Field Control. ACS nano. 2022 Aug 26;16(9):15100-7.

(2) **Zheng H**, Liu Q, Zhou Y, Kravchenko II, Huo Y, Valentine J. Meta-optic accelerators for object classifiers. Science Advances. 2022 Jul 27;8(30):eabo6410.

(3) Raeker BO, **Zheng H**, Zhou Y, Kravchenko II, Valentine J, Grbic A. All-Dielectric Meta-Optics for High-Efficiency Independent Amplitude and Phase Manipulation. Advanced Photonics Research. 2022 Mar;3(3):2100285.

(4) **Zheng H**, Zhou Y, Ugwu CF, Du A, Kravchenko II, Valentine JG. Large-scale metasurfaces based on grayscale nanosphere lithography. ACS Photonics. 2021 Jun 1;8(6):1824-31.

(5) Zhou Y, **Zheng H**, Kravchenko II, Valentine J. Flat optics for image differentiation. Nature Photonics. 2020 May;14(5):316-23.

Chapter 1

Introduction

1.1 Origins of Metasurfaces

Electromagnetic metamaterials are artificially manufactured structures with the prefix "meta" arising from the Greek word meaning "beyond". Hence, a metamaterial possesses optical properties unattainable in natural environments, such as negative refractive index[1, 2, 3, 4], epsilon-near-zero[5, 6, 7], and ultra-high index[8]. The optical response of metamaterials is dictated by the geometry of the unit cells, or meta-atoms, and have been employed for various uses, including the perfect lens[9], cloaking[10, 11], and helicity filtering[12, 13]. However, due to the complexity of 3-dimensional structures, the absence of a cost-effective manufacturing method as well as a solid design methodology hinders further applications for metamaterials. In this case, development in novel physics theories and hardware platforms are needed for achieving more advanced functions at optical wavelengths.

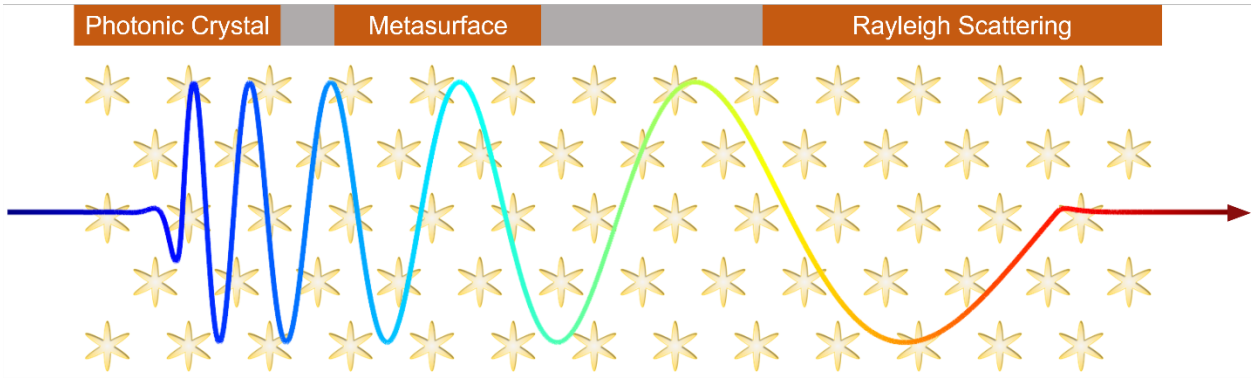

Figure 1.1 Schematics of photonic feature size and interacting wavelength. The hexagram means artificially fabricated unit cells.

Complete monochromatic field control is enabled by independent manipulation of the amplitude, phase, and polarization state of light, which is needed for a wide variety of scientific and industrial applications and generally requires multiple conventional optical elements such as lenses, polarizers, and amplitude masks. The need for multiple elements results in large systems that can be difficult to integrate into compact optical packages. Optical metasurfaces, a 2-dimensional version of metamaterials, as shown in Fig.1, provides a versatile platform for manipulating optical waves. Compared to metamaterials, metasurfaces offer the wave control within an ultrathin artificial layer, resulting in a compact and low-profile device mophorlogy. Such 2-dimensional architecture makes metasurface manufacturing compatible with the standard lithography technique in present semiconductor industry[14, 15, 16]. The ease of fabrication as well as the reduced design complexity could lead to metasurfaces being utilized in the next generation of high-performance integrated or portable photonic devices.

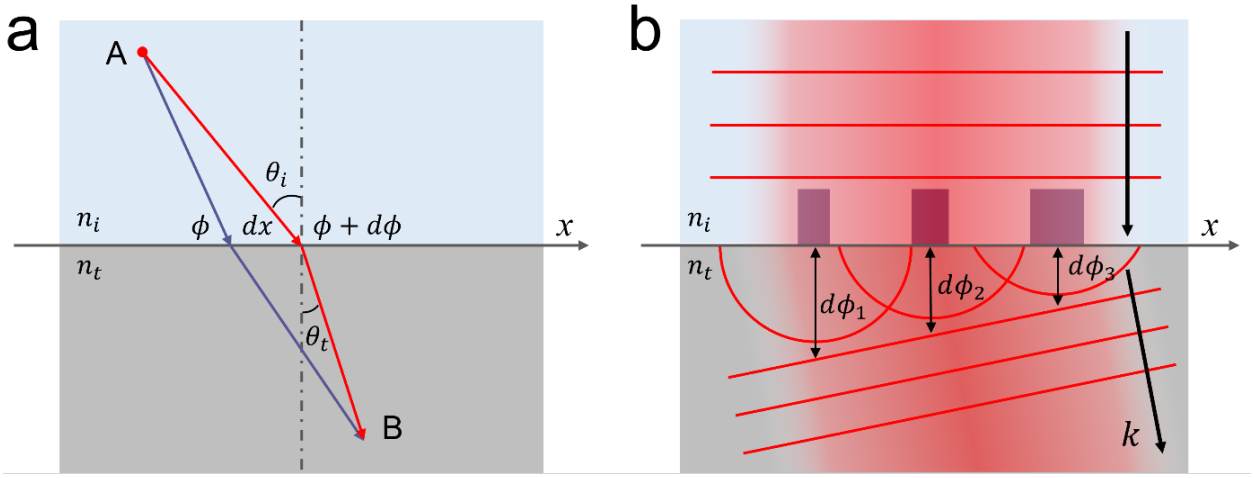

Figure 1.2 Mechanism of metasurface for wavefront control. (a) Schematics of generalized Snell's law. (b) Light control by each unit cell in metasurfaces for anomalous refraction.

The metasurface concept was first proposed to provide an abrupt phase shift within an ultra-thin layer[17], as shown in Fig.1.2 (a), and can be described by the generalized Snell's law. By

locally manipulating the metallic resonators between two uniform media, a phase discontinuity can be introduced at the interface, resulting in anomalous refraction. The generalized Snell's law can be derived from Fermat's principle and is based on the neighboring optical paths for light traveling between two points being equal. Considering the phase gradient, the analytical expression for anomalous refraction can be described by:

$$n_t \sin(\theta_t) - n_i \sin(\theta_i) = \frac{1}{k_0}\frac{d\phi}{dx} \tag{1.1}$$

where θ_i and θ_t is the incident and transmit angle, n_i and n_t is the refractive index of uniform medium labeled in Fig.1.2 (a), k_0 is the wavenumber in vacuum, and $d\phi/dx$ is the phase gradient introduced by metasurface.

The phase gradient in generalized Snell's law can be engineered by locally exciting various meta-atoms as shown in Fig.1.2 (b). Each meta-atom can be considered an independent point source, emitting a secondary wavefront with the phase-delay dictated by the geometry. Wavefront shaping is achieved by designing the geometry and layout of all the meta-atoms in the metasurface. At an early stage of metasurfaces, the phase control mechanism was based on the excitation of two modes in V-shape metallic resonators[17], leading to a 2π phase manipulation range for mid-infrared light. However, the intrinsic Ohmic loss of metals in the optical spectrum significantly deteriorates the performance of metasurface devices, hindering further applications. Such flaws will be further amplified under the resonance mode with field enhancement effects. In the following sections, I will introduce recently emergent low-loss dielectric metasurfaces and briefly review related applications.

1.2 Dielectric Metasurfaces for Wavefront Engineering

Due to intrinsic Ohmic loss, metallic metasurfaces are limited with reduced efficiency in

the optical region. In contrast, dielectric materials with a low extinction ratio possess explicit advantages for high-efficiency metasurface devices. In the past decades, a plethora of dielectrics have been proposed for metasurface design, including titanium dioxide (TiO_2)[18, 19, 20], silicon dioxide (SiO_2)[15], silicon nitride (Si_3N_4)[21, 22, 23], and silicon (Si)[24, 25, 26], to name a few. Dielectric-based meta-atoms provide a refractive index contrast with the surroundings, resulting in a resonance or waveguide mode for phase manipulation with high transmission.

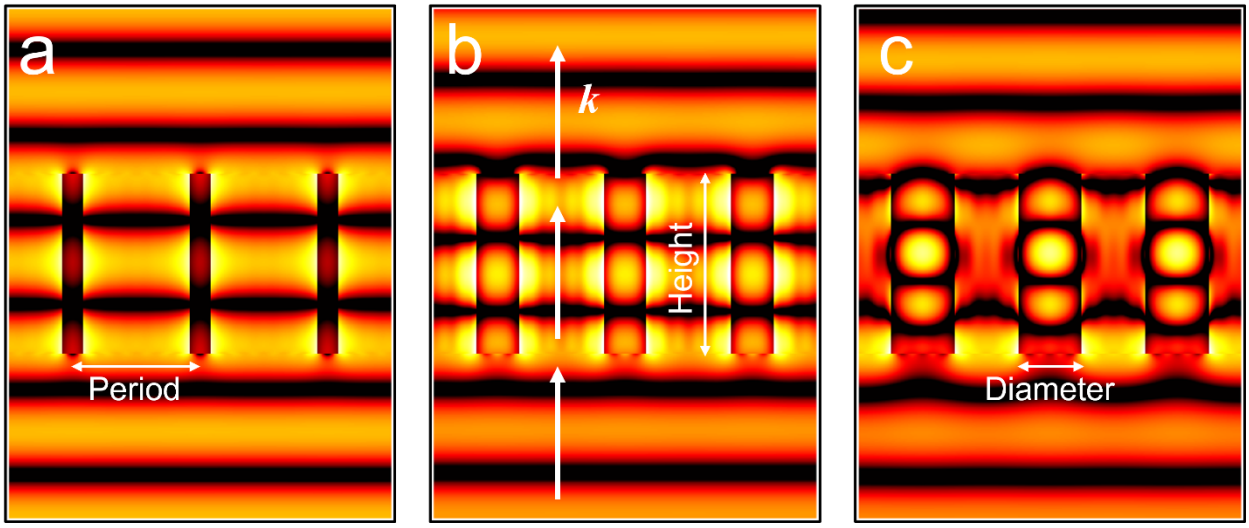

Figure 1.3 Electrical field map of periodic metasurfaces for phase manipulation. The simulated wavefront shows different phase responses under plane-wave illumination dictated by the diameters of silicon-based nanopillars. The period is fixed at 0.5λ, Height is 0.7λ and diameter is controlled at (a) 0.08λ, (b) 0.16λ and (c) 0.24λ, respectively. All metasurfaces are embraced in a polymer surrounding environment with an index of 1.48.

Huygens metasurfaces arising from Mie resonance were first proposed[27] in 2014 based on dielectrics. The corresponding meta-atoms comprise Si nanopillars and support magnetic and electric resonance modes. By varying the aspect ratio of the meta-atoms, two resonance modes will overlap, resulting in a Huygens mode with high transmission as well as 2π phase shift. Although a Huygens metasurface can provide near-unity transmission and phase control, there are still drawbacks. First, the optical response of Huygens metasurfaces is sensitive to the incident angle, leading to the devices generally working under the paraxial approximation. Second,

Huygens metasurfaces are based on Mie resonance, which has a high-quality factor that is sensitive to the geometry variation. Hence, such devices are also sensitive to fabrication errors, resulting in challenging manufacturing in the visible spectrum.

Instead of using Mie resonances to provide wavefront control, another choice is to utilize high-contrast transmit-arrays (HCTAs)[28, 29, 30] composed of dielectric nanopillars. Each nanopillar is considered as a truncated waveguide, offering control over the phase delay. In this scenario, the meta-atoms have a high aspect ratio to prevent strong resonances so as to enhance the device tolerance to fabrication error. Fig.1.3 demonstrates wavefront control using silicon nanopillars with various diameters, where periodic boundary conditions are applied during simulation. Due to the high refractive index contrast between silicon and surrounding media, the diameter of the nanopillars will affect the group velocity of light guided in the unit cell, hence the phase response of transmitted light. To be specific, a larger diameter leads to lower group velocity as well as a more delayed phase response. Moreover, since the waveguide can be considered as a weak resonator, such a solution has superior fabrication tolerance as well as broadband performance[31]. As a result, HCTAs have been proved as a promising platform for high-efficiency metasurface devices. This has been shown through a variety of devices, including flat lenses[18, 32], beam-splitters[33, 34, 35, 36], holograms[37, 38, 39, 40, 41], augmented reality displays[42, 43], high-definition displays[44, 45], image differentiation[46, 47, 48], and compact optical spectrometers[49, 50].

1.3 Design Strategy of Metasurfaces

During the metasurfaces design process, a local approximation is applied so that each meta-atom is assumed to be non/weakly coupled. In this case, a single meta-atom becomes a secondary point source for the subsequent wavefront and is independent of each other. A metasurface with a specified function is achieved by a meta-atom array, where meta-atoms are assigned various

geometrical parameters as a function of position.

In order to form a metasurface, a data library of meta-atoms, including geometries with corresponding delayed phase, $\Phi(g_1, g_2, \cdots)$, will be generated by full-wave simulations. Here, phase, Φ, is a function of geometrical parameters, g_i. Meanwhile, a phase profile $\phi(x)$ for metasurfaces is designed in terms of position, x, based on the target function. The metasurface is then accomplished by a global search in the data library at each designated position, where a loss function defined by $L(x) = |\phi(x) - \Phi|^2$ is minimized. The global search will convert the target phase profile, $\phi(x)$, into a series of geometrical parameters in terms of position, x, which is utilized for fabrication.

Another important parameter for metasurface design is the period, P, of each unit cell. The lower limit for P is dictated by the fabrication resolution of meta-atoms. In most cases, the period should be large enough to avoid coupling effects between the neighboring meta-atoms. On the other hand, the upper limit of P is determined by the Nyquist sampling criterion. In general, consider a target phase profile, $\phi(x)$, the period should obey the following sampling rule:

$$\max\left(\frac{d\phi}{dx}\right) \cdot P \leq \pi \tag{1.1}$$

A detailed derivative process can be found in the Appendix A.1. Meanwhile, to suppress higher diffraction orders from the periodic structure, the period is limited by the following equation:

$$P < \frac{\lambda}{n} \tag{1.2}$$

where n is the refractive index of surrounding environments.

A designed meta-grating is exhibited in Fig.1.4, where the period of the meta-atoms is chosen as $\lambda/2$. Each meta-atom can introduce a specified phase control as shown in Fig.1.4 (a). With a certain layout, the meta-grating can deflect the incident wave to a different angle. The full-

wave simulation for the entire structure is demonstrated in Fig.1.4 (b), matching well with the theoretical prediction. The tiny perturbations of the wavefront are generally introduced by the weak coupling effects between the neighboring meta-atoms, which arise from the broken periodic boundary conditions in the metasurface devices. These perturbations can be further optimized by more advanced design strategies, such as inverse design[51, 52, 53, 54, 55] based on machine learning or the adjoint method.

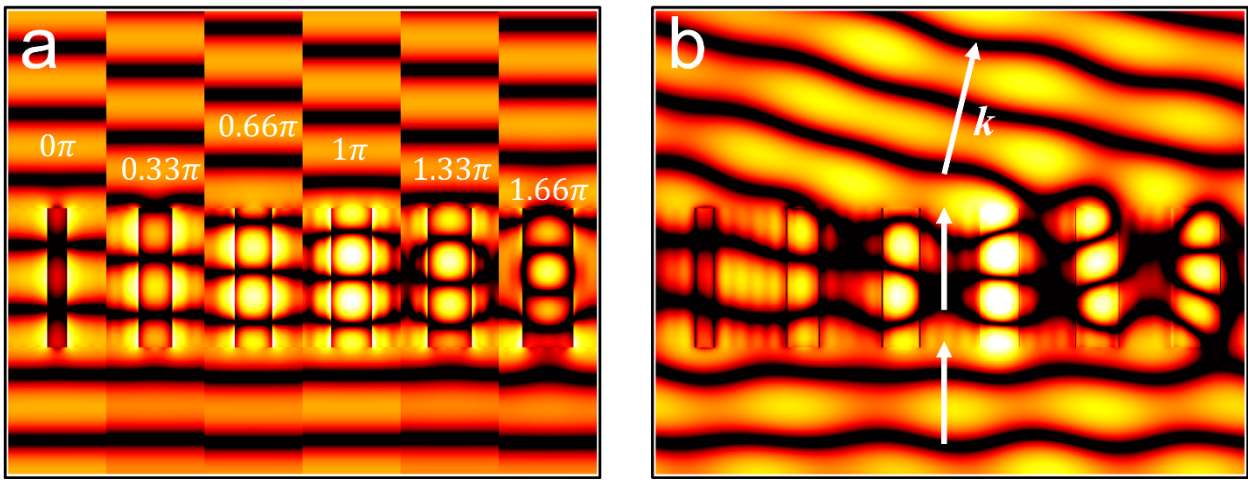

Figure 1.4 Electrical field map of metasurfaces for anomalous refraction. (a) The schematic of a period of metasurface for anomalous refraction. The period includes six different meta-atoms. Each is independent and chosen from a prior data library with designed phase responses as labeled. (b) A full wave simulation based on the structure in (a) indicates an anomalous refraction behavior under plane-wave illumination.

1.4 Meta-optic-based Applications

In the past decades, various metasurface-based applications have been demonstrated as counterparts or extensions of conventional optics. One of the most visible applications is the emergence of the metasurface-based diffractive lenses[18, 31], also named metalenses. Compared to conventional lenses, metalenses have several advantages. First, due to the ultra-low-profile metalenses can be readily integrated with other optoelectronic devices while significantly reducing the form factor of the entire system. Particularly, the numerical aperture (NA) of metalenses are

irrelevant to the device thickness, so a high NA lens can be readily manufactured within a compact volume. A metalens with the numerical aperture as high as 0.8 was reported[18] in 2015, with a device efficiency of 86% and performance comparable with the objective formed by conventional optics. However, as a conventional lens with a free-form profile, the phase profile is defined by the accumulated phase difference during light propagation. Large NA can only be achieved by raising the lens thickness or combining multiple lenses, resulting in a bulky optical system. Second, a conventional lens is generally fabricated by diamond turning or a mold polishing technique, which is challenging for optical surfaces with large curvature and high accuracy requirements. In contrast, metasurface fabrication is compatible with standard semiconductor manufacturing platforms with nm-scale fabrication resolution. The well-defined meta-atoms providing a highly accurate phase profile can effectively avoid the spherical aberrations of conventional optics.

Nevertheless, as a diffractive optic, a metalens has other inevitable drawbacks hindering commercial applications. First, a metalens is typically designed at a single working wavelength. Due to the non/weekly resonant meta-atoms, the phase control of metasurface remains almost constant over a broad bandwidth. However, a hyperbolic lens working at different wavelength requires distinguished phase profiles induced by dispersion, hence a metalens with a constant phase profile leads to a phase discontinuity between the neighboring phase zones, except for the designed wavelength. To compensate the phase discontinuity, one solution is to enhance the dispersion of each meta-atom by raising the aspect ratio of unit-cells[56]. Another choice is to design multiple working wavelengths instead of broadband imaging since a red-green-blue (RGB) color mixture is enough for full-color imaging applications[43]. Second, a metalens is generally fabricated by electronic beam lithography (EBL) which is a point-by-point manufacturing platform. Such technique is limited for massive production since the manufacturing time and cost is exponentially

related to the device footprint. One solution is to use projection lithography[14, 15], as is used in the semiconductor industry based on ultra-violet (UV) or deep-ultra-violet (DUV) exposure. In this case, a geometrical database including billions of unit cells needs to be compressed to a size-suitable file for machine processing. Another promising choice is to utilize a reusable template for nanoimprinting[57]. Although the hard mask for printing is fabricated by high-resolution EBL systems, the template can be recycled for massive manufacturing.

Metasurfaces can also produce arbitrary wavefronts for a wide variety of functionalities. As an example, a computer-generated phase mask can be utilized to generate a 3-dimensional hologram[40]. Although a phase-based spatial light modulator can be used for holograms, metasurfaces have subwavelength unit cells effectively avoiding higher diffraction orders and significantly increasing the quality of the hologram. Furthermore, subwavelength unit cells can also provide ultra-high field manipulation resolution and potentially large numerical aperture, which is preferred for the applications requiring high optical power and field accuracy, such as hologram-based optical tweezer[58].

In addition to phase control, one unique advantage of metasurfaces is the ability to engineer the birefringence[59], which is defined by the geometry of the meta-atoms. Birefringence is an extension of conventional optics allowing hidden information associated with polarization to be readily explored. Birefringent meta-atoms break rotational symmetry, such as the silicon cylindroid shown in Fig.1.5 (a), so that the optical response for orthogonal directions can be independently defined. Each meta-atom obeys the Jones matrix correlating the spatial phase, amplitude, and polarization states. The detailed control process can be found in Appendix A.2. By controlling the geometrical phase dictated by the rotation of meta-atoms, a polarization conversion process can be readily achieved as shown in Fig.1.5 (b) and (c), where the *x*-polarized light can be

completely converted into the y-polarizaed state. Such a phenomenon can be utilized for spatial amplitude control since the cross-polarized output light intensity obeys Malus's law that the intensity is dictated by the rotation angle, θ. Furthermore, by combing the accumulated and the geometrical phase, a fully controlled amplitude and phase response can be achieved readily. The versatile manipulation ability of metasurfaces over light properties leads to various applications such as vectorial field control[60], chiral imaging[61], dichroism plate[62], and full-stoke polarimetry[63].

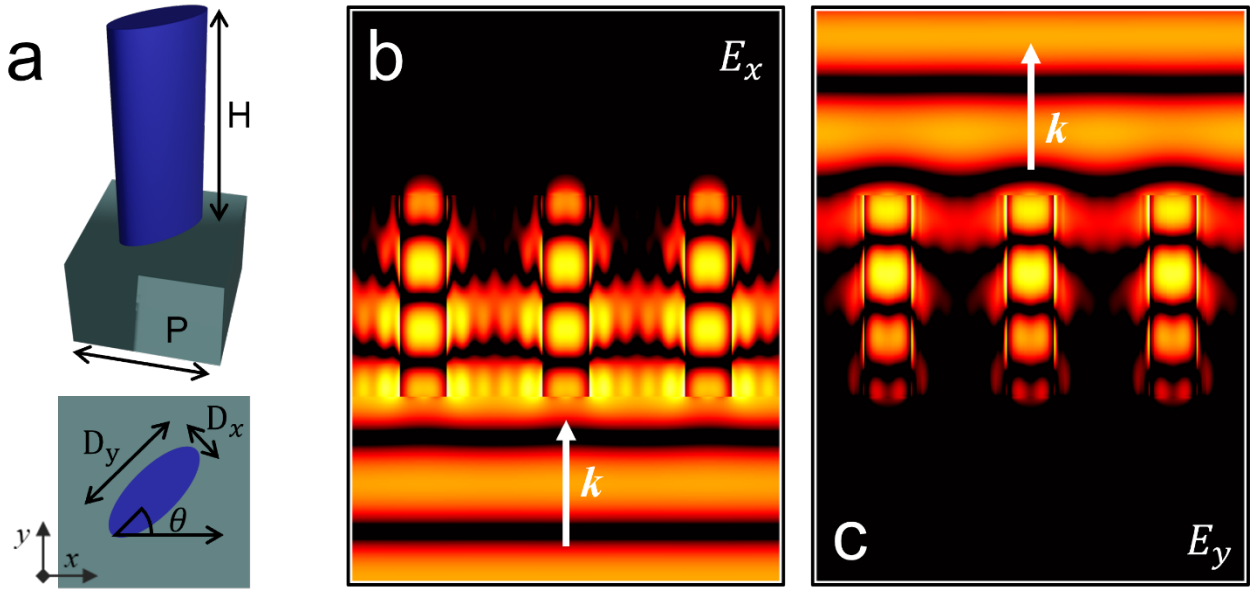

Figure 1.5 Demonstration of birefringent property of cylindroid meta-atom. (a) The geometrical schematic of meta-atom. The period is fixed at 0.5λ, Height is 0.7λ, diameters are chosen at 0.13λ and 0.32λ, respectively. The rotation angle θ is set at 45°. All metasurfaces are embraced in a polymer surrounding environment with an index of 1.48. (b) and (c) exhibit x and y polarized electrical field map, indicating a complete polarization conversion process.

1.5 Compound Meta-optic Systems

Throughout the past few decades, numerous applications based on single-layer metasurfaces have been proven, nonetheless, the capabilities are constrained by the lack of engineering degrees of freedom. In order to accommodate the additional degree of freedom (DOF) required by more complex functionalities, a compound meta-system made up of multiple metasurfaces was created. A plethora of research has recently been conducted based on compound

meta-systems for advanced functions, where the extra metasurface layers offer an optimization or a functional extension of single-layer metasurface devices. For both purposes, the compound meta-optics systems exhibit better performance while still maintaining a compact profile. Compound meta-optic systems thus provide a flexible foundation for the development of the next generation of metasurface devices with superior performance and novel functionality.

A compound meta-optic can leverage the functionalies of meta-systems beyond single-layer metasurfaces. For instance, single-layer metalenses with a hyperbolic phase profile are typically made for the paraxial approximation, which means that the performance will suffer greatly under illumination with a large incident angle. These comatic aberrations will significantly reduce the field of view (FOV) during the imaging process. Compound metalens in this scenario can obtain a view-angle as wide as 30° due to the secondary metasurface providing a phase correction[64]. Such optimization has been used to create metalens appropriate for machine vision applications that require far-field imaging with a compact form factor.

Moreover, compound meta-optics offer additional engineering freedom to achieve multifunctional devices[32, 65] in addition to serving the performance optimization. Single-layer metasurface are only able to provide a limited set of functions or, if any, compromise the device efficiency due to the limited engineering freedom. Compound meta-optics, instead, which extend the DOF by using multiple independent metasurfaces, can perform functions beyond the single-layer counterparts. For instance, by carefully constructing the bilayer metasurface system, a metalens is capable of operating at several wavelengths without degrading performance. A single-layer metasurface, in contrast, might multiplex unit cells or rely on an inverse design technique, which would degrade the device performance and efficiency.

Furthermore, the processing of multi-channel information can also be performed via a

compound meta-optic system. Compared to single-layer metasurfaces, the structure with multiple meta-optics offers adequate space for light travel between metasurfaces and be redistributed serving the purpose of spatial multiplexing. As a result, compound meta-optics can perform more sophisticated and intricate functions than single-layer metasurfaces. For instance, a compound meta-optic including a multi-channel metalens and a multiplexed phase difference metasurface was proposed to achieve the quantitative phase mapping[66] in 2020. The phase mapping resolution of the compound meta-optic system can achieve $92.3 mrad \cdot um^{-1}$, and the optical system can be miniaturized into a chip-scale size.

Finally, compound meta-optics can provide distinctive and innovative functionalities beyond single-layer metasurfaces when co-optimizing multi-element systems. For instance, using a bilayer metasurface structure and coupling effects between metasurface layers for polarization filtering, a high circular dichroism of 0.7 can be achieved[62]. In this case, compound meta-optics offers a compact scenario for light mode filtering and selection.

1.6 Organization of the Thesis

In this dissertation, I will discuss my effort in developing compound meta-optic systems with novel features and applications. The additional engineering freedom arising from the multilayer metasurface architecture improves the system flexibility, resulting in multifunctional and/or extraordinary performance. In contrast to single-layer metasurface systems, compound meta-optics with more versatile functionalities provide a new avenue for high-quality wavefront control as shown in Fig.1.6 (a) and (b). In addition, object classifiers based on convolutional neural networks (CNNs) can be accelerated by applying compound meta-optics with multi-channel information processing , as illustrated in Fig.1.6 (c). Moreover, a large-scale compound meta-optics based on nanosphere lithography were demonstrated for image processing as shown in

Fig.1.6 (d). Finally, in addition to the distinctive functionalities of compound meta-optics, large-scale metasurface manufacturing is necessary for commercial applications. Hence, a scalable, cost-effective fabrication technique was proposed on the basis of a grayscale lithography platform as shown in Fig.1.6 (e). The detailed organization of this thesis can be described as follows.

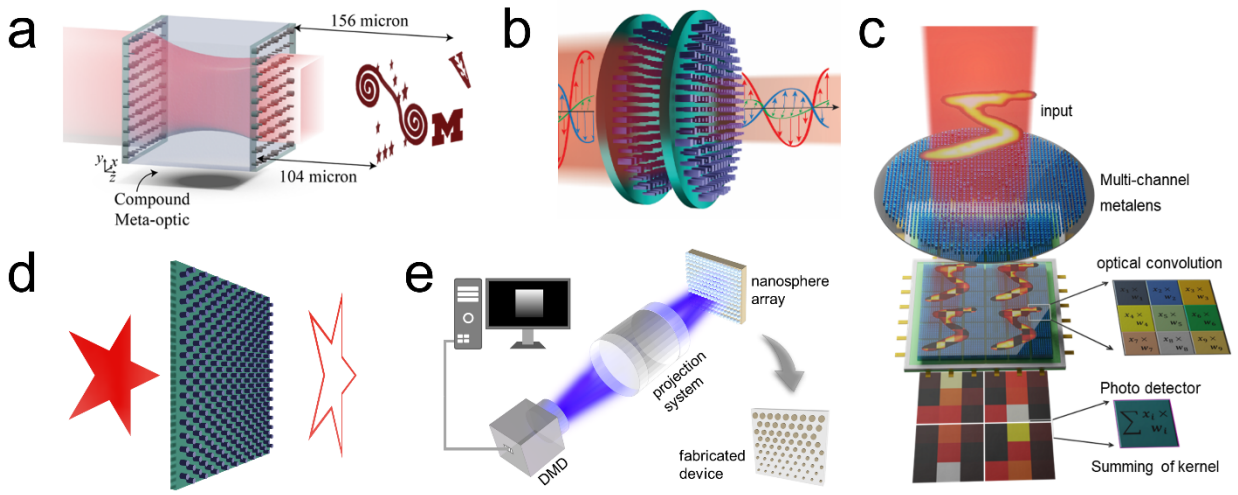

Figure 1.6 Various applications and novel fabrication methods for meta-optics. (a) Compound meta-optics for 3-dimensional displaying. (b) Compound meta-optics for lossless and complete field control. (c) Compound meta-optic as an accelerator for information processing. (d) Meta-optic as an angular filter for edge signal enhancement. (e) Nanosphere-assisted grayscale lithography for large-scale metasurface fabrication.

In **Chapter 2**, I present a compound meta-optic system that is used for high-efficiency and complete field manipulation. In comparison to a single-layer metasurface device, compound meta-optics utilize the light redistribution behavior between layers to achieve effective amplitude control. The additional engineering degree from the second-layer metasurface significantly prevents the amplitude manipulation loss that would otherwise occur in single-layer scenario. For proof of the concept, a high-efficiency beam former/splitter and a high-quality 3-dimensional hologram have been experimentality demonstrated. Moreover, a platform for end-to-end inverse design is being developed for additional polarization manipulation. In this case, mode division/multiplexers, mode converters, and vectorial holograms are experimentally presented to accomplish lossless and

complete field control.

In **Chapter 3**, I present compound meta-optics-based accelerators for object classification. The meta-optic system comprises two-layer metasurfaces, either creating multiple image channels or performing optical convolution. With incoherent light illumination, the meta-optic accelerator can be used to recognize and classify an object. Meanwhile, the meta-optic effectively off-loads the convolution operations from digital to the optical platform, resulting in a speedup of 50% when compared to the state-of-the-art fully digital system. Additionally, multifunctional categorization, including the intensity and polarization states, can be readily achieved due to the flexibility of compound meta-optics platform. Further developments and prospects for meta-optic accelerators are also explored.

In **Chapter 4**, I present a nanosphere lithography technique used for large-scale metasurface fabrication and applications. The large-scale metasurface was fabricated by nanosphere lithography within a hexagonal periodic lattice, which can be used for image edge enhancement with an all optical system. The optical edge detection mechanism is discussed and verified experimentally. Furthermore, a number of non-periodic large-scale metasurface devices, including metalens and meta-holograms, are fabricated and characterized in combination with a customized grayscale exposure system, exhibiting the flexibility and robustness of the proposed fabrication technique.

Finally, in **Chapter 5**, I draw a main conclusion of the thesis and the work during my Ph.D. research. In the end, I will provide my insights for the compound meta-optic platform.

Chapter 2

Compound Meta-optics for Field Control

2.1 Introduction

Control over the amplitude, phase, and polarization state of light is critical in a variety of scientific and industrial applications. Conventionally, this is achieved using a sequence of optical components such as lenses, polarizers, gratings, and amplitude masks. Such an approach results in physically large systems as well as reduced efficiency, especially when transmission loss is utilized to manipulate the wavefront. Optical metasurfaces, on the other hand, provide a path toward meeting the growing technical demand for compact and high-efficiency optical systems[67, 68, 69, 70]. Composed of two-dimensional arrays of subwavelength scatterers, metasurfaces can be designed to control the transmitted phase, amplitude, and polarization of light with remarkable capability.

Forming optical components such as combined beam-former and splitter devices requires independently manipulating the spatial amplitude and phase distributions of an electromagnetic wave. Though have been demonstrated through a variety of methods[34, 35], the typical metasurface beam splitters, without any beam shaping functionality, always suffer a low efficiency due to the diffraction loss. Another application of amplitude and phase control is in forming three-dimensional holograms, which can be produced with high quality if a specific complex-valued field profile is formed[59]. The complex-amplitude field necessitates the loss involved in the single-layer metasurface system, which is typically achieved by polarization conversion or absorption loss, resulting in low efficiency in specific applications[24, 59, 71, 72,].

Meanwhile, although manipulation over wavefront and polarization has been demonstrated in the past, independent control of phase and amplitude by a single layer metasurfaces was

achieved only at the expense of a polarization-dependent response[59] as illustrated in Fig.2.1 (a). The involvement of polarizer components introduces undemanding loss, based on the specific application[73], which can be as high as 90%. Spatial multiplexing can provide polarization-independent manipulation by using interference between the neighboring meta-atoms, as shown in Fig.2.1 (b). This method, however, leads to higher diffraction orders[74] due to the use of a larger supercell, limiting the diffraction efficiency in the target order.

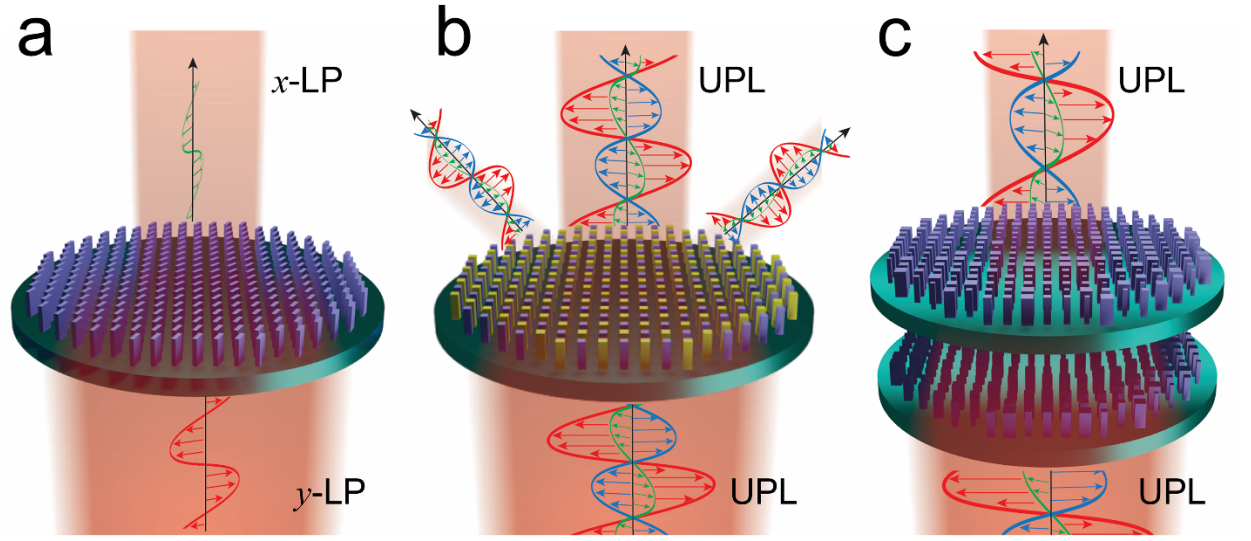

Figure 2.1 Complex-field control with metasurfaces. (a) A single metasurface, in the absence of a supercell, enables full and independent control (phase, amplitude, polarization) over one input polarization state. LP stands for linear polarized. (b) The use of supercells enables interference to be used for independent control over unpolarized light but results in loss to higher diffraction orders. UP stands for unpolarized. (c) Bi-layer meta-optics can be used for nearly loss-less full field control for unpolarized light.

The compound meta-optic systems, on the other hand, provide extra design freedom for free space light control[32, 75, 76, 77, 78]. This platform utilizes either the unique optical response in each layer or the light redistribution ability during propagation, avoiding unnecessary efficiency degradation as shown in Fig.2.1 (c). Moreover, the broken spatial symmetry along the optical axis in compound meta-optics enables unsymmetrical manipulation between the orthogonal polarization states, usually prohibited in single-layer meta-system. This method provides the

possibility of complete and lossless control of the light field in a compact scenario.

In this chapter, I will discuss the wavefront control mechanism of compound meta-optics and experimentally demonstrate a high-efficiency, independent amplitude and phase control strategy over an optical field using a compound meta-optic. This meta-system is comprised of a sequential metasurface separated by a distance and arranged along a common axis. The extra freedom of design offers the compound meta-optic system the capability to perform functions beyond individual metasurfaces. Besides, I will also discuss the theoretical model, where the Gerchberg-Saxton (GS) algorithm was used to design the compound meta-optic system. This model is achieved by a two-phase-only metasurface with a certain distance between, which enables high-efficiency amplitude control by redistributing the optical beam amplitude instead of using loss to form the desired amplitude distribution.

Moreover, I further expand this model to perform complex-amplitude manipulation for orthogonal polarization states by employing end-to-end design optimization. In this optimized platform, birefringent meta-atoms are used for both surfaces, enabling independent control over orthogonal polarization states as well as polarization conversion between those states. Redistribution of the wavefront between metasurface layers allows for nearly loss-less, complex-valued wavefront and polarization control, which is not limited by the symmetric Jones matrix (a more detailed discussion can be found in Appendix B.1).

As a proof of concept, I experimentally achieved high-efficiency beam-former-splitters and three-dimensional holograms for the complex-valued field control based on the phase-only compound meta-optic. Besides, to prove the complete manipulation ability of the further optimized compound meta-optic platform, I also demonstrated a spatial division multiplexer (SDM), an optical mode converter, and a vectorial hologram, which include independent control of amplitude,

phase, and polarization.

2.2 Design Strategy of Phase-only Compound Meta-optics

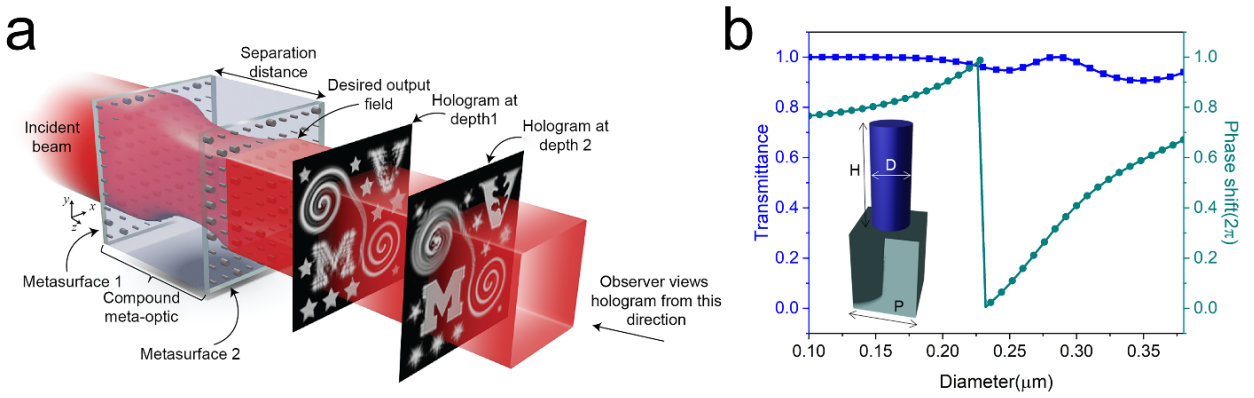

Figure 2.2 The optical compound meta-optic implementing independent phase and amplitude control over an incident optical field. (a) Illustration of a compound meta-optic converting a uniform illumination into a three-dimensional, complex-valued hologram. The depth of the three-dimensional hologram is visualized when the output field is imaged at different depths by an observer facing the device. (b) The transmission characteristics of the unit cell under normally incident plane wave illumination and periodic boundary conditions. The inset shows a schematic of the metasurface unit cell. Each cell has a period of P=570nm and contains an amorphous silicon nanopillar with a height of H=850nm. The nanopillar diameter is varied across the metasurface to implement the desired transmission phase profile. All the silicon nanopillars were embraced by PDMS as the support for the compound metasurface system.

The compound meta-optic is formed by two lossless phase-only metasurfaces separated by a physically short distance of homogeneous dielectric, as shown in Fig.2.2 (a). Together, they provide the desired independent amplitude and phase control. Adding additional metasurfaces would allow more control over the optical field, for instance, multi-wavelength performance or diffractive neural networks for multi-input multi-output applications, but only two metasurfaces are necessary for lossless complex-amplitude control at a single wavelength. As a proof of concept, meta-optics that combine beamforming and splitting and produce high-quality, three-dimensional holograms are experimentally demonstrated. The efficiency of the devices is high, only limited by the minor reflection from each metasurface, indicating the promise of optical compound meta-optics for high-efficiency holographic displays and optical components.

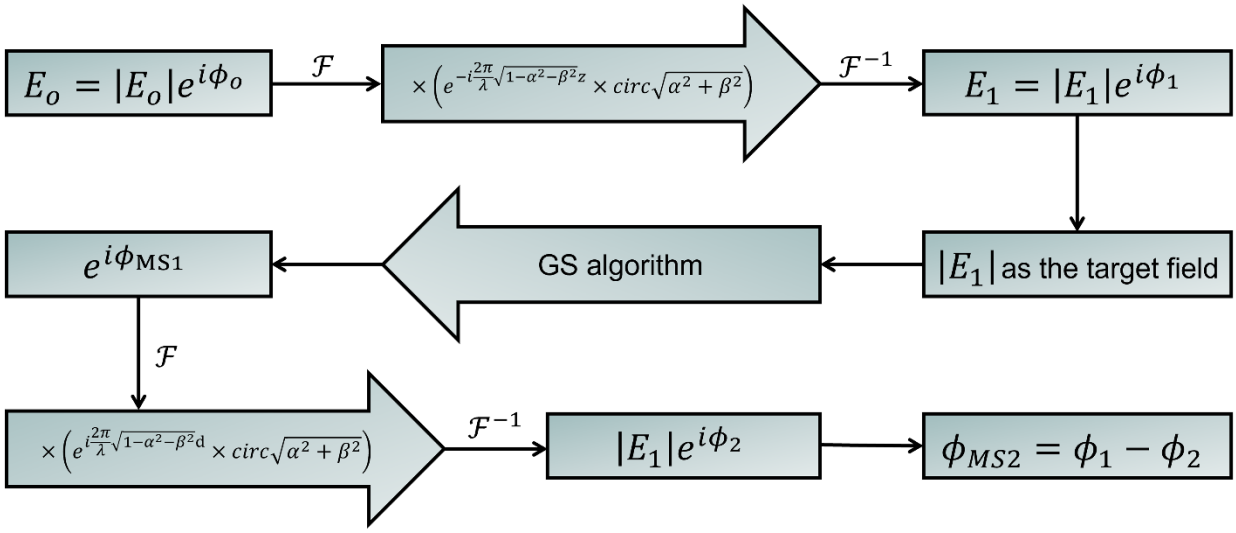

Figure 2.3 Gerchberg-Saxton algorithm-based design framework to generate a compound metasurface system for complex-amplitude control. E_0 represents the desired complex-amplitude distribution at the target image plane. E_1 is the field distribution at the second metasurface layer. ϕ_{MS1} and ϕ_{MS2} are the retrieved phase distribution for each metasurface layer to achieve independent amplitude and phase manipulation.

The proposed compound meta-optic devices consist of two phase-only metasurfaces, each impressing a phase discontinuity onto an incident wave. In order to provide enough phase manipulation at each metasurface layer, LPCVD deposited α-silicon based nanopillar on the fused silica substrate was employed as the basic meta-atoms. The refractive index of silicon (n=3.7) was characterized by ellipsometry (Details can be found in Appendix A.3). All the nanopillars were embraced in the Polydimethylsiloxane (PDMS) surrounding as the support for the compound meta-optic structure. Circular cross-sections of the nanopillars were chosen to ensure polarization invariance. However, elliptical or rectangular cross-sections could be used if polarization control is required. In Fig.2.2 (b), the transmission characteristics as well as the diagram of basic meta-atoms are illustrated. Variation of the pillar diameter (D) provides control over the transmission phase. The silicon pillar height ($H = 850nm$), unit cell period ($P = 570nm$), and illuminating wavelength ($\lambda_0 = 1.3\mu m$) have been chosen to provide high transmittance for a large transmission phase range. For these dimensions, a transmission phase coverage of 78% can be

achieved with a transmission magnitude greater than 0.93.

The compound meta-optic system was designed by the Gerchberg-Saxton (GS) algorithm as shown in Fig.2.3. The details of GS algorithm can be found in Appendix B.1. The first metasurface applies a phase discontinuity onto the known incident wave. This phase shift is designed so that the desired electric field amplitude distribution is formed at a distance equal to the separation distance between the metasurfaces. However, the phase of this field profile is incorrect relative to the desired output phase profile. Therefore, the second metasurface applies a phase correction to form the desired complex-valued electric field distribution. The light propagation behavior in the uniform medium can be derived by the angular spectrum method (details can be found in Appendix A.4), giving an accurate prediction of the complex-valued field along the propagation axis. Since the metasurfaces are assumed to be transparent, the amplitude distributions of the wave transmitted by metasurface 1 and incident on metasurface 2 are known from the incident and desired field profiles, respectively. The free parameters are the transmission phase distributions at each plane, which are optimized using the GS algorithm that links the incident and output field amplitude distributions.

The phase shift distribution of each metasurface is calculated as the difference between the phase distributions of the transmitted and incident fields.

$$\phi_{ms1} = \phi_{tr1} - \phi_{E_{inc}} \tag{2.1}$$

$$\phi_{ms2} = \phi_{E_{out}} - \phi_{inc2} \tag{2.2}$$

where $\phi_{E_{inc}}$ is the phase of the incident field, ϕ_{tr1} is the phase profile of the transmitted field from metasurface 1, ϕ_{inc2} is the phase of the field incident on metasurface 2, and $\phi_{E_{out}}$ is the phase profile of the desired output field. The metasurfaces are then designed to implement ϕ_{ms1} and ϕ_{ms2} as a transmission phase shift of the form $e^{i\phi_{MS}}$ on the incident wave. Here, a time convention

of $e^{-i\omega t}$ is assumed.

Once the light propagation behavior was determined among the compound meta-optic system, the phase distribution of metasurface 1 and 2 was retrieved by the algorithm exhibited in Fig.2.3. Compared to single layer system, the extra metasurface layer offers another freedom of design for independent amplitude and phase control, verified by the complex-amplitude target function in the algorithm. To fabricate the metasurface, the phase shift profiles producing the desired phase profile are sampled at the unit cell periodicity and converted to distributions of nanopillars with the corresponding diameters according to Fig.2.2 (b). Each metasurface was then fabricated individually and aligned to form the compound meta-optic devices.

2.3 Compound Meta-optics for Lossless and Complex-valued Field Control

Once the meta-optic system was designed, each metasurface layer was fabricated using nanofabrication techniques developed to construct multi-metasurface devices. To be specific, an 850nm-thick layer of amorphous silicon was deposited onto a fused silica substrate by the low-pressure chemical vapor deposition (LPCVD) method. Each metasurface pattern was defined using electron beam lithography (EBL), and then nanopillars were formed using reactive ion etching (RIE). The metasurfaces were subsequently enclosed in a protective layer of PDMS. Finally, the metasurfaces were spaced by a layer of PDMS and carefully aligned using translation stages to form the complete compound meta-optic (The alignment process is shown in Appendix B.2).

The compound meta-optics were then characterized using an unpolarized supercontinuum laser whose beam is passed through a monochromator to select the desired wavelength. The resulting beam overfilled the meta-optic footprint to form the desired uniform illumination. The meta-optic performs the required spatial amplitude and phase manipulation to form the desired complex-valued output field distribution. Intensity distributions at different depths from the meta-

optic output were then magnified with an objective and tube lens and recorded with a camera. Amplitude control over the incident optical field can be directly verified by imaging the output plane of the meta-optic. If the output field phase distribution is accurate, propagation of the output field will form the desired intensity profile at each plane in space beyond the meta-optic. However, if the phase distribution is inaccurate, the desired intensity will not be formed at the corresponding distance. Therefore, phase control was verified by comparing the measured intensity distribution at a plane beyond the meta-optic output.

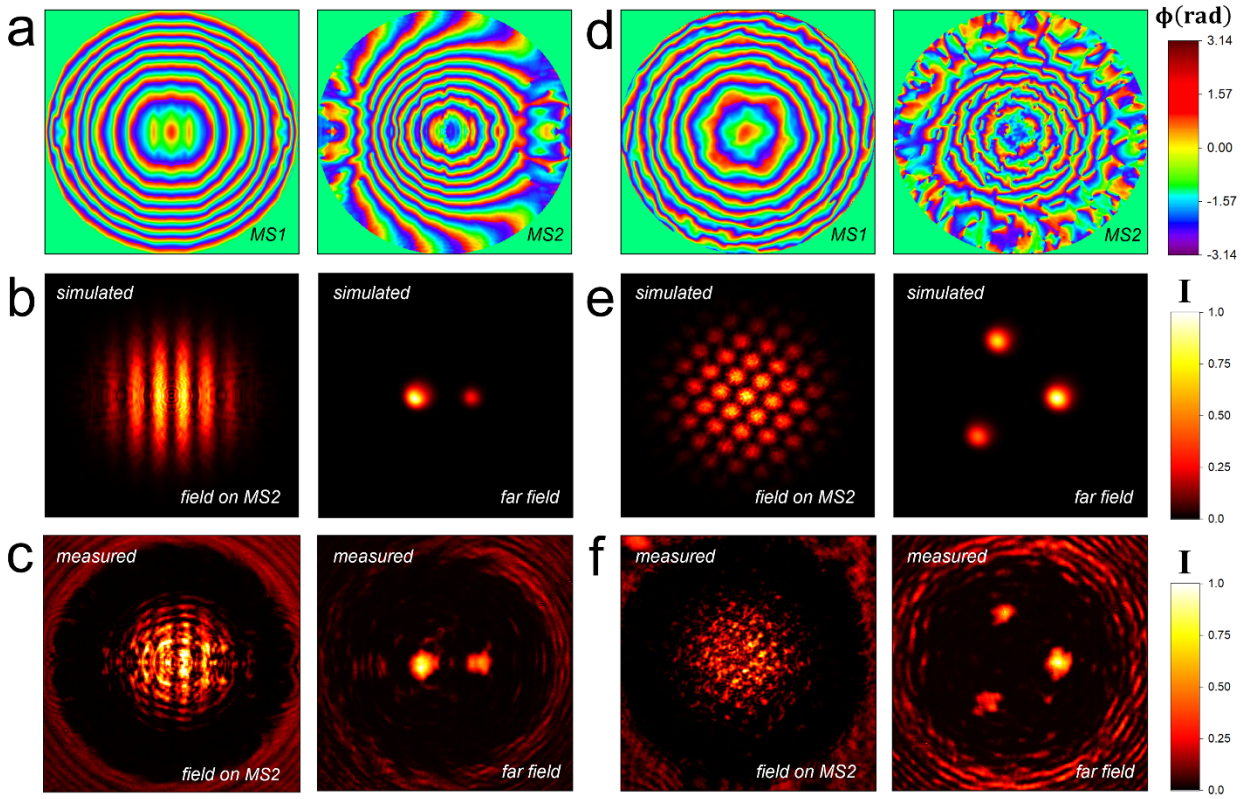

Figure 2.4 Measurement results of meta-optics implementing a beamforming and splitting function. Uniform circular illumination is manipulated to form multiple Gaussian beams at the output. (a) The phase profile of compound metasurfaces for two Gaussian beams former. (b) and (c) The simulation and measurement results of the output intensity from two Gaussian beams former at the second layer metasurface (left) and far-field (right). (d) The phase profile of compound metasurfaces for three Gaussian beams former. (e) and (f) The simulation and measurement results of the output intensity from three Gaussian beams former at the second layer metasurface (left) and far-field (right). The intensity redistribution and beam splitting indicate well complex-amplitude control.

To demonstrate the accuracy of the compound meta-optic in providing independent phase

and amplitude control with high efficiency, two different functions are presented. First, a combined beamforming and splitting function is demonstrated, where a uniform illumination is reshaped to form multiple output beams with specified amplitude profiles and propagation directions. Second, a meta-optic to reshape a uniform illumination to form a computer-generated, three-dimensional hologram is exhibited. The efficiency was calculated based on the images captured by the near-infrared (NIR) camera with the background noise correction processed by subtraction of a blank image. The reference intensity was calculated from images of the substrates without any meta-optics. With the same integration time, the intensity distribution can be revealed by the photon count from the camera. The efficiency of the beam-former-splitter devices was calculated as the intensity within an area encompassing each beam in the far-field, divided by the intensity incident on the device. For the three-dimensional hologram example, the efficiency is the intensity contained in the transmitted field divided by the intensity incident on the device.

Using the meta-optic design process, two meta-optic devices performing optical beamforming and splitting at a wavelength of $\lambda_0 = 1.3\mu m$ were designed and fabricated. In both examples, circular uniform illumination with a diameter of $200\mu m$ is reshaped to form multiple output Gaussian beams. Each metasurface is $200\mu m$ in diameter and separated by $325\mu m$ of PDMS. The first meta-optic forms the interference pattern between two Gaussian beams of different beamwidths, propagation directions, and relative intensities. The desired output field profile is calculated as the superposition of the two Gaussian beams as

$$E_{out} = -e^{-\left(\frac{r}{45.5\lambda_0}\right)^2} e^{ik_0 x \sin(-2^\circ)} + \sqrt{0.5} e^{-\left(\frac{r}{32.5\lambda_0}\right)^2} e^{ik_0 x \sin(2^\circ)} \tag{2.3}$$

which forms a fringed interference pattern. Here, r represents the radial distance from the center of each gaussian beam. Since the exact complex-valued field distribution is formed, only the desired Gaussian beams are produced, and undesired diffraction orders are not present. Fig.2.4 (a)

exhibits the retrieved phase profile of two metasurface layers, respective. The comparisons of the intensity profiles formed by the meta-optic at the output plane and far-field in simulation and measurement are presented in Fig.2.4 (b) and (c). In each case, the measurements closely agree with the simulated intensity distributions and form the desired Gaussian beams with little diffractive noise. Furthermore, the transformation in amplitude and phase was performed with an efficiency of 81% in simulation and 72% in measurement.

A second beam-former-splitter example was fabricated to produce three Gaussian beams. The propagation directions are chosen such that the output field has variations in both planar dimensions. The desired output field is calculated as the sum of three beams,

$$E_{out} = e^{-\left(\frac{r}{45\lambda_0}\right)^2}\{e^{ik_0[x\sin(2^\circ)+y\sin(0^\circ)]} + \sqrt{0.75}\, e^{ik_0[x\sin(-1^\circ)+y\sin(3^\circ)]} + \sqrt{0.5}\, e^{ik_0[x\sin(-2^\circ)+y\sin(-2^\circ)]}\} \quad (2.4)$$

Fig.2.4 (d) presents the phase distributions of both metasurfaces at different layers. The comparisons of the intensity profiles formed by the meta-optic at the output plane and far-field in simulation and measurements are also exhibited in Fig.2.4 (e) and (f). Here, the desired Gaussian beams are formed at the correct relative intensities, propagation directions, and beamwidths, verifying the accuracy of amplitude and phase control performed by the meta-optic. The device efficiency is 79% in simulation and 65% in measurement. The lower measured efficiency compared to the simulated results is due to the fabrication imperfection as well as the slight alignment error. The former factor will introduce the phase mismatch between the fabricated and designed device, leading to undesired field distribution. Although the latter factor is unavoidable due to the limitation of mechanical parts in the alignment system, the alignment tolerance may be further improvement by extra optimization algorithms.

Image Component	Rotation Axis	Rotation Angle (degrees)	Center Position
Spiral	$y = x$	20	$(0, 0, 104)\mu m$
Stars	No rotation	No rotation	$(0, 0, 104)\mu m$
University of Michigan logo	y	25	$(-35, -35, 156)\mu m$
Vanderbilt University logo	x	25	$(55, 50, 104)\mu m$

Table 2.1 Manipulation parameters of each image component to assemble the 3-dimensional hologram

The measured intensity images from each of the meta-optic devices demonstrate the accuracy of complex-valued optical field control with high efficiency. Specifically, the intensity measured at the output plane of the meta-optic demonstrates amplitude control since the uniform illumination is reshaped. The intensity measured at a plane beyond the aperture (after the optical field propagates away from the meta-optic output) demonstrates phase control since the desired intensity will only be formed if the output phase profile is accurate. An inaccurate phase profile would alter the propagation characteristics of the optical field so that the measured intensity pattern would not match the desired result. This is verified in Fig.2.4, where combined beam-former and splitters are demonstrated to form intensity distributions that closely match the expected distributions. Even though a small number of Gaussian beams were formed with these devices, meta-optics can be designed to produce a larger number of beams with different amplitude profiles. The measured efficiency of the beam-former-splitter designs of 78% and 65% is higher than that of methods that would require loss.

Another attractive application of high-efficiency amplitude and phase control is three-dimensional holography. While phase-only metasurfaces can produce holograms, phase and amplitude control allows for enhanced image quality, especially for three-dimensional holograms. Such complex-valued holograms have been generated using lossy methods, most commonly

reflection or polarization loss. Here, the meta-optic design approach was utilized to demonstrate high-efficiency, three-dimensional holograms. Multiple computer-generated hologram approaches can be used to display a three-dimensional scene, but one method is demonstrated here: a hologram composed of solid flat image components more applicable to generating a realistic hologram scene. This technique can be used to produce a faceted representation of an object, leading to the ability to form 3D holograms of life-like scenes.

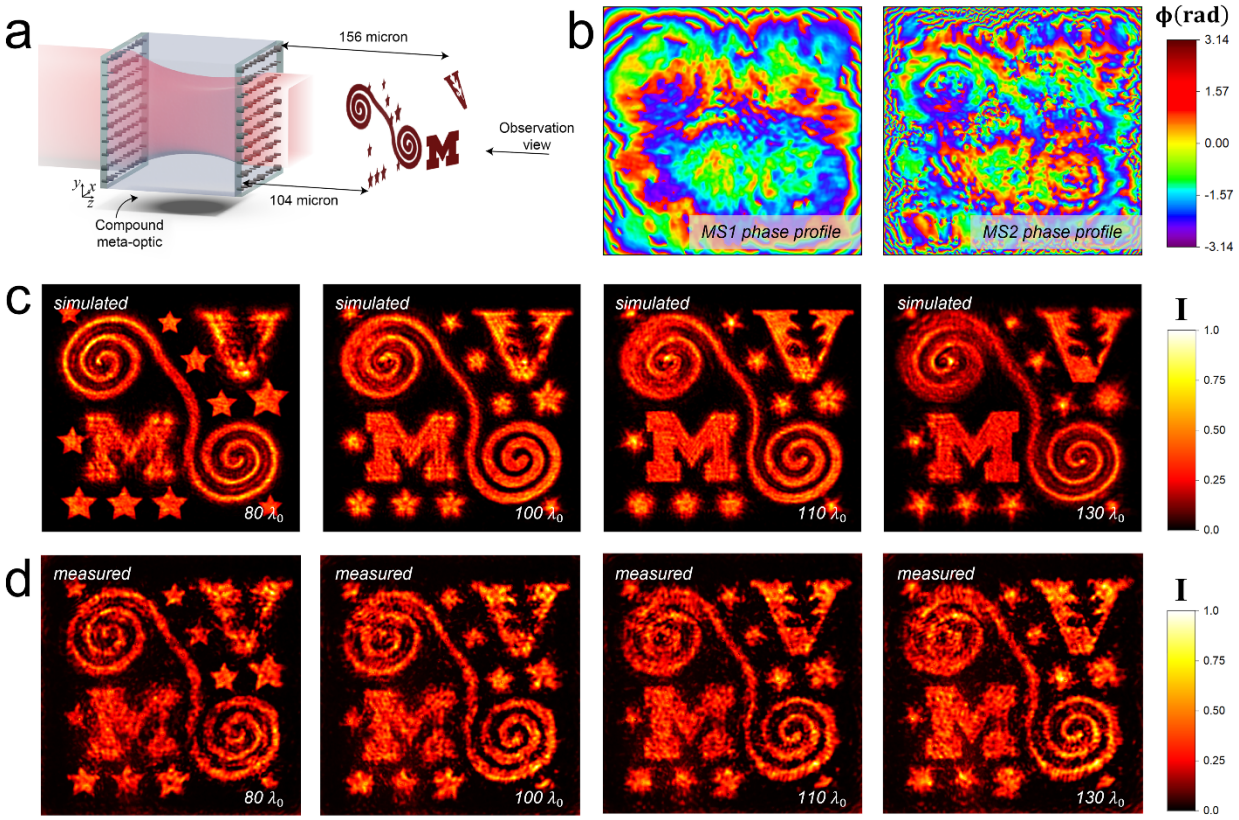

Figure 2.5 Measurement results of meta-optics implementing a 3-dimensional hologram. A uniform plane-wave-like illumination was used. The intensity has been normalized to respective maximums. (a) The diagram of the compound meta-optic structure architecture forms the 3d holograms at variant depths. (b) The phase profile of the first(left) and second(right) layer metasurface. (c) The simulated output field intensity profile from the compound meta-optic. The output field was calculated at a variant distance from the second layer metasurface. The bottom-right corner label indicates the distance. (d) The measured output field intensity profile from the compound meta-optic. As a comparison, the distance between the second metasurface and the simulated field was chosen to match the measurement results.

For this example, a compound meta-optic was designed where each metasurface is a 200μm

square array of nanopillars separated by 325μm of PDMS. The operating wavelength is λ_0=1.3μm. The output field of the compound meta-optic was engineered in amplitude and phase to form the scene shown in Fig.2.5 (a). The large spiral, University of Michigan (M), and Vanderbilt University (V) logos are all tilted in space but in different directions. As a result, different cross-sections of the image come into focus when imaging at different depths from the meta-optic output plane. The detailed geometrical parameters of the 3D hologram are exhibited in table 2.1.

The phase profile of each metasurface is exhibited in Fig.2.5 (b), respectively. Fig.2.5 (d) shows intensity images measured at different depths in the 3D hologram, which closely match the simulated images in Fig.2.5 (c). Specifically, the first image shows the middle of the spiral and stars in focus, while the remaining images show different cross-sections of the logos. The full three-dimensional nature of the hologram can be seen by scanning the focal plane through the depth of the hologram. The compound meta-optic performs the desired complex-valued field manipulation with a simulated efficiency of 82% and measured efficiency of 75%, significantly exceeding the efficiency of loss-based approaches.

Similarly, the measured three-dimensional holograms shown in Fig.2.5 very closely match the desired intensity images, demonstrating that the meta-optics can produce life-like holograms. The images produced in Fig.2.5 (d) with phase and amplitude control avoid the image speckle common to phase-only implementations produced with phase-retrieval algorithms. While the fabricated meta-optics demonstrated relatively simple holograms, meta-optics can be designed to form 3D holograms of life-like scenes. This approach also maintains the image contrast compared to the desired phase profile simply applied to the uniform illumination. Here, we can compare the complex-valued control provided by the meta-optic and the phase-only control from a single metasurface. Phase-only control is achieved by an individual metasurface applying a desired phase

profile to the incident uniform illumination. The resulting transmitted field exhibits the desired phase profile but an incorrect amplitude profile as shown in Fig.2.6.

In the case of the solid-image three-dimensional hologram, the phase-only metasurface was designed to implement the phase distribution of the desired output field profile. As the transmitted field distribution propagates away from the metasurface, it forms a version of the desired hologram image. Fig.2.6 (b) shows the hologram intensity at different depths for the cases of the simulated phase-only control system. Compared to the phase-only results, the compound meta-optic system exhibits higher hologram quality since both the phase and amplitude profiles of the field distribution are manipulated to match the desired distribution.

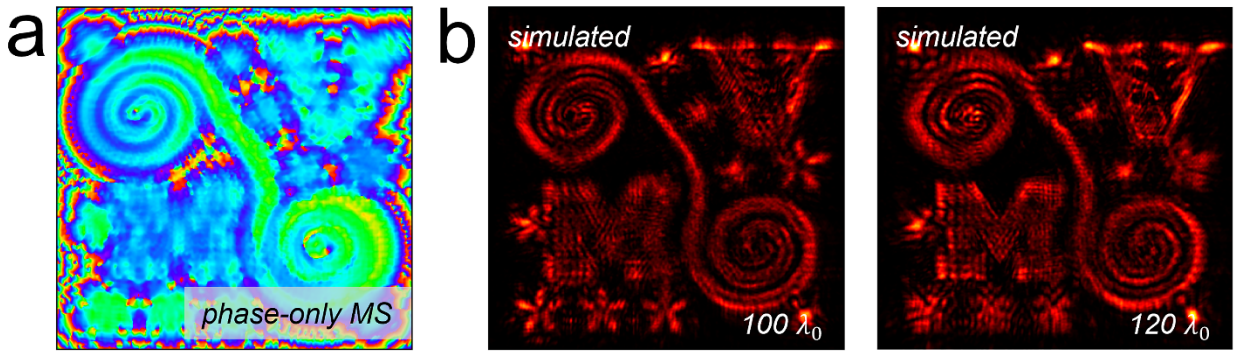

Figure 2.6 Single-layer phase-only metasurface to produce the 3d hologram. (a) The phase profile of single layer metasurface for hologram generation. (b) The simulated output field intensity from the metasurface. The field was calculated at a variant distance to show a 3d hologram profile. The bottom-right corner label indicates the distance between the hologram and metasurface.

High-efficiency amplitude and phase control over optical fields enable compound meta-optics to explicitly perform a variety of applications without inherent losses in efficiency. In contrast, loss-based amplitude control significantly reduces the device's efficiency. For example[73], a measured efficiency of 6.4% was demonstrated in forming a complex-valued hologram using polarization conversion at THz frequencies (however, intrinsic unit cell losses also contributed since the measured efficiency for a similar phase-only version was 19.1%). Even when unit cells

are optimized to obtain a maximum polarization conversion efficiency of 100%, the overall efficiency of a device is less than unity and highly case-dependent due to variation of transmission amplitude over the metasurface. Therefore, there are two main advantages of the compound meta-optic approach in terms of efficiency. First, using polarization loss for amplitude control requires a specific input polarization, which decreases the overall efficiency if an unpolarized source is used. Instead, the proposed method is polarization independent and avoids this issue. Second, the efficiency of loss-based approaches is highly case-dependent, but our work can achieve near-unity efficiency (in the ideal case) regardless of the required amplitude control. As a result, the measured 75% efficiency of the compound meta-optic producing the 3D hologram is significantly higher than lossy methods and is approximately independent of the desired amplitude control.

2.4 Physics Driven End-to-end Optimization for Compound Meta-optics

In this section, I will discuss the lossless and complete light control ability of compound meta-optic over amplitude, phase, and polarization based on the end-to-end optimization method. In this platform, birefringent meta-atoms are used for both surfaces, enabling independent control over orthogonal polarization states as well as polarization conversion between those states. Redistribution of the wavefront between metasurface layers allows for nearly loss-less, complex-valued wavefront and polarization control, which is not limited by the symmetric Jones matrix (a more detailed discussion can be found in Appendix B.3). As a proof of concept, I experimentally demonstrated a meta-optic for optical mode manipulation[79, 80, 81, 82], including a spatial division multiplexer (SDM), an optical mode converter, and a vectorial hologram. All the devices achieve experimental diffraction efficiencies above 80%, showing excellent agreement with the theoretical prediction.

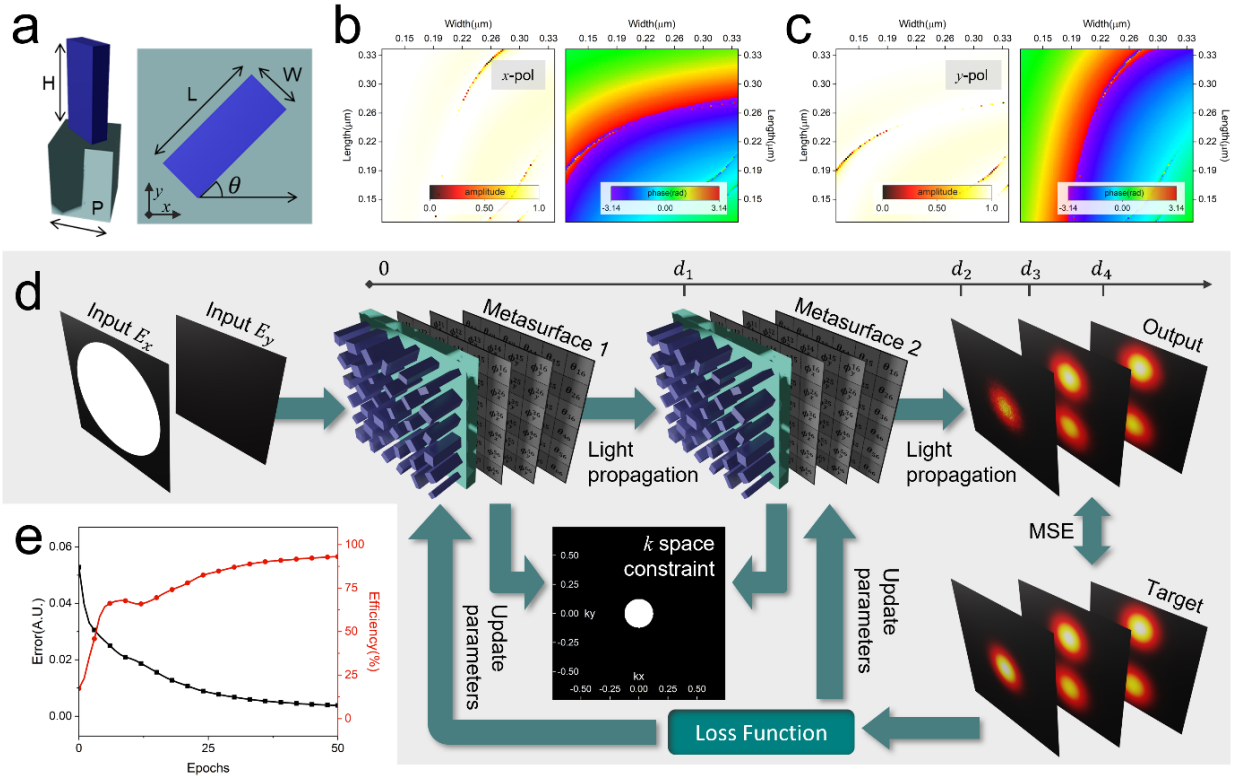

Figure 2.7 Inverse design of multi-layer meta-optics. (a) Schematic of the birefringent meta-atom. (b) and (c) Transmission coefficient (amplitude and phase) map of the meta-atom under x and y polarized illumination, respectively, as a function of the geometry (width and length). In these maps, the rotation angle of the meta-atom was fixed at 0°. (d) The inverse design architecture allows for optimization of the amplitude, phase, and polarization state. Multiple optimization targets with various propagation distances, indicated by the coordinate (d2, d3, d4), were sampled for robustness. (e) The error function and efficiency of the meta-optic as a function of epoch.

The experimentally demonstrated meta-optic consists of two metasurfaces with near-unity transmission, each serving to control the phase delay and polarization conversion between the *x* and *y*-directions. In the design process, we utilized meta-atoms comprising α-silicon nanopillars with a height of 0.75μm and a period of 0.52μm, sitting on a silica substrate, as shown in Fig.2.7 (a). The design wavelength was 1.15μm and the polarization-dependent transmission coefficient map was calculated using rigorous coupled wave analysis (RCWA). The width and length of the nanopillars varied between 0.12μm and 0.34μm and the transmission and phase maps are presented in Fig.2.7 (b) and (c), demonstrating near-unity transmission and independent control over phase along the *x* and *y*-axes. This data forms the data library that is used in the design process of the

compound meta-optics.

In order to achieve full control over phase, amplitude, and polarization state of light, the incident field is divided into two separate channels, E_x and E_y, with each comprising a complex-amplitude field matrix. Based on the data library, each metasurface can independently control the phase along the *x* and *y* direction, as well as the polarization conversion, which is determined by the rotation angle, θ, of the meta-atom. The transmitted field of each rectangular nanopillar comprising the metasurface follows an analytical model based on the Jones matrix given by,

$$\begin{bmatrix} E_{x,out} \\ E_{y,out} \end{bmatrix} = \begin{bmatrix} \cos(\theta) & \sin(\theta) \\ -\sin(\theta) & \cos(\theta) \end{bmatrix} \begin{bmatrix} e^{i\phi_x} & 0 \\ 0 & e^{i\phi_y} \end{bmatrix} \begin{bmatrix} \cos(\theta) & -\sin(\theta) \\ \sin(\theta) & \cos(\theta) \end{bmatrix} \begin{bmatrix} E_{x,in} \\ E_{y,in} \end{bmatrix}$$

$$= \mathcal{M}\left(\phi_x, \phi_y, \theta\right) \begin{bmatrix} E_{x,in} \\ E_{y,in} \end{bmatrix} \tag{2.5}$$

where $E_{x,in}$, $E_{y,in}$ and $E_{x,out}$, $E_{y,out}$ are the *x* and *y* polarized incident and transmitted amplitude, respectively. ϕ_x and ϕ_y are the phase shifts provided by the resonator for *x* and *y* polarization, values that are dictated by the size of the resonator. θ is the pillar rotation angle, which determines the polarization conversion efficiency and transmitted phase for a given meta-atom in the metasurface. $\mathcal{M}$ represents the operator of Jones matrix.

To design the multilayer meta-optic, I employed an end-to-end inverse-design algorithm, as shown in Fig.2.7 (d), which is based on a physical model of light propagation within the meta-system. In previous work[83], we designed loss-less meta-optic phase profiles based on the Gerchberg-Saxton (GS) algorithm, which did not allow for the design of polarization states and required *prior* knowledge of the desired intensity distribution at the second metasurface layer. In this work, I utilize a stochastic gradient descent (SGD) solver[84], a common approach in machine learning applications, to specify the output intensity, phase, and polarization at a position in space after the last metasurface in the optic. In the forward analytical model, light propagating in free

space is described by the angular spectrum propagation operator,

$$\mathcal{R}(d) = \mathcal{F}^{-1}\mathcal{H}(d)\mathcal{F} \tag{2.6}$$

where $\mathcal{F}$ is a Fourier transform operator, d is the propagating distance, and $\mathcal{H}(d) = \exp\left[i \cdot (2\pi d/\lambda) \cdot \sqrt{1 - k_x^2 - k_y^2}\right]$ is the transfer function of light in k-space. Here, λ is the effective wavelength in the medium and k_x and k_y represent the lateral wavenumbers. Light propagating through the meta-optic is calculated by cascading the various elements and free-space regions and is given by,

$$E(x, y, p_{out}) = \mathcal{R}(d_2)\mathcal{M}\left(\phi_{x2}, \phi_{y2}, \theta_2\right)\mathcal{R}(d_1)\mathcal{M}\left(\phi_{x1}, \phi_{y1}, \theta_1\right)E(x, y, p_{in}) \tag{2.7}$$

where p is the polarization state. Eq.2.7 provides the optical response of a bilayer meta-optic and analytically connects the input electric fields $E_{x,in}$ and $E_{y,in}$ with the output fields, $E_{x,out}$ and $E_{y,out}$. This approach can be readily extended for many-layer systems, such as diffractive neural networks[85], going beyond the more traditional GS algorithm-based optimization.

To avoid overfitting in the training process, multiple output fields at various propagation distances were optimized simultaneously. Due to the complex-valued electric fields, the error function, defined by the mean square error (MSE), was calculated using both the real and imaginary components of the output field as well as the polarization states at each propagation distance. The target field profiles used to design the compound meta-optics in this manuscript are presented in the Appendix. The error gradient of the designable parameters was then calculated by the SGD solver, which was used to update all parameters simultaneously. The evolution of the error function, as well as the absolute efficiency, defined by the energy in the target mode over the input power, is presented in Fig.2.7 (e). Near-unity efficiency is achieved in roughly 50 training cycles (epochs). In addition, an angular filter was employed at the output field from each

metasurface as a constraint during optimization iterations as shown in Fig.2.7 (d). There are two main purposes for this restriction. First, a k-space filter will remove light propagating at high angles between the metasurfaces, mitigating the dependence of the optical response on the angle of incidence. Second, the angular spectrum filter will reduce the required phase gradient of each metasurface resulting in more gradual meta-atom changes and reduced scattering. Ultimately, the k-space filter results in higher efficiency meta-optics, and a comparison of the optimized phase profile with/without the angular spectrum filter is presented in Appendix B.4.

2.5 Compound Meta-optics for Lossless and Complete Field Control

To experimentally validate the design methodology, each optimized metasurface was realized by starting with a wafer comprising a 0.75μm thick silicon device layer on quartz. The silicon device layer was patterned into nanopillars with a period of 0.52μm using electron beam lithography (EBL) followed by reactive ion etching (RIE). A polymethyl methacrylate (PMMA) layer was spin-coated over each metasurface as a protective coating as well as serving as an index-matching layer. The two metasurfaces were aligned using a custom alignment and bonding system (see details in Appendix B.2) with PDMS being used as the bonding material. Alignment of the metasurfaces was aided by fabricating an alignment mark consisting of a metasurface hologram, designed to project an alignment symbol at the prescribed separation distance. The final alignment was accomplished by observing the output intensity distribution of the meta-optic while tunning the lateral position of the metasurfaces. As a proof of concept, I optimized a series of bilayer meta-optics with an aperture size of 200μm. The separation distance between layers was set at 287.5μm, which was chosen to balance the spatial resolution of the designed amplitude function and the sensitivity to the angle of incidence[77].

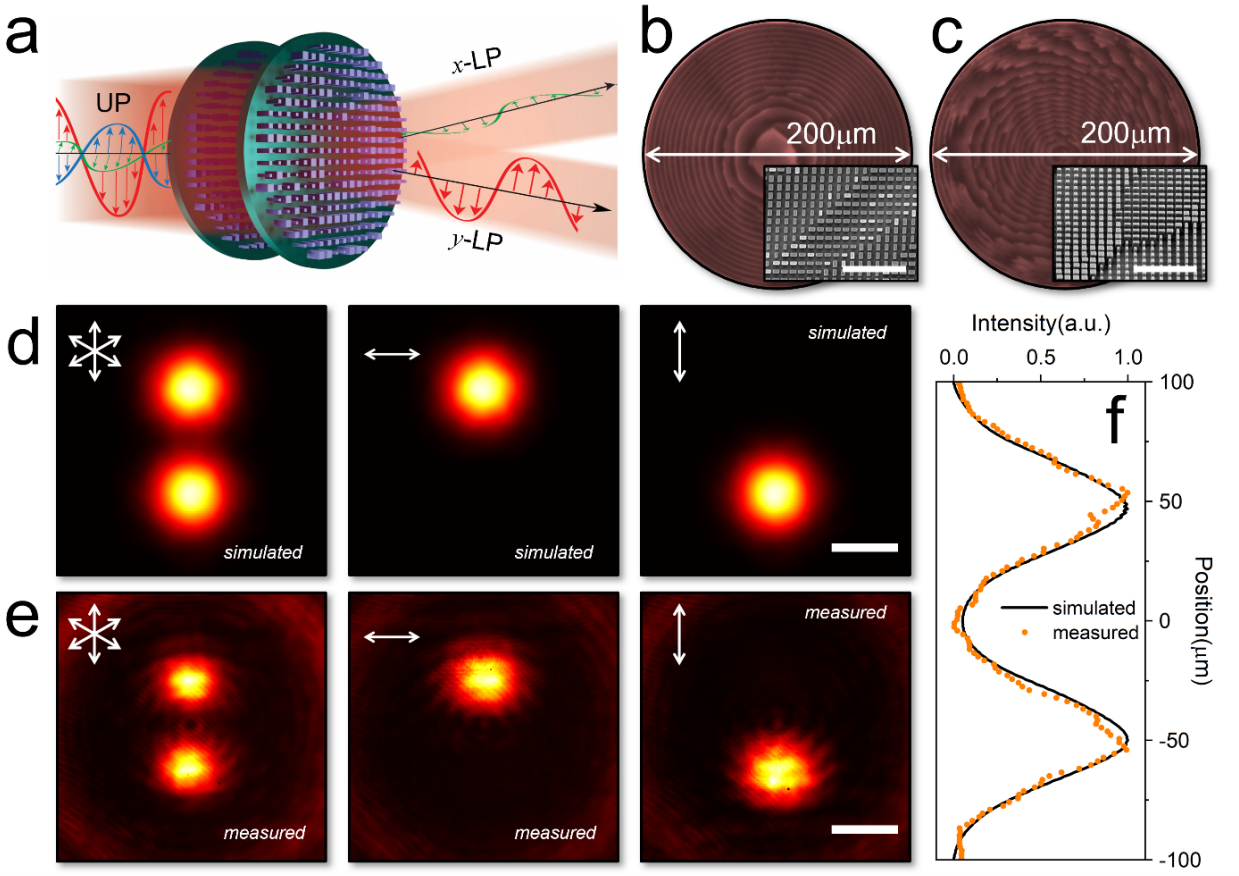

Figure 2.8 Meta-optic-based SDM to unpolarized light. (a) Schematic of the multi-layer meta-optic for SDM to unpolarized beams. (b) and (c) Optical images of each metasurface in the meta-optic. The insets are SEM images of metasurfaces. Scale bar: 4μm. (d) and (e) Simulated and measured polarization-dependent intensity distributions after the meta-optic. An unpolarized supercontinuum laser was used as the source. The arrows in the upper-left corner indicate the analyzer direction, which is unpolarized (left), *x*-polarized (middle), and *y*-polarized (right). Scale bar: 50μm. (f) Simulated and measured mode profile after the meta-optic as a function of lateral position. The intensity has been normalized to the maximum value.

A meta-optic that operates as both a mode sorter and mode shaper for free-space spatial division multiplexing (SDM)[79] is first designed and fabricated as shown in Fig.2.8 (a). The meta-optic splits incident light into *x* and *y*-polarization states while, at the same time, transforming the two wavefronts into Gaussian profiles. Specifically, the desired output field at the second metasurface is given by a superposition of two Gaussian beams with the same beam waist,

$$\begin{bmatrix} E_x \\ E_y \end{bmatrix} = \begin{bmatrix} e^{-\left(\frac{r}{28.3\lambda_0}\right)^2} e^{ik_0 y \cdot \sin(0.03°)} \\ e^{-\left(\frac{r}{28.3\lambda_0}\right)^2} e^{ik_0 y \cdot \sin(-0.03°)} \end{bmatrix} \tag{2.8}$$

where λ_0 is designed working wavelength, k_0 is the free-space wavenumber, and r is the radial distance from the center of the aperture. In this case, since the proposed function is polarization independent, the rotation angle, θ, was fixed at 0° for all metasurface pixels. The optimized phase profile for each polarization channel can be found in Appendix B.5. Both metasurface layers exhibit a smooth profile and the optical and scanning electron microscope (SEM) images are shown in Fig.2.8 (b) and (c), respectively. The meta-optic was characterized by imaging the far-field beam profiles for both polarizations with the results presented in Fig.2.8 (d) and (e). The measured beams exhibit a Gaussian profile, with each beam being composed of the desired polarization component. The quantitative comparison of the beam intensity distribution between the simulated and measured results are presented in Fig.2.8 (f), showing excellent agreement. Furthermore, the diffraction efficiency, defined by the intensity in the two Gaussian beams over the input energy, with Fresnel reflection correction, was measured to be 88.64%. As a comparison, a single-layer metasurface with the same function has a maximum theoretical efficiency of only 5.3% (see other instances in Appendix B.3).

To explore the alignment sensitivity for compound meta-optic, the lateral alignment sensitivity of the spatial mode division/multiplexing (SDM) device is calculated as shown in Fig.2.9 using the angular spectrum propagation method. In the simulation, I added a misalignment factor along the lateral direction, which led to aberration in the output field. The ideal and aberrated output intensity are shown in Fig.2.9 (b), (c), and (d), respectively. Aberrations can be observed when the lateral misalignment is over 1μm. The vertical alignment will have a higher tolerance as shown in Fig.2.10, where a Gaussian-like shape can still be maintained even with 3μm vertical misalignment. By comparison between the simulated and measured results, the in-situ alignment system can provide a sub-1μm alignment resolution.

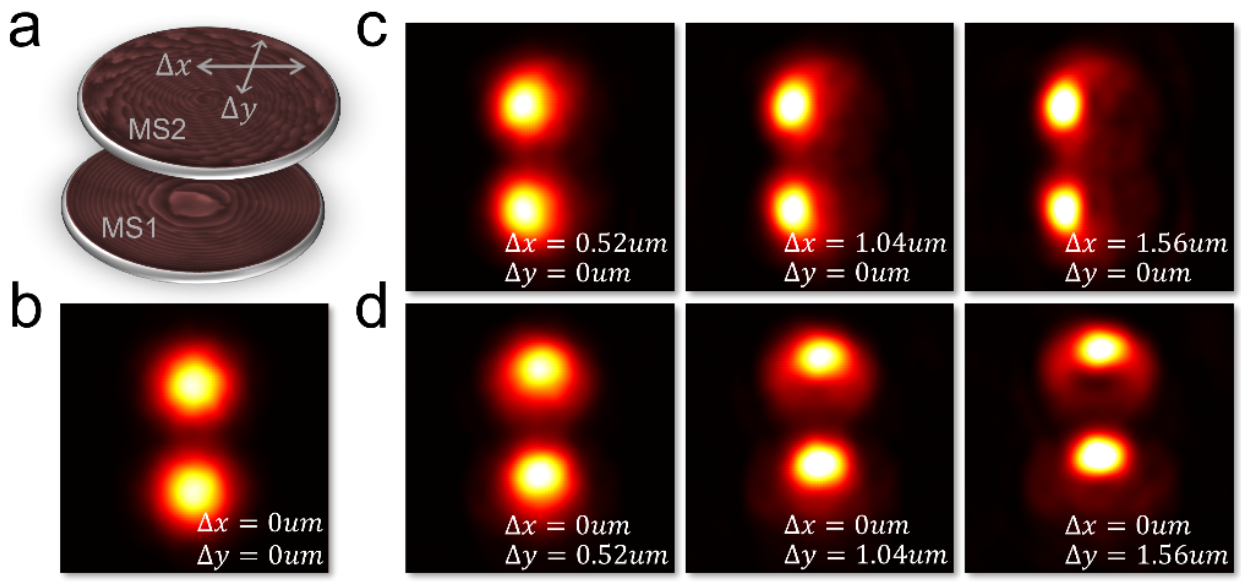

Figure 2.9 Simulated sensitivity to lateral misalignment. (a) Diagram of lateral misalignment. (b) The simulated output field without any misalignment. (c) and (d) The simulated output field with various misalignment values along the *x* and *y*-axis.

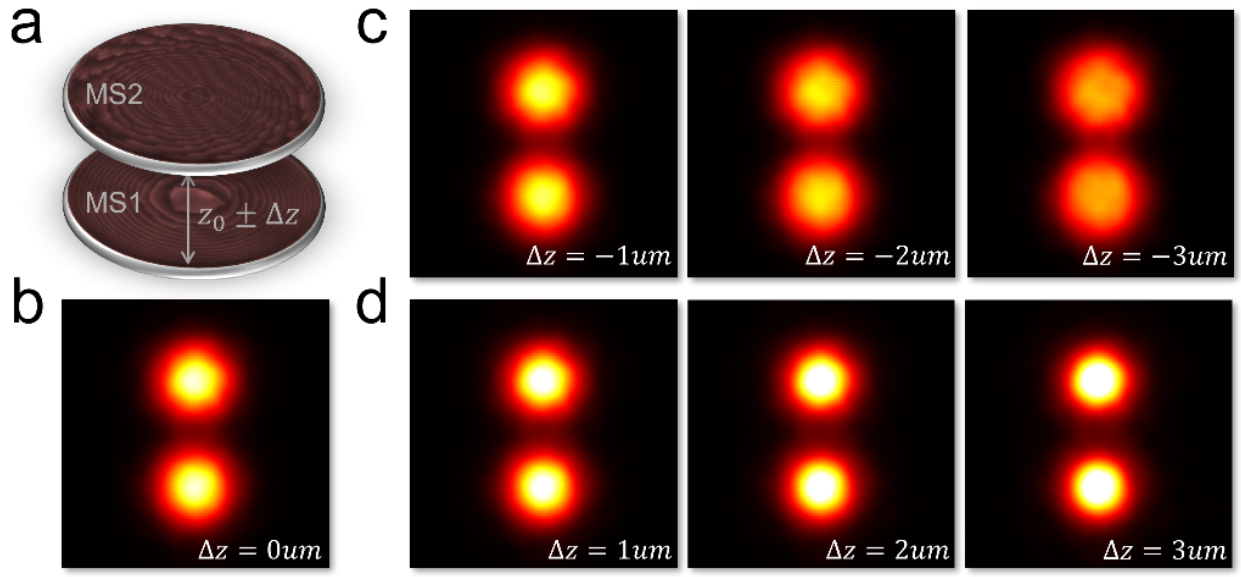

Figure 2.10 Simulated sensitivity to vertical misalignment. (a) Diagram of vertical misalignment. (b) The simulated output field without any misalignment. (c) and (d) The simulated output field with various misalignments values along z-axis.

The design freedom associated with this approach can also be used to realize a meta-optic that acts as an arbitrary mode converter, allowing for the transfer of any polarization state across the Poincare sphere. As an example, I used the meta-optic to convert a single polarization state

into two, while maintaining high conversion efficiency.

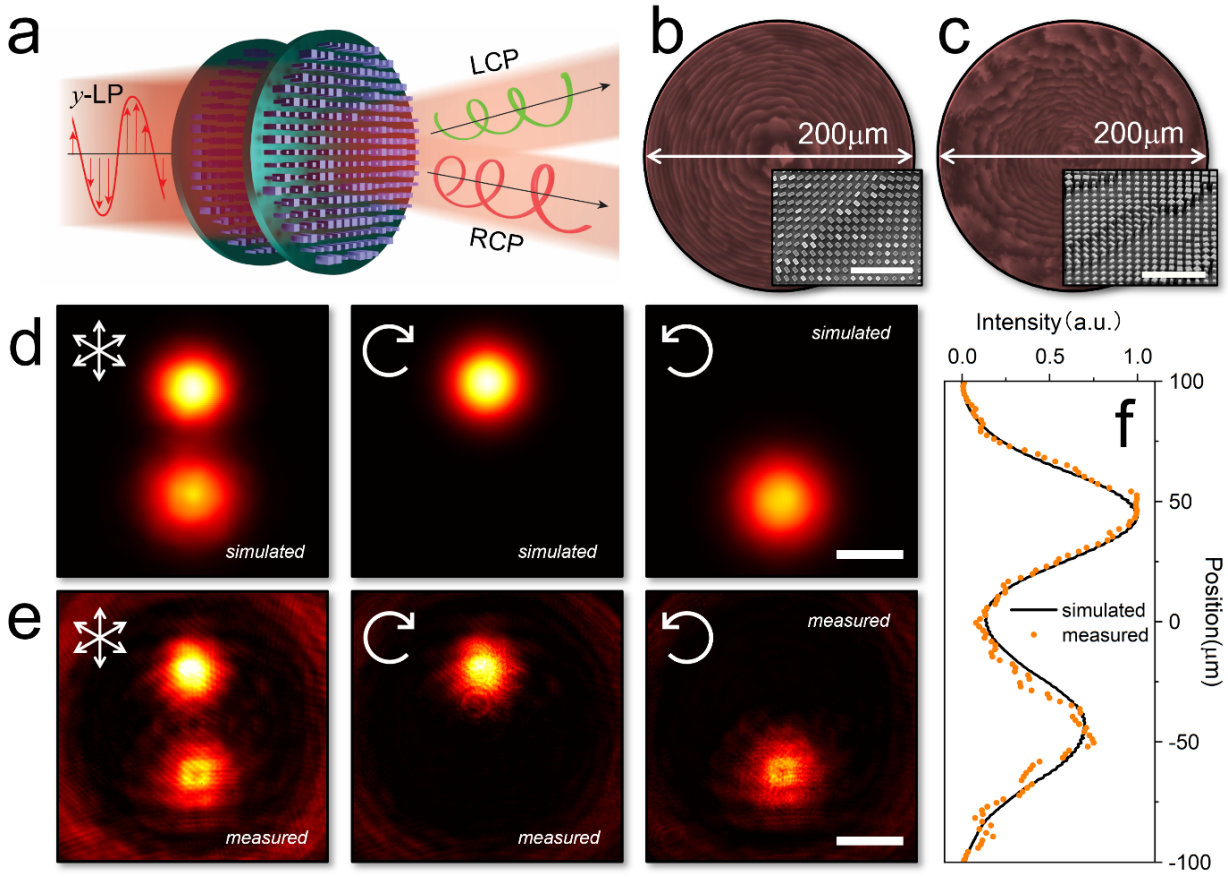

Figure 2.11 Meta-optic-based mode conversion for circularly polarized light. (a) Schematic of the multi-layer meta-optic for mode conversion to linearly polarized beams. (b) and (c) Optical images of each metasurface in the meta-optic. The insets are SEM images of metasurfaces. Scale bar: 4μm. (d) and (e) Simulated and measured polarization-dependent intensity distributions after the meta-optic. An unpolarized supercontinuum laser was used as the source. The upper-left corner arrows indicate the analyzer orientation, which is unpolarized (left), LCP (middle), and RCP (right). Scale bar: 50μm. (f) Simulated and measured mode profile after the meta-optic as a function of lateral position. The intensity has been normalized to the maximum value.

Specifically, the desired output field at the second metasurface layer can be calculated as the sum of multiple Gaussian beams as follows:

$$\begin{bmatrix} E_x \\ E_y \end{bmatrix} = \begin{bmatrix} e^{-\left(\frac{r}{28.3\lambda_0}\right)^2} e^{ik_0 y \cdot \sin(0.03°)} e^{\frac{i\pi}{2}} + e^{-\left(\frac{r}{35\lambda_0}\right)^2} e^{ik_0 y \cdot \sin(-0.03°)} \\ e^{-\left(\frac{r}{28.3\lambda_0}\right)^2} e^{ik_0 y \cdot \sin(0.03°)} + e^{-\left(\frac{r}{35\lambda_0}\right)^2} e^{ik_0 y \cdot \sin(-0.03°)} e^{\frac{i\pi}{2}} \end{bmatrix} \tag{2.9}$$

Eq.2.9 divides the overall intensity into two Gaussian beams, with one being lefthand-circular-

polarized (LCP) and the other righthand-circular-polarized (RCP), as shown in Fig.2.11 (a). The resulting phase profile can be found in the Appendix while the optical and SEM images are provided in Fig.2.11 (b) and (c), respectively. It is important to note that even though we demonstrate conversion from a single state to two orthogonal states, multiple and arbitrary output states are also achievable using the end-to-end inverse-design process (see details in Appendix B.6), providing a powerful tool for enhancing the capacity of free-space optical communication systems.

The simulation and characterization of the far-field intensity distribution of the mode converter are shown in Fig.2.11 (d) and (e), with both output beams having a Gaussian-like shape. The polarization states, characterized by a quarter waveplate combined with a linear polarizer, demonstrate an excellent match with the theoretical predictions, with the exception of ripples observed at the edges due to diffraction from the neighboring aperture. The agreement between the simulated and measured results can also be found in the quantitative analysis of the intensity distribution shown in Fig.2.11 (f). The meta-optic has a measured diffraction efficiency, with Fresnel reflection correction, of 82.44%. The slight decrease in efficiency compared to the SDM meta-optic may be due to the inclusion of a varying rotation angle for each metasurface pixel, leading to additional fabrication errors.

The extra design degrees of freedom associated with multilayer meta-optics ultimately enable loss-less polarized complex-field control, which is not possible using a single-layer metasurface. To illustrate the full power of this approach, I demonstrate a meta-optic vectorial hologram[86, 87] in which polarization information is arbitrarily redistributed on an image plane, as shown in Fig.2.12 (a). Specifically, a meta-optic that accepts unpolarized incident light and redistributes the energy, based on polarization, to realize a “V” logo is exhibited. The detailed

phase profile, as well as the rotation angle of the meta-atoms, can be found in Appendix B.5. In Fig.2.12 (b) and (c), I present the optical and SEM images of the fabricated metasurfaces. The polarization distribution after the meta-optic was characterized using a linear analyzer, as shown in Fig.2.12 (d) and (e), demonstrating excellent agreement between the simulated and measured results. The diffraction efficiency, defined by the overall transmission over total input energy, was measured to be 83.0%.

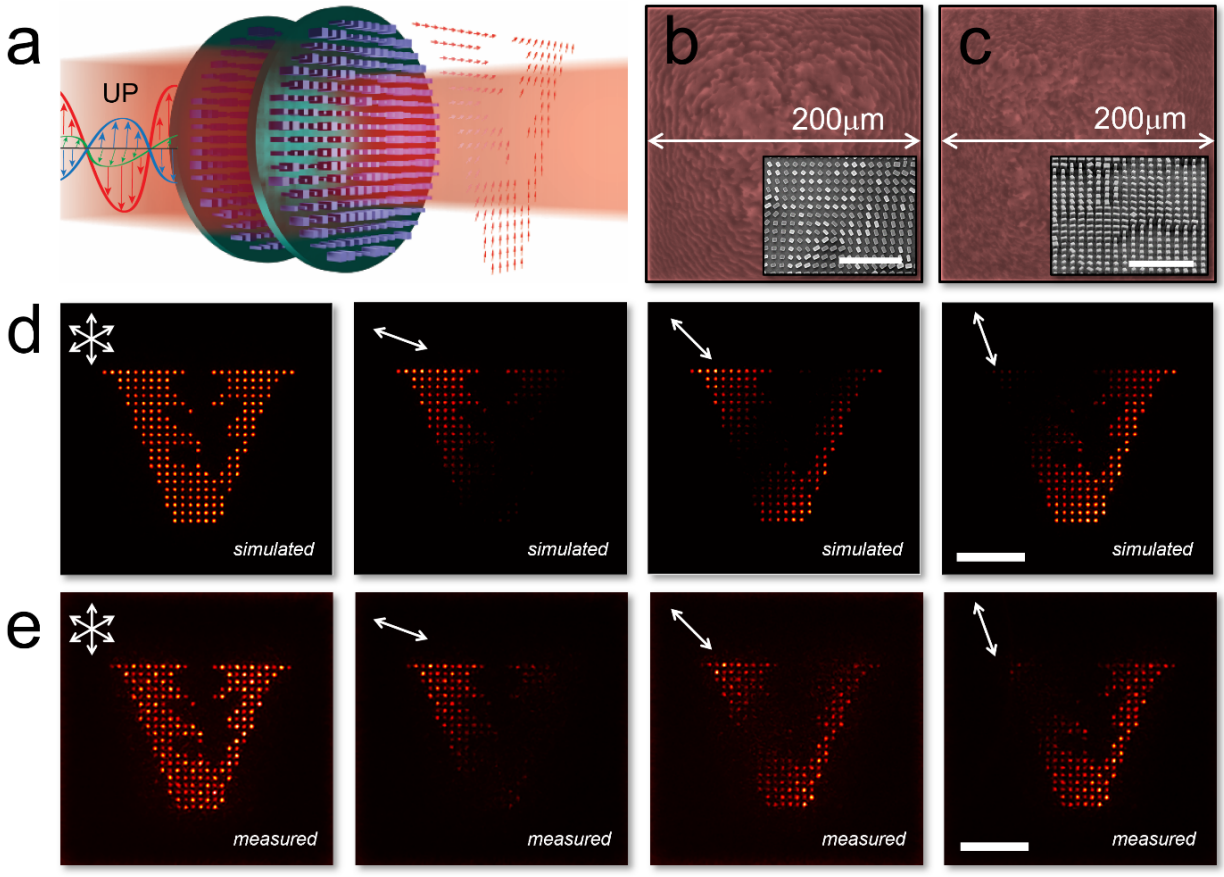

Figure 2.12 Meta-optic-based vectorial hologram. (a) Schematic of the multi-layer meta-optic for the vectorial hologram to unpolarized beams. (b) and (c) Optical images of each metasurface in the meta-optic. The insets are SEM images of metasurfaces. Scale bar: 4μm. (d) and (e) Simulated and measured polarization-dependent intensity distributions after the meta-optic. An unpolarized supercontinuum laser was used as the source. The upper-left corner arrows indicate the analyzer orientation. From left to right, the analyzer state is unpolarized, 15°, 45°, and 75° polarized to the *x*-axis. Scale bar: 50μm.

The vectorial hologram devices manipulate the orthogonally polarized amplitude as well

as polarization conversion efficiency, providing a powerful toolbox for optical systems design, which may find applications in a variety of areas. The cascaded architecture and the ability to redistribute light across the aperture enable opportunities in optical computing, such as neural networks[88], where low-loss spatial control over the output field is necessary. Meanwhile, complete control over the coherent vector field along orthogonal axes can be used for quantum entanglement[89] with spin and orbital angular momentum encoded in the optic. Furthermore, high-efficiency and arbitrary spatial mode manipulation allow for optical multiplexing and division for use in multichannel displays[45] and information encryption[90, 91].

2.6 Conclusion

In this chapter, I have demonstrated compound meta-optics consisting of paired, lossless metasurfaces that independently manipulate the amplitude and phase as well as the polarization state of an optical field. Each metasurface was implemented as a high-transmission array of amorphous silicon nanopillars and aligned, operating at near-infrared wavelengths. The distance between the metasurfaces allows the optical wave to be reshaped, leading to high-efficiency devices by avoiding loss-based amplitude-control mechanisms. High-efficiency field control expands the application space of meta-optics, while maintaining a compact form factor. As examples, I have experimentally shown that compound meta-optics can implement optical functions such as combined beamformer and splitter, as well as form 3-dimensional holograms with high image quality. In each case, the measured efficiency of the fabricated meta-optic devices ranged between 65~75%. By explicitly forming the desired complex-valued field profiles, no energy is lost to diffraction, and high-quality holograms are obtained.

Additionally, polarization control can be achieved through an anisotropic nanopillar cross-section. Assisted with an end-to-end optimization method based on a state-of-the-art machine

learning platform, the manipulation efficiency of the compound meta-optic system can be further enhanced to over 80%. Compound meta-optics could lead to improved performance in three-dimensional holography, compact holographic displays, custom optical elements, vectorial field control, and other applications requiring detailed control over the phase, amplitude, and polarization distributions of an optical field, which can pave a new avenue for the next generation of the nanophotonic platform.

Chapter 3

Meta-optic Accelerators for Object Classifiers

3.1 Introduction

Digital neural networks (NNs) and the availability of large training datasets have allowed for rapid progress in the performance of machine-based tasks for a wide range of applications, including image analysis[92, 93], sound recognition[94, 95], and natural language translation[96]. The enhanced capability has, however, come at a computational cost as increased complexity and accuracy have necessitated the need for ever larger deep neural networks (DNNs)[97]. The ever-increasing computational requirements of DNNs have resulted in unsustainable growth in energy consumption and restrictions in real-time decision-making when large computational systems are not available.

One alternative to DNNs is the use of optical processors that have the advantages of ultra-fast processing times and low energy costs[98, 99, 100]. These systems can be employed as stand-alone processors and/or as front-end accelerators for digital systems as shown in Fig.3.1. In either case, optical systems are most impactful when used for the linear matrix-vector multiplications[101, 102] that comprise the convolution operations in DNNs. These operations are often the most computationally burdensome components typically comprising more than 90% of the required floating-point operations (FLOPs) in popular CNNs[103, 104]. There are both free-space[105, 106, 107] and chip-based[108, 109] approaches to optical processors but in either case, the computational advantage is achieved via the massively parallel and low-power processing that is possible with optics. In the case of image analysis, free-space approaches are attractive as spatial multiplexing can be readily achieved[75, 110, 111] as well as the fact that an optical front-end can potentially be integrated directly

with an imaging system[50, 112].

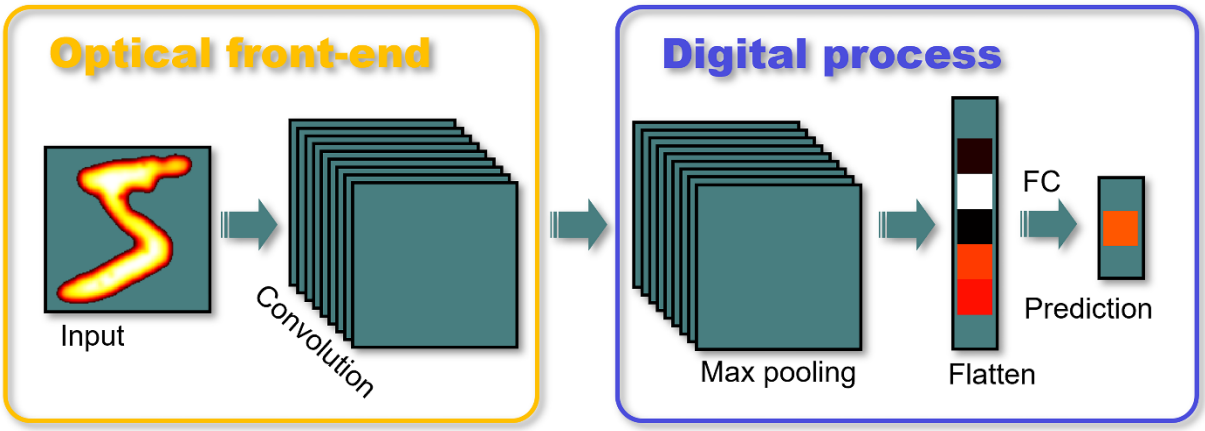

Figure 3.1 The Schematic of a convolutional neural network. The optical front-end performed object capturing as well as convolution process based on the optical operations.

The most traditional approach to free-space based optical image processing is the use of 4*f* optical correlators where spatial filters[113, 114, 115, 116], either passive or dynamic, are placed in the Fourier plane of a 2-lens optical system. Recorded spatial features are then fed to a lightweight digital NN back-end for classification. An alternative approach is the use of diffractive neural networks which utilize cascaded diffractive elements as convolutional layers[117, 118, 119]. Image classification is realized through redistribution of optical energy on the detector plane requiring minimal digital processing. The tradeoff is the need for several diffractive layers as well as coherent illumination, precluding use with ambient lighting. While these approaches have shown benefits in terms of processing speed and energy consumption, they necessitate enlarged imaging systems. Furthermore, none of these approaches utilize the additional information channels, such as polarization, that are available when utilizing an optical front-end[63, 120].

In this chapter, I demonstrate the use of meta-optic based optical accelerators that serve as the convolutional front-end for a hybrid image classification system as shown in Fig.3.2. Spatial

multiplexing is achieved by using a multi-channel metalens for image duplication and a metasurface-based convolutional layer. This system has the advantage of being compact while the use of metasurfaces allows for additional information channels, in this case, polarization, to be accessed enabling both image and polarization-based classification. The hybrid network utilizes end-to-end design such that the optical and digital components are co-optimized while also incorporating statistical noise resulting in a robust classification network. I experimentally demonstrate the classification of the MNIST dataset with an accuracy of 93.1% as well as 93.8% accurate classification of polarized MNIST digits. Due to the compact footprint, ease of integration with conventional imaging systems, and ability to access additional information channels, this type of system could find uses in high-dimensional imaging, information security, and machine vision.

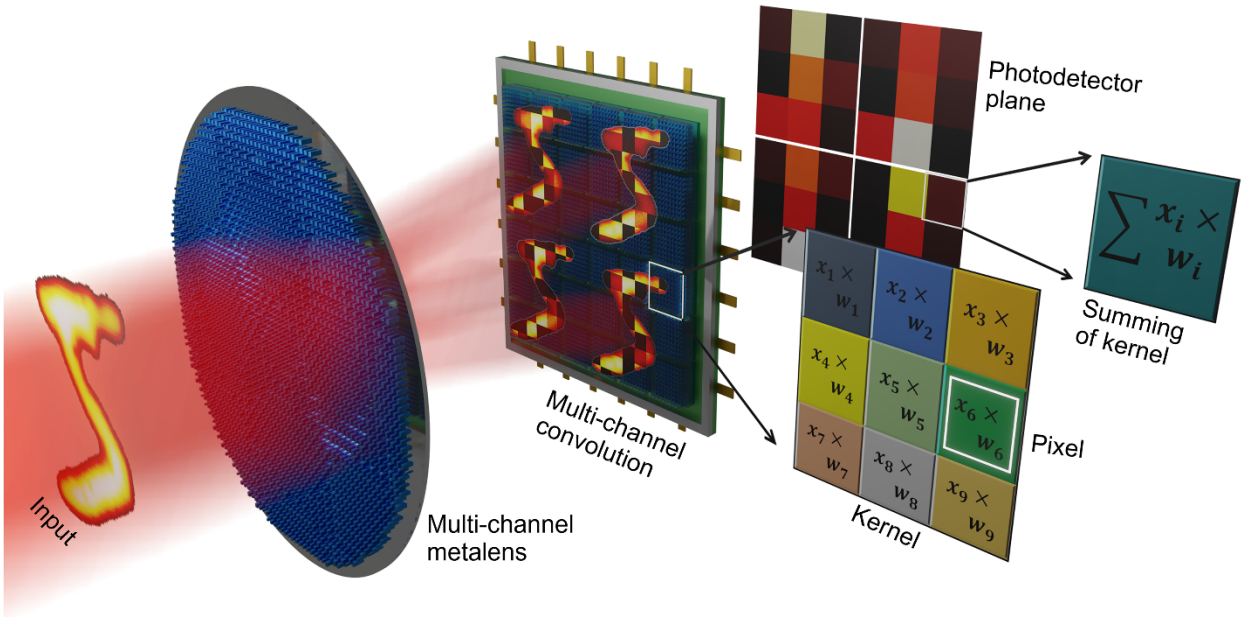

Figure 3.2 Schematic of the meta-optic accelerator. The meta-optic enables multi-channel signal processing for replacing convolution operations in a digital neural network. Summing is achieved by each kernel being recorded by a single pixel on the photodetector.

3.2 Meta-optic Accelerators for Convolutional Neural Network

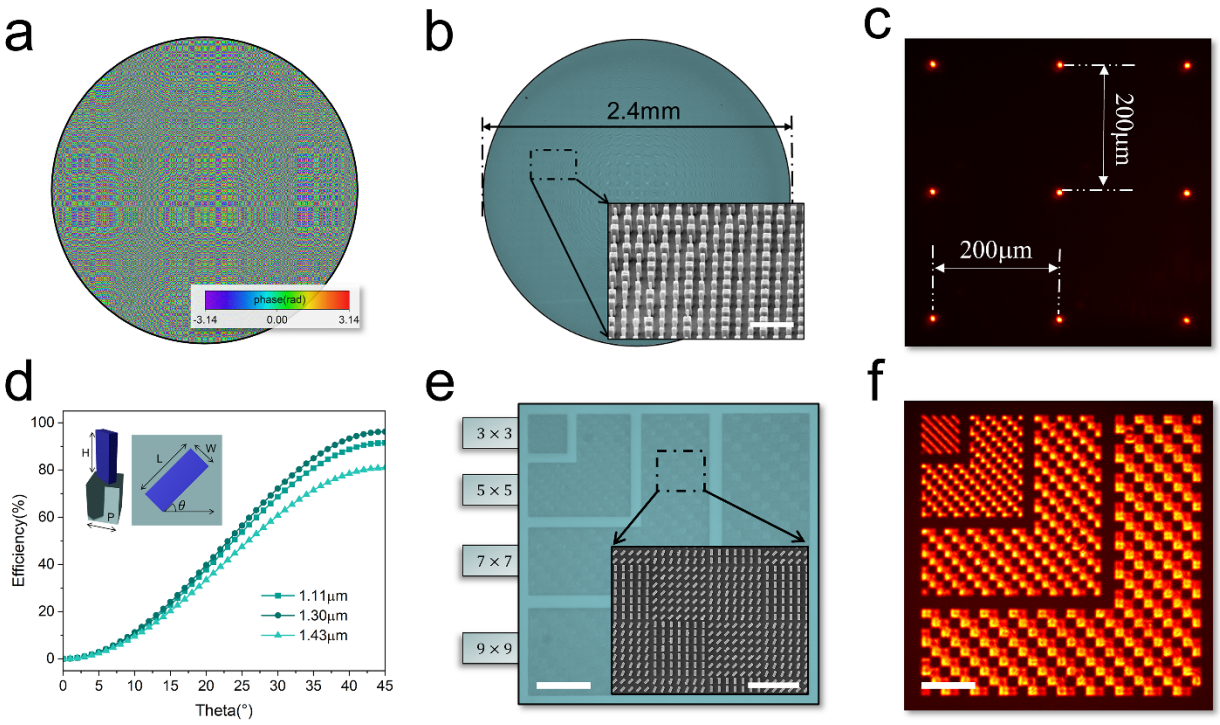

Figure 3.3 Components of the meta-optic system. (a) The phase profile of the multi-channel metalens was achieved using spatially multiplexed meta-atoms. (b) Optical image of the fabricated multi-channel metalens. The inset is an SEM image of the lens. Scale bar: 2μm. (c) Experimental focal spot profile of the multi-channel metalens under illumination at a wavelength of 1.3μm. (d) Polarization conversion efficiency as a function of the meta-atom rotation angle. (e) Optical image of kernel resolution test chart. The left-side bar shows the number of meta-atoms in each kernel pixel. Inset is an SEM image of the meta-atoms. Left scale bar: 30μm. Right scale bar: 4μm. (f) Optical transmission of the kernel resolution test char under tungsten lamp illumination. An orthogonal analyzer was used to image the transmission map. Scale bar: 30μm.

The meta-optic accelerator is made up of two metasurfaces, a platform due to the fact that it offers precise wavefront, complex-amplitude, and polarization state manipulation in an ultra-thin form factor. Metasurfaces have also been utilized as standalone systems for all-optical image processing, namely, edge detection, through manipulation of the non-local, angle-dependent response. In the meta-optic accelerator's design, the first metasurface is a multi-channel metalens that duplicates an object into nine images. The multi-channel metalens was created using 9 meta-atoms per super-cell to create images at 9 spatial locations. The lens was created with a hyperbolic

phase profile where the phase delay of each resonator, i, in the supercell is given by,

$$\phi_i = \frac{2\pi}{\lambda}\left(f - \sqrt{f^2 + (x - a_i)^2 + (y - b_i)^2}\right) \tag{3.1}$$

where f is the focal length, λ is the working wavelength, and x and y are the spatial positions on the lens. a and b correspond to the displacement of each unique focal spot, i, from the center of the lens. The resulting phase profile, for a 2.4 mm diameter metalens, is shown in Fig.3.3 (a). The metalens was realized using cylindrical silicon nanopillars with a period of 0.6μm and a height of 0.88μm (See meta-atoms details in Appendix C.1). The width of each meta-atom was chosen such it provides the phase profile given by Eq.3.1.

All the metasurfaces fabrication is completed by the EBL-based standard lithography technique. The fabrication process is described as follows. First, plasma-enhanced chemical vapor deposition was used to deposit an 880nm thick silicon device layer on a quartz substrate. PMMA photoresist was spin-coated on the silicon layer followed by evaporation of a 10nm thick Cr conduction layer. EBL patterning was performed and after removing the Cr layer, the exposed pattern was developed. A 50nm Al_2O_3 hard mask was deposited via electron beam evaporation, followed by lift-off. The silicon was then patterned using reactive ion etching, and a 1μm thick layer of PMMA was spin-coated to encase the nano-pillar structures in a protective and index-matching layer.

An optical image of the meta-lens is shown in Fig.3.3 (b) with the inset showing the individual meta-atoms. The experimentally recorded focal spots demonstrate diffraction-limited performance, as shown in Fig.3.3 (c). While spatial multiplexing is used here to create the multi-channel lens, it is worth noting that the design method is not unique. As additional channels are added, a spatially multiplexed lens will suffer from higher-order diffraction and resolution reduction due to a larger super-cell structure. One way this can be overcome is through the use of

complex-valued amplitude control that eliminates the need for spatial multiplexing, which will be discussed in a later section.

The second metasurface serves as a multifunctional kernel layer that provides the vector-matrix multiplication operations. The kernels are based on Pancharatnam-Berry metasurfaces that can encode polarization and/or amplitude information for convolution with the image. The transmission of each rectangular nanopillar comprising the metasurface follows an analytical model based on the Jones matrix given by

$$\begin{bmatrix} E_{x,out} \\ E_{y,out} \end{bmatrix} = \begin{bmatrix} cos(\theta) & sin(\theta) \\ -sin(\theta) & cos(\theta) \end{bmatrix} \begin{bmatrix} e^{i\phi_x} & 0 \\ 0 & e^{i\phi_y} \end{bmatrix} \begin{bmatrix} cos(\theta) & -sin(\theta) \\ sin(\theta) & cos(\theta) \end{bmatrix} \begin{bmatrix} E_{x,in} \\ E_{y,in} \end{bmatrix} \tag{3.2}$$

Here $E_{x,in}$, $E_{y,in}$ and $E_{x,out}$, $E_{y,out}$ are the x and y polarized incident and transmitted amplitude. ϕ_x and ϕ_y are the phase shifts provided by the resonator for x and y polarization. θ is the pillar rotation angle. The kernel pattern is discretized to allow for a memory-efficient architecture and one that is compatible with a dynamically reconfigurable system where pixelization is necessary due to practical limits on control electronics. In order to control the weights in each kernel, linearly polarized illumination was utilized, combined with an orthogonal polarizer serving as an analyzer that is placed in front of the camera. The rotation angle of each meta-atom, θ, dictates the percentage, or weight, of the incident light that has had its polarization vector rotated by 90°, thus passing the analyzer. To achieve amplitude manipulation, spatial variations in ϕ_x and ϕ_y are not needed and were fixed as $|\phi_y - \phi_x| = \pi$ to simplify the model. In the case of x-polarized incident light, the intensity of y-polarized transmitted light is given by,

$$I_{y,out} = sin(2\theta)^2 \cdot I_{x,in} \tag{3.3}$$

where $I_{x,in}$, $I_{y,in}$ and $I_{x,out}$, $I_{y,out}$ are the x and y polarized incident and transmitted intensities, respectively. The use of pillar rotation for controlling kernel weight has the advantage of being

broadband while also allowing for precise control over the weight, as rotation is readily controlled in the lithography process. Fig.3.3 (d) displays the transmission, $T_{yx} = I_{y,out}/I_{x,in}$ as a function of rotation angle and wavelength, revealing a 320nm bandwidth where there is less than a 10% variation in transmission. In this approach, either the camera pixel size or the kernel size, determines the maximum areal density of neurons. In the case of the kernel, the meta-atoms in each pixel of the kernel are designed as being periodic. Thus, as the number of meta-atoms in each uniform pixel is reduced, there will be a deviation in the weight as the boundaries of the pixels, where periodicity is broken, play a larger role. In Fig.3.3 (e) and (f), I characterize the role of pixel size on the accuracy of the designed weight using 3×3 pixel kernels and find that a minimum pixel size of 0.2 pixels / λ^2 is possible based on a maximum weight error of 10% where λ is the working wavelength.

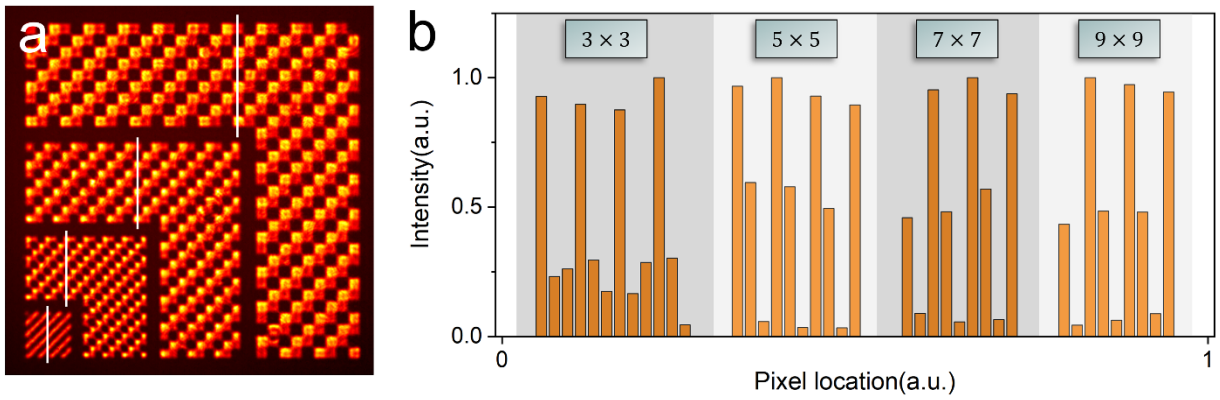

Figure 3.4 Characterization of metasurface-based kernel resolution. (a) The field profile of the test kernel. The white lines indicate the extracted data in (b). The data were extracted according to different meta-atoms numbers in each kernel element. (b) The quantitative description of kernels as a function of meta-atoms number is each kernel element. The top labels indicate the meta-atoms arrangements in a single kernel pixel.

The quantitative analysis of kernel accuracy as a function of size can be found in Fig.3.4. The kernel comprised weights of 0, 0.5, and 1 arranged in a checkboard layout as shown in Fig.3.4 (a). Under the illumination of a tungsten lamp, the transmission was measured using a camera. The

weight of each kernel, measured along the white lines, is displayed in Fig.3.4 (b). It was found that the metasurface weight error is less than 10% when the number of meta-atoms in each kernel is larger than 5×5. Hence, illumination at a wavelength of 1.3μm yields a minimum pixel size of 3μm×3μm (5×5 meta-atoms) or ~1×10^5 pixels/mm^2. This can be compared to state-of-the-art spatial light modulators (DLP650LNIR, Texas Instruments Inc.) where pixel sizes are on the order of 10.8μm×10.8μm yielding 9×10^3 pixels/mm^2. Understanding the minimum metasurface pixel size is important for reconfigurable metasurface kernel layers as weight must be accurately controlled regardless of the kernel pattern.

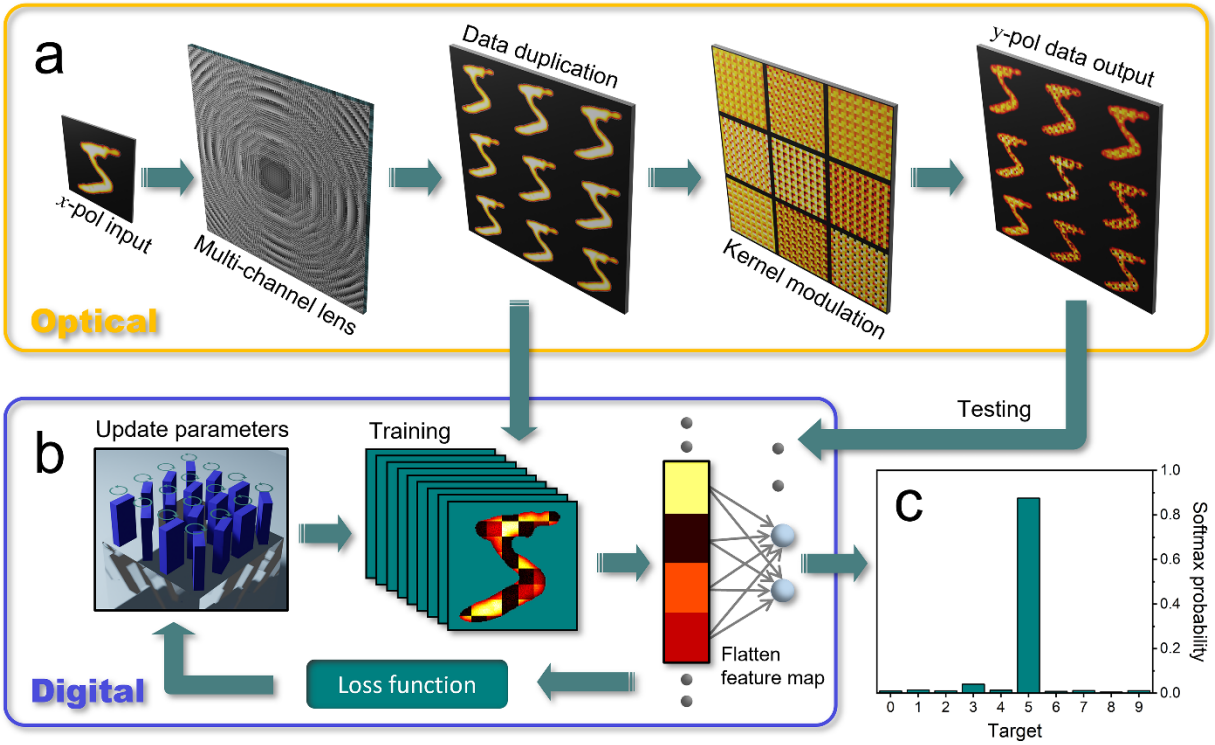

Figure 3.5 Workflow of the meta-optic accelerator design and testing process. (a) The metalens, with 9 independent channels, splits the image. In training, these images are recorded on the camera and used for training the optical kernel layer and digital systems. Once the kernel layer is trained, it is inserted into the system, and the images are then projected onto that layer generating 9 feature maps that are recorded on the camera (b) The digital loop comprises an iterative training process in which the Jones matrix is used for forward propagation. (c) The probability histogram is the final output for image classification.

In order to design the weights and geometry of the kernel layer, an end-to-end design was

employed where both the digital and optical systems are co-optimized as shown in Fig.3.5. The system was designed for the classification of 24×24 pixel MNIST digits using the 9 unique channels provided by the metalens, each channel comprising 3×3 pixel kernels with a stride of 3. We employ a shallow digital neural network comprising 2 fully connected layers with a ReLU function in between. In this architecture, 50% of the overall FLOPs are implemented by the meta-optic accelerator. An optical front-end imposes unique constraints on the design of hybrid neural network structures as there are several noise sources in the analog signal being input and output, from the optical system. The main sources of noise in our system come from stray light, detector noise, image misalignment due to variations in the optical system, aberrations from off-axis imaging system and fabrication imperfections in the metalens and kernel layers. To better understand these noise sources, and validate the designs for statistically relevant data sets, I used the imaging system in Appendix C.2 to project the 24×24 pixel MNIST digits as the design reference. The SLM was imaged, using the meta-optic without kernel layer, onto an InGaAs focal plane array that was triggered by the SLM such that large numbers of images could be recorded in an automated fashion.

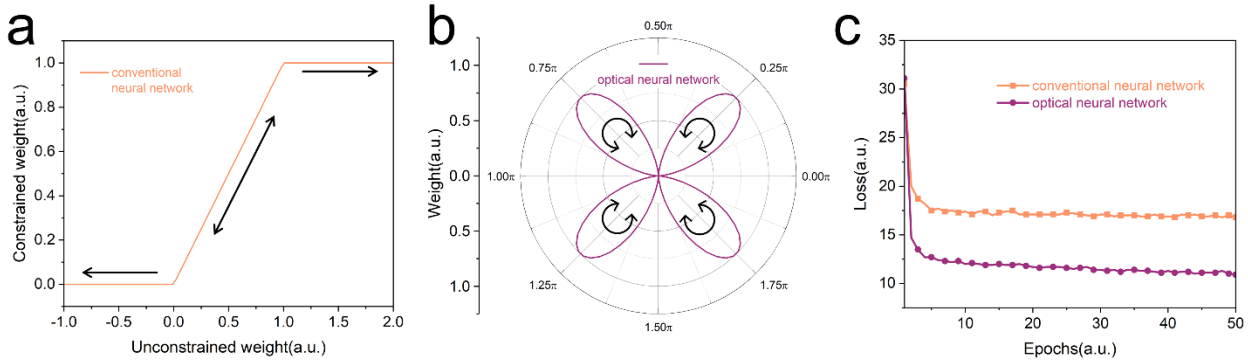

Figure 3.6 Comparison between conventional and optical neural networks. (a) and (b) The weight evolution for conventional and optical neural networks, respectively. (c) The loss evolution for conventional and optical neural networks as a function of training epochs.

To account for noise in the projection, imaging, and detector systems the 10,000 training images from the MNIST dataset were projected and recorded using the metalens as the imaging optic, without the kernel layer, as shown in Fig.3.5 (a). The optically recorded data were used as the training data in the end-to-end design loop. In the training process, I incorporated 10% spatial intensity fluctuation in the kernel layer and random image rotation within ±3 degrees. The feature maps, which correspond to the convolution of the metasurface kernel layer with each of the 9 images, were fed into the trainable model to form a mean-square-error (MSE) loss function as shown in Fig.3.5 (b). The backward propagation comprised a stochastic gradient descent (SGD) based algorithm driven by the loss function to update the physical parameters (ϕ_x, ϕ_y and θ) of metasurface kernel layer for each iteration. The physical model, based on the Jones matrix, is used in forward propagation during design, and thus the evolution of the kernel weight is continuous with rotation angle, θ. Without the use of the physical model, one would have to clamp the weights in order for the transmission to be restricted to the physically attainable range of 0 to 1. Ultimately, the continuous weight evolution enabled by the physical model was found to result in more accurate classification by avoiding local minimum during the training of the network as shown in Fig.3.6.

The detailed architecture of the designed hybrid neural network is depicted in Fig.3.7. In order to develop the machine learning platform, training data was first generated by projecting, and imaging, the 10,000 training images from the MNIST data library. The 9 optical images generated from the multi-channel metalens were recorded at 512×640 resolution and then each image was down-sampled to 24×24 pixels. In training of the digital and optical components of the network, an Adam optimizer was utilized with the learning rate set as 0.001. Training occurred over 50 epochs to obtain stable accuracy. Here we proposed two kinds of models, where model1

is utilized for amplitude-only object classification while model2 is used for multi-functional (amplitude and polarization) image recognition, which will be discussed in the next section. For both models, we employ shallow neural network architectures with minimal numbers of digital layers, among which, ~50% of the overall FLOPs are moved into the optical layer. The FLOPs of each layer in the neural network were calculated in the following table 3.1. The highlighted area indicates the operations performed by optical metausrface.

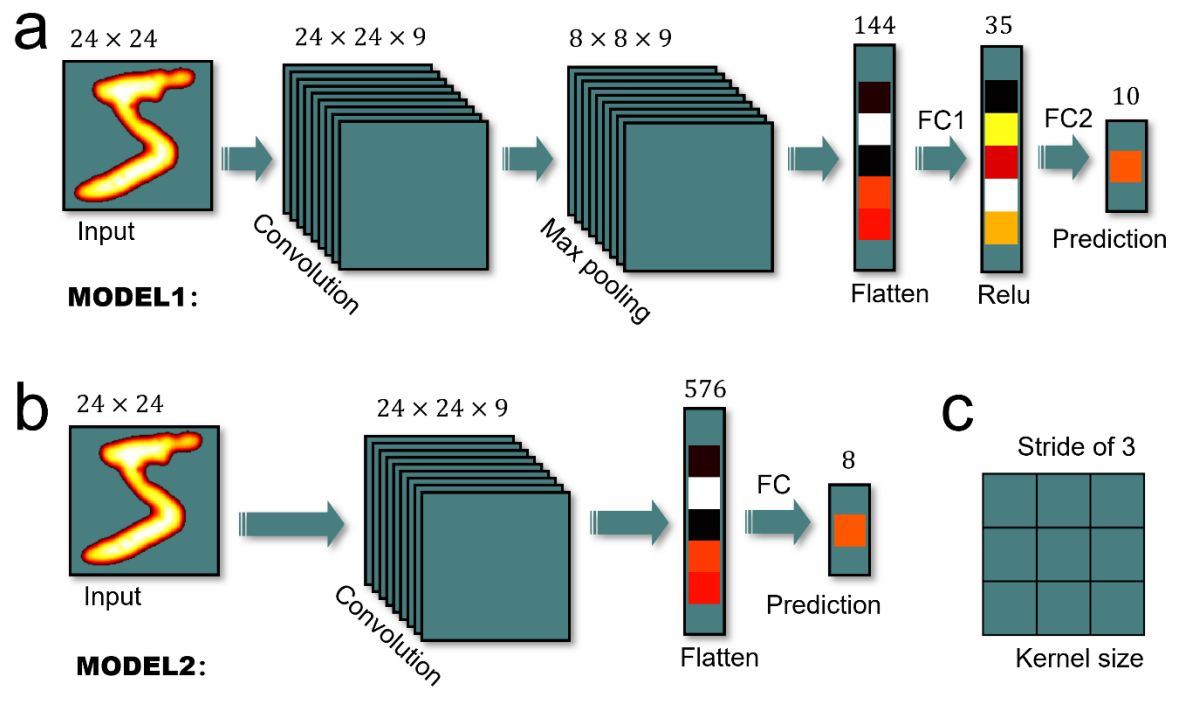

Figure 3.7 The digital neural network architecture used in the manuscript. (a) The neural network for amplitude-only object recognition. (b) The neural network process for polarized object classification. The label above indicates the input neuron numbers of each layer. (c) The size and stride number of kernel for convolution.

Once training of the system was complete, the metasurface kernel layer was fabricated by the EBL-based standard lithography process as discussed previously. The metasurface kernel layer was then imaged using uniform illumination and compared to the theoretical design, both of which are included in Fig.3.8 (a) and (b). The fabricated and designed kernels show agreement with a

standard deviation of less than 10%, which matches the noise level in the training model. The kernel layer was then placed in the image plane of the metalens for recording convoluted images from the testing dataset. Fig.3.8 (c) shows the feature map produced for a digit of "0". Each kernel pixel comprises an 11×11 (6.6μm×6.6μm) meta-atom array. Summing of each kernel could be achieved optically via alignment of each kernel with an individual pixel on the camera. However, in this work, summing is performed digitally as the kernel layer is magnified when imaged onto the camera such that each kernel comprises multiple camera pixels.

	Operations	FLOPs
MODEL1	Convolution	2 × Channel × Kernel shape × Output shape = 10368
	Max pooling	(Height / Stride) × Depth × (Width / Stride) = 144
	Fully connected layer 1	2 × Input size × Output size = 10080
	Fully connected layer 2	2 × Input size × Output size = 700
MODEL2	Convolution	2 × Channel × Kernel shape × Output shape = 10368
	Fully connected layer	2 × Input size × Output size = 9216

Table 3.1 FLOPs of proposed neural network architecture

In order to characterize the system's performance, 1000 digits, not in the training set, were recorded using the meta-optic. The theoretical and experimental confusion matrices for this testing dataset are shown in Fig.3.8 (d) and (e), respectively. The theoretical training model's overall accuracy was 94.7%, while the experimental accuracy was 93.1%. To validate the significance of the optical convolution layer, two types of reference experiments were performed, one with no convolution layer and one with random kernel values, both based on the same neural network

architecture as used with the meta-optic front-end. The removal of the convolution layer resulted in a model accuracy of 79.2%, while random kernel values resulted in an accuracy of 79.7%, illustrating the significance of end-to-end design and the meta-optic front-end.

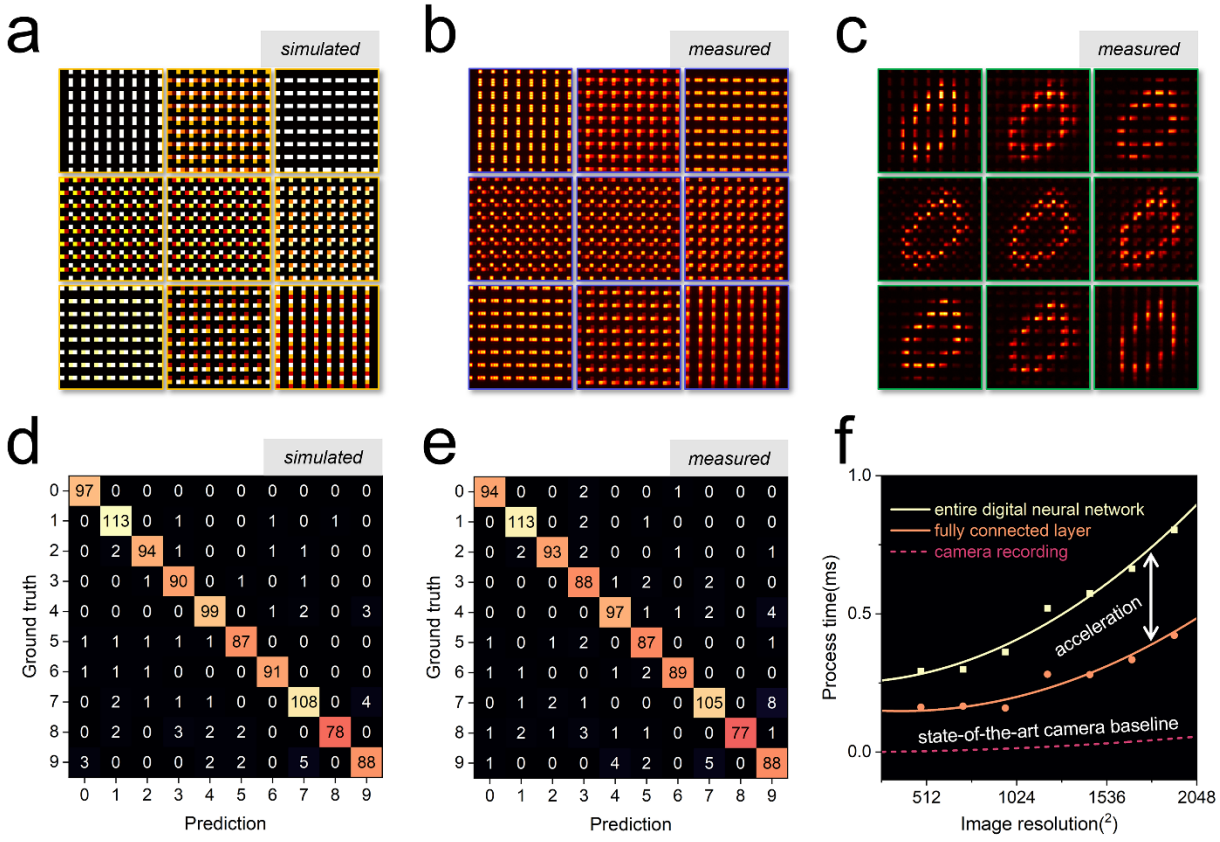

Figure 3.8 Classification of MNIST digits. (a) Transmission (weights) of the ideal kernels after the training process. (b) Measured transmission of the fabricated channels. An incoherent light source, filtered at 1.3μm, was used for illumination. (c) The nine feature maps were recorded on the camera. (d) and (e) is the theoretical and measured confusion matrices for MNIST object classification, respectively. (f) The acceleration by optical convolution in neural networks as a function of input image resolution. The state-of-the-art camera baseline indicates the image recording speed by Phantom TMX 7510.

Although this proof-of-concept demonstration involves low-resolution images, the small minimum pixel size of the kernel layer along with the parallel nature of the optical operations means that this architecture could be a powerful tool for high-speed and large-scale image processing applications. In Fig.3.8 (f) I benchmark system performance based on both the all-

digital and hybrid networks recording images with a state-of-the-art camera (Phantom TMX 7510) and the same network architecture and hardware platform. The hybrid network is accelerated due to the passive and parallel convolution operations provided by the metasurface with gains increasing with raising of image resolution. Moreover, the versatility of the system can be further improved by the incorporation of dynamically tunable metasurfaces as the kernel layer such that the optical front-end can be reconfigured or temporally multiplexed.

3.3 Meta-optic Accelerators for Multifunctional Classification

One of the unique strengths of metasurfaces, compared to conventional lenses or diffractive optical elements, is their ability to provide user-specified amplitude and phase functions while also being sensitive to the polarization state and wavelength of light. This allows for access to additional information carriers that are normally lost when recording an image on a camera, allowing one to discriminate based on normally hidden features in the physical world such as vectorial polarization, phase gradients, or spectrally complex signals. To demonstrate this ability, a polarized MNIST dataset with 8000 images was created comprising four digits (1, 4, 5, 7) with each digit having two orthogonal polarization states, as shown in Fig.3.9 (a).

In this case, a single fully connected digital layer, without ReLU, was utilized for classification (see Fig.3.7 model2). Polarization classification is possible due to the fact that the meta-atoms, outlined in Fig.3.3 (d), have a transmitted intensity that is dependent on the incident polarization state, given by,

$$I_{y,out} = cos(2\theta)^2 \cdot I_{y,in} + sin(2\theta)^2 \cdot I_{x,in} \tag{3.4}$$

where $I_{x,in}$, $I_{y,in}$ and $I_{y,out}$ are the x and y polarized incident and transmitted intensities, and θ is the meta-atom rotation angle.

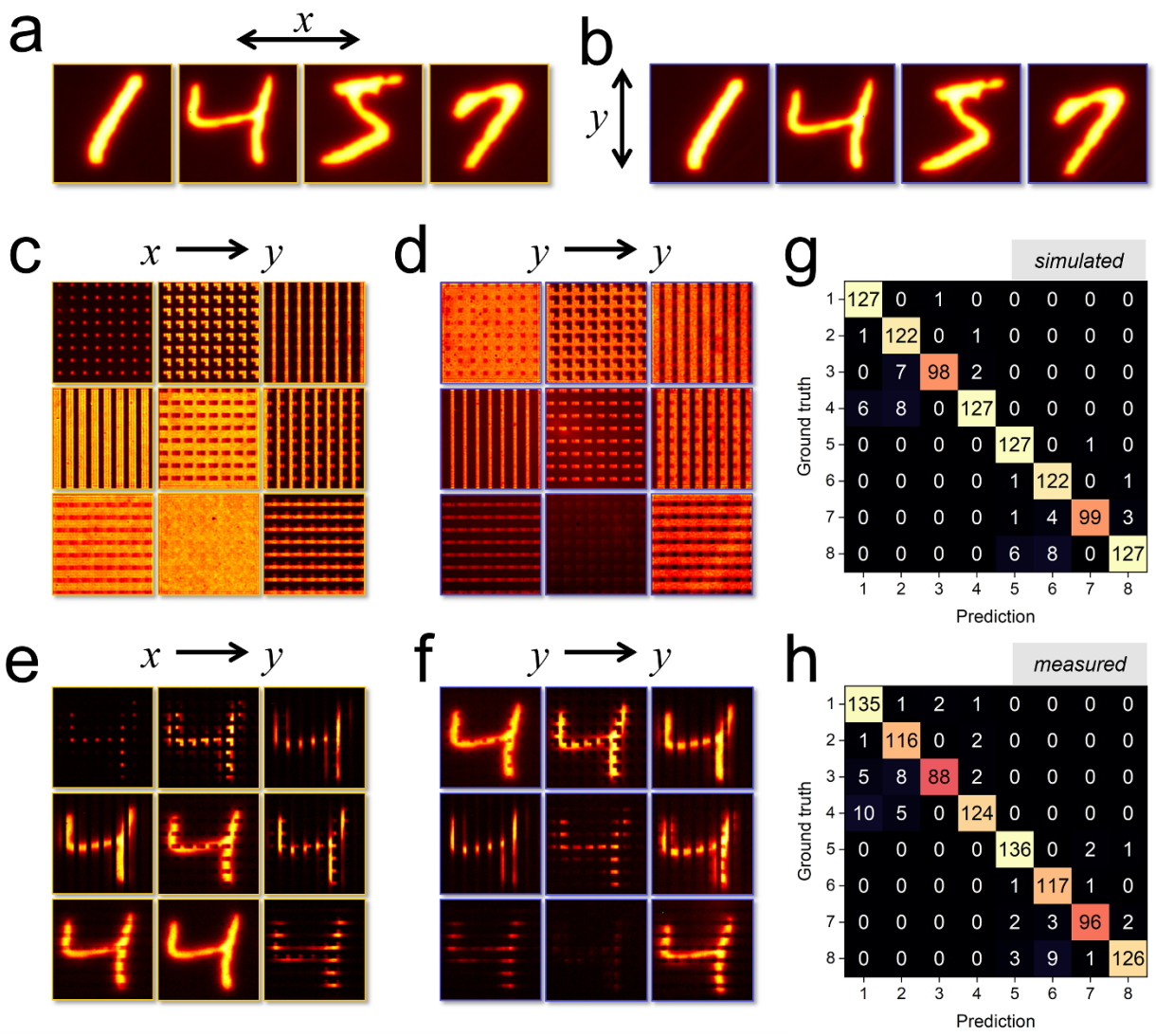

Figure 3.9 Demonstration of multi-functional object classification. (a) and (b) illustrate the digits for classification, which carry both amplitude and polarization information. (c) and (d) is the transmission profiles of the fabricated metasurface channels under incoherent, 1.3μm wavelength, illumination with orthogonal linear polarization states. (e) and (f) are feature maps for identical digits with *x* and *y*-polarization, respectively. (g) and (h) are the theoretical and measured confusion matrices, respectively.

While the output signals between the *x* and *y* polarized channels are correlated, the mechanism for polarization recognition is independent of object classification and the latter requires feature map analysis provided by the convolution process. In the case of polarization, the birefringence of the meta-atoms enables the conversion of the polarization state to an intensity value. The intensity arising from the polarization state is constant across the channel and is

completely independent of the spatially varying amplitude value. Hence, both functions, polarization and amplitude classification, can be integrated into a single meta-optic for multifunctional analysis. The optical kernel layer was designed following the training procedure outlined in Fig.3.5 with the system tasked with classifying eight output states comprising the four distinct digits, each with *x* and *y* polarization states.

The metasurface kernel layer was formed from rectangular nanopillars using the same geometry and fabrication process as described previously. In Fig.3.9 (c) and (d) the transmitted intensity, $I_{y,out}$, is provided for a uniformly illuminated kernel layer with both *x* and *y*-polarization states and Fig.3.9 (e) and (f) provide the feature maps for an identical digit with *x* and *y*-polarization states. Both the uniformly illuminated kernels and feature maps demonstrate the contrast in the convolution for orthogonal polarization states. Fig.3.9 (g) and (h) provide the theoretical and experimental confusion matrices, respectively, for 1000 test images not in the training dataset. The theoretical accuracy of classification was 94.8% shown, while the experimental accuracy was 93.8%, showing excellent agreement. It is worth mentioning that in the confusion matrix, the neural network system has a 100% accuracy on polarization state recognition. A more complex, non-orthogonal signal recognition design can also be found in Appendix C.3 to demonstrate the robustness and flexibility of the proposed meta-optic platform.

3.4 Complex-amplitude Manipulation for Object Classifier

In section 3.2, I demonstrated a 3×3 multi-channel metalens based on spatial multiplexing of the unit cells. In this case, higher diffraction orders will be problematic as the number of channels is increased. To create arbitrary numbers of channels while eliminating higher diffraction orders, complex-valued amplitude control of the output field is necessary. A complex-amplitude metalens with 25 output channels is exhibited in Fig.3.10. The complex-valued field

profile can be described by the following equation,

$$F[\alpha(x,y),\phi(x,y)] = \sum_i^n \exp\left[\quad i\cdot\frac{2\pi}{\lambda}\left(f-\sqrt{f^2+(x-a_i)^2+(y-b_i)^2}\right)\right] \tag{3.5}$$

where f is the focal length, λ is the working wavelength, and x and y are the spatial positions on the lens. a and b correspond to the displacement of each unique focal spot, i, from the center of the lens. F is the complex-amplitude field composed of α (amplitude) and ϕ (phase) information.

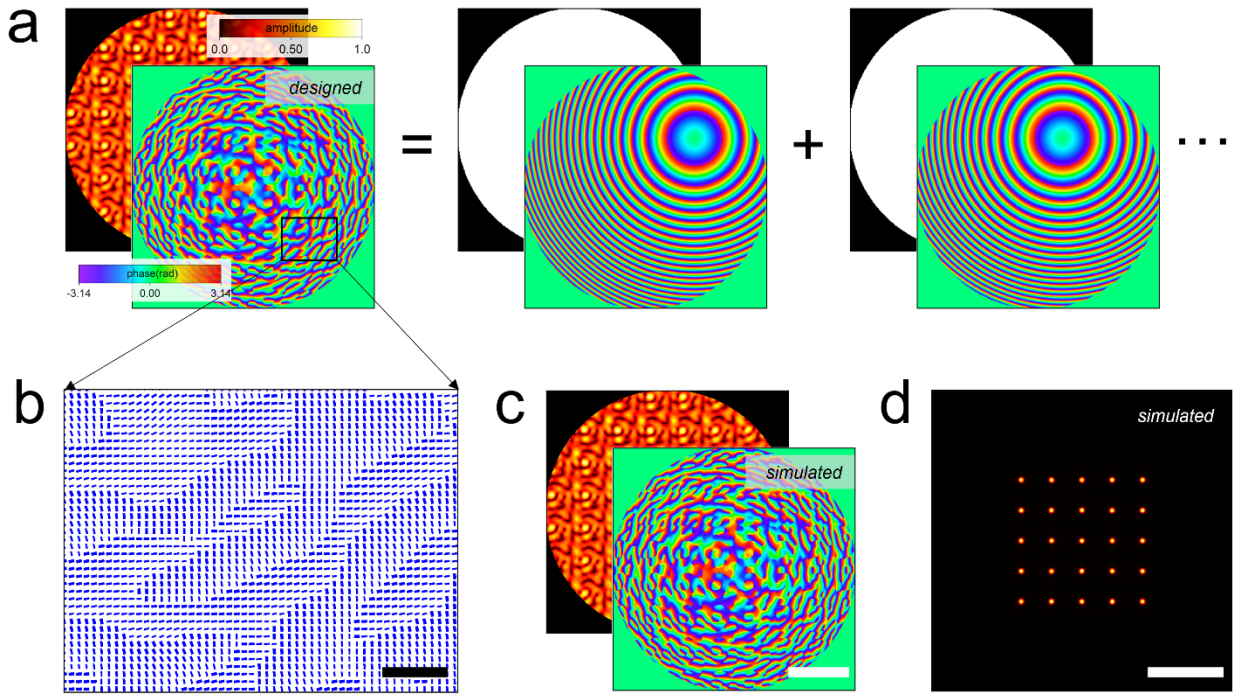

Figure 3.10 The complex-amplitude manipulation method for multi-channel metalens. (a) The design process for multi-channel metalens with arbitrary information channels. (b) The schematics of metasurface profiles to construct the complex-amplitude profile in (a). Scale bar: 5μm. (c) The reconstructed complex-amplitude profile based on calculated meta-atoms data library. Scale bar: 50μm. (d) The calculated focal spot profile of the multi-channel metalens based on complex-amplitude values in (c). Scale bar: 50μm.

In Fig.3.10, I present the design and simulation of a 5 × 5 multi-channel metalens based on this method. The ideal complex-amplitude field for the multi-channel metalens is shown in Fig.3.10 (a). To reconstruct this field, the nanopillars discussed in section 3.2 were employed and the phase, as well as rotation angle of each meta-atom, is dictated by the equations in Appendix

A.2. The required geometrical data for the metasurface is then extracted from the data library and exhibited in Fig.3.10 (b). The reconstructed complex-amplitude field, displayed in Fig.3.10 (c), shows an excellent match with the designed target field. The focal spot profile was calculated based on the angular spectrum propagation method[2] and is shown in Fig.3.10 (d), demonstrating independent multi-channel imaging.

3.5 Comparison between Hybrid and Diffractive Neural Networks

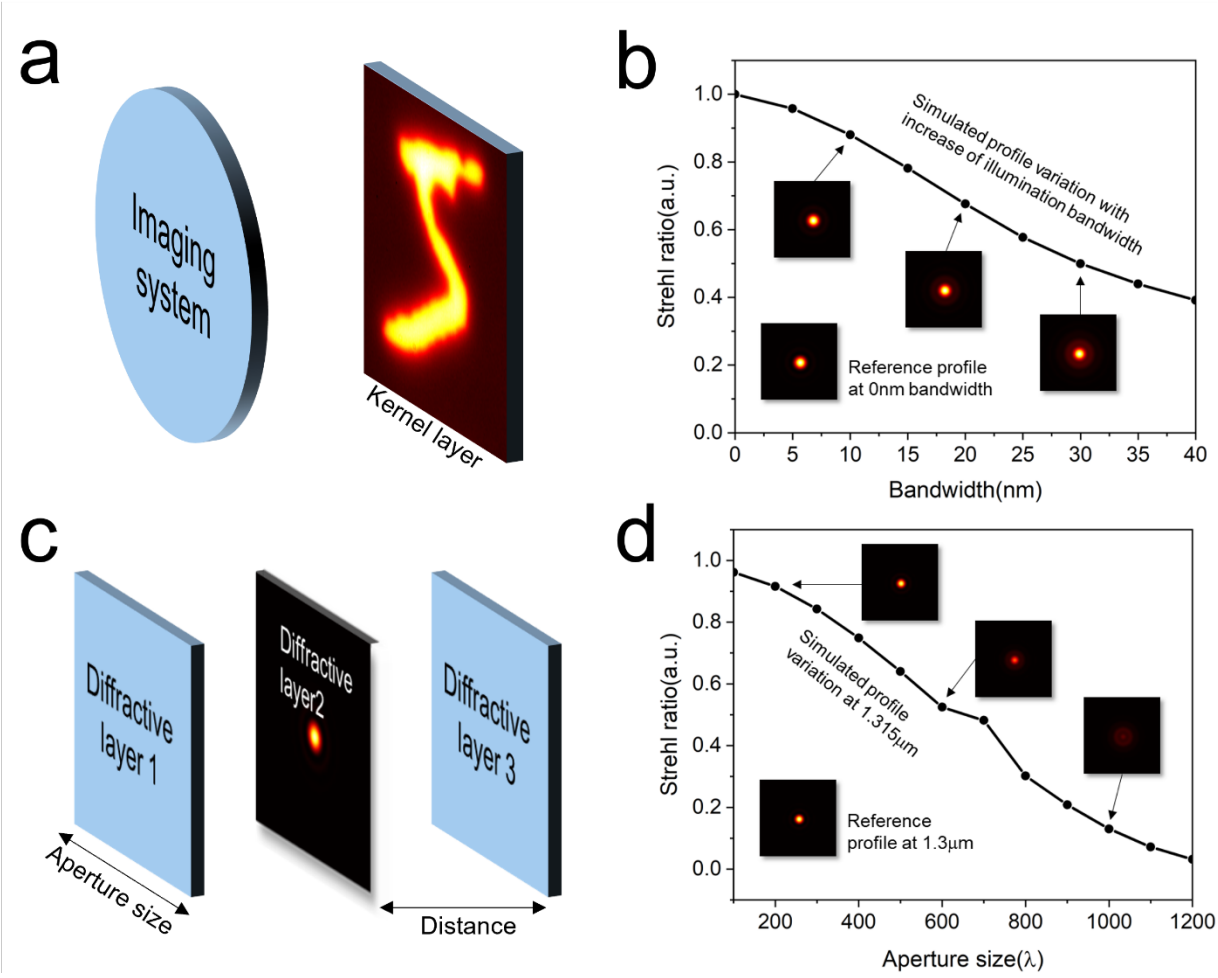

Figure 3.11 Bandwidth verification of meta-optic system and comparison to diffractive neural networks. (a) A schematic of hybrid neural network. (b) The Strehl of the imaging system in terms of the illumination bandwidth. Insets show point spread function (PSF) of the imaging system in terms of illumination bandwidth. (c) A schematic of a simple diffractive neural network. (d) The performance of diffractive layer as a function of input aperture size.

In the hybrid neural network system, I used a bandpass spectral filter in front of a tungsten lamp as the illumination source to verify that our system works under incoherent light illumination. The filter bandwidth was 30nm. The bandwidth of the system is limited by the multi-channel lens since the kernel layer is broadband, as shown in the thesis. The performance of the metalens based on the illumination bandwidth was calculated, as shown in Fig.3.11 (a). Here, the calculation is based on the angular spectrum propagation method, where the point spread function of a metalens was calculated under the illumination of various bandwidths, with each wavelength being equally weighted. It is worth mentioning that the diameter of our metalens is fixed at 2.4mm with an *f*/# of *f*/3 and moving to a smaller aperture or larger *f*/# would increase bandwidth. Fig.3.11 (b) presents the Strehl ratio of the lens for different illumination bandwidths, where a ratio of ~0.5 was achieved using the present configuration. Importantly, while the Strehl number is reduced with increased bandwidth, the end-to-end design method mitigates aberrations as they are taken into account in the training/design. Thus, it is likely possible to increase bandwidth further.

Besides, there are several advantages of a discrete kernel neural network as described below. First, a discrete kernel allows for memory-efficient system architecture. Ideally, the neural network will have as few trainable parameters as possible. However, if arbitrary kernels (formed by a diffractive layer) are used, the system needs to design the phase control at each neuron to form the diffractive layer, which will drastically increase the data volume as the aperture size increases. Secondly, discrete kernels are needed if the system is dynamically reconfigured. Even in the case of a diffractive network, pixelization will be needed, due to practical limits on control electronics, to dynamically control the pattern of the metasurface. Furthermore, as outlined in the manuscript, as the size of the metasurface pixels is reduced, their transmission will deviate from the local phase approximation also placing a limit on the practical size of reconfigurable

metasurface pixels.

Compared to a diffractive neural network, the advantage of our proposed method can also be described in the following aspects. First, the proposed system has alignment tolerance due to end-to-end optimization. I incorporate 10% noise fluctuation and $\pm 3°$ rotation error in the training process, which makes the system less sensitive to the image position. However, the multilayer diffractive structure has a high sensitivity to the interlayer alignment process. According to our previous research as well as recent publications from other groups, misalignment of even a single unit cell will lead to a large difference in the far-field intensity distribution, even for a simple 2-layer system, making it difficult to scale a high-quality diffractive neural network into the visible spectrum. Secondly, our proposed method can be employed with broadband illumination due to the end-to-end optimization process, while a diffractive neural network, especially for a large aperture, will only work under narrow band (laser) illumination. To quantitatively demonstrate this, I calculate the performance of a simple diffractive neural network under different illumination bandwidths, as shown in Fig.3.11 (c). In this architecture, the first layer will provide a specific neural weight, which will converge all the intensity into a spot, identical to a lens, hence we can use Strehl ratio to account for the performance. During the calculation, the *f*/# of the diffractive system was fixed as 2 for each layer and the system was designed at a wavelength of 1.3μm. Fig.3.11 (d) shows the performance of the corresponding system working at a wavelength (1.315um) with a 15nm deviation from the designed wavelength as a function of aperture size. With an increase in aperture size, the performance will deteriorate drastically, making a diffractive neural network unsuitable for broadband illumination at practical aperture sizes.

3.6 Further Optimization for Optical Frontend

The complex-amplitude control approach can also be applied to the optical convolution

process, which can further improve the complexity and robustness of the proposed hybrid neural network system. The complexity of the neural network, described using FLOPs, dictates the robustness and complexity of the classification task. The stride number is related to the system complexity, which in the approach described in section 3.2 is limited to the kernel size due to the spatial multiplexing method employed. Although robustness was optimized during the training process, the complexity of the system could be further enhanced by reducing the stride number of the optical convolution operations. This can be achieved using complex-valued amplitude manipulation in the kernel layer providing for control over image overlap and the ability to achieve arbitrary stride values.

The reduced stride number (stride number less than kernel size) requires entanglement of the neurons, necessitating complex-amplitude control in the kernel layer. In this case, the metasurface-based kernel layer should be separated from the photodetector plane by a certain distance, such that the modulated signal can have interaction. Fig.3.11 (a) shows an example of digital convolution, where a 4×3 pixel array forms a simple image being convoluted with a 3×3 kernel. The stride number was set as 1, resulting in a 6×5 output image. To achieve this operation optically, we designed a single channel kernel layer with the complex-amplitude field based on the following equation,

$$F[\alpha(x,y),\phi(x,y)] = \sum_i^9 \exp\left[i \cdot \frac{2\pi}{\lambda}\left(f - \sqrt{f^2 + (x-a_i)^2 + (y-b_i)^2}\right)\right] \cdot w_i \qquad (3.6)$$

Where w_i represents each value in the kernel matrix, a_i and b_i correspond to the displacement of each unique focal spot from the center of the lens which dictates the stride number in the convolution process. The designed complex-amplitude field is shown if Fig.3.11 (b). This manipulation process is similar to the multi-channel metalens discussed in section 3.4, however, by controlling the displacement of each focal spot and transmission of each independent channel

(the value of kernel pixel in this case), we can achieve optical convolution with stride number less than the kernel size. Optical measurement of this optical convolution process is exhibited in Fig.3.11 (c) including the measured input image, focal spot profile, and convolution results, showing an excellent match with the digital operation result. The significance of small stride number is also shown in Fig.3.11 (d). During the convolution process, with the same number of neurons, the complexity of the operations (FLOPs) is significantly increased when reducing the stride number, leading to a more robust neural network.

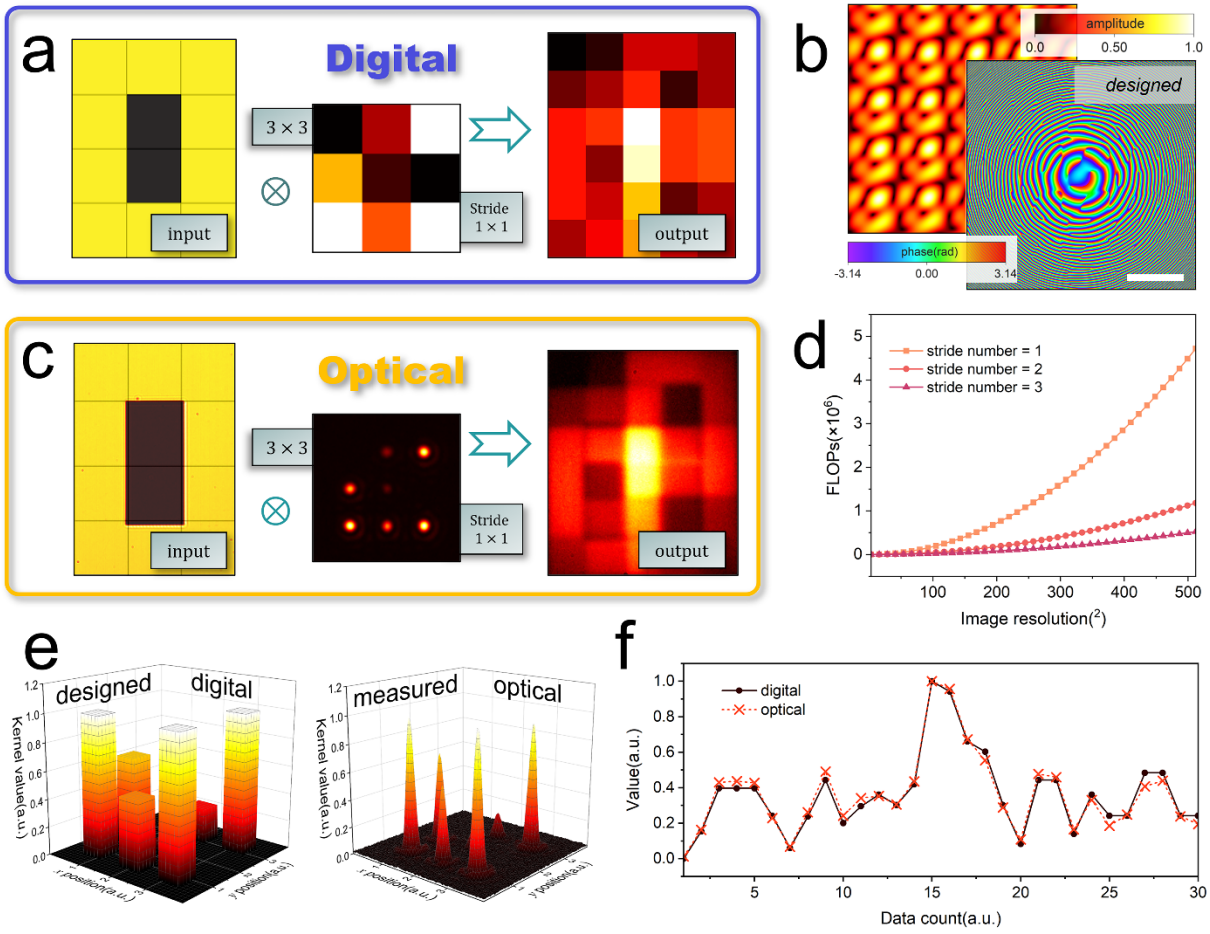

Figure 3.12 Complex-amplitude manipulation method for low stride number convolution. (a) The digital convolution process with a designed kernel. (b) The designed complex-amplitude profile to operate optical convolution. (c) The convolution process performed by optical operations. All data in (c) was optical measured based on fabricated devices. (d) The FLOPS of convolution as the function of stride number as well as the input image resolution.

3.7 Conclusion

In this chapter, I have demonstrated a meta-optic accelerator for multi-functional image classification. The technique is enabled by the unique design freedom afforded by metasurfaces, including the creation of multi-channel lenses to duplicate information and polarization-sensitive kernel layers, which allow for discrimination based on both the spatial intensity profile and the polarization state of the object. The use of polarization demonstrates how optical front-ends are able to access additional information channels normally lost in traditional imaging systems. Furthermore, by implementing end-to-end design, we improved the robustness of the system to common noise sources, ultimately yielding ~94% experimental classification accuracy, which closely matches the theoretical prediction.

The proposed meta-optic accelerators can be massively parallel and serve to bridge the gap between the natural object and digital neural network analysis. The approach can allow one to harness the strengths of both free-space and electronic or optical chip-based architectures. Moreover, the ability to operate with incoherent illumination enables machine-vision applications with passive ambient lighting which is incompatible with diffractive neural networks. End-to-end optimization also provides a robust platform that can balance the trade-off between bandwidth as well as the aperture size for a meta-optic system. Ultimately, these advantages allow meta-optic accelerators to achieve superior processing speed while also lowering power consumption and thus could lead to advances in a wide range of compact, low-power, and high-speed computer vision systems.

Chapter 4

Nanosphere Lithography based Large-scale Metasurfaces

4.1 Introduction

The flexibility of meta-optics in dictating the electromagnetic response has led to numerous metasurface-based optical elements such as beam deflectors[121, 122, 17], holograms[38, 39, 40], image processors[46, 123, 124], biosensors[125, 126] and metalenses[18, 31, 127]. The emergence of multi-element compound meta-optics offers even more flexibility in realizing complex optical assemblies[32, 75, 78]. However, the current conventional fabrication techniques are generally slow and result in optics that are difficult, or expensive, to manufacture at the scale of their refractive optic counterparts. Advances in affordable and scalable fabrication techniques are needed for wider-scale adoption of metasurfaces and associated optical systems.

Electron-beam lithography (EBL) is the most widely used fabrication technique for visible and near-infrared metasurfaces as their feature size is typically beyond the limitation of conventional ultra-violet (UV) contact mask photolithography systems[128]. While EBL provides extremely high patterning resolution, the serial exposure process limits throughput and ultimately relegates the applicability to prototype level devices. Stepper-based lithography, on the other hand, has been proven as one of the most powerful manufacturing platforms in the semiconductor industry. These systems, through the use of focusing optics, allow for both parallel exposure and subwavelength patterning resolution. Nevertheless, the complexity of the optical system in steppers, as well as the need for high-quality optical components, immersion optics, and highly accurate mechanical components, results in high system cost[129]. In addition, the millions, or even billions of unit cells comprising a metasurface, result in extremely large patterning files that require

algorithmic reduction based on structural symmetries[130, 15]. While this reduction will work with high symmetry structures such as metalenses, it will not suffice when there is little, if any, underlying symmetry such as in holograms.

Self-assembly methods, on the other hand, provide a promising direction for large-scale device fabrication. These methods depend on a material's peculiar chemical or physical properties during bottom-up growth, for instance, block copolymer[131], DNA nanostructure[132], and nanotubes[133] can be used to realize distinctive shapes that can be utilized directly as the desired structure or as templates for further fabrication. Among these techniques, it has been demonstrated that self-assembled nanospheres can serve as a means for high-resolution optical lithography[134, 135, 136, 137, 138, 137,] with each sphere serving as a lens. Under illumination from a UV light source, each nanosphere will generate a photonic jet which can be used to expose an underlying photoresist. This technique can provide stepper-level spatial resolution while taking advantage of the self-assembled hexagonal lattice to locate the unit cells.

In this chapter, I demonstrate the fabrication techniques for both periodic and non-periodic large-scale metasurface based on nanosphere self-assembly. For the former case, I will present the applications of compound large-scale metasurface systems for image processing such as edge detection, which can be applied to the integrated machine vision platform. The non-periodic large-scale metasurface fabrication technique, on the other hand, is also exhibited to indicate the flexibility of the proposed lithography method.

4.2 Nanosphere Self-assembly Method

In this section, we will introduce the technique of nanosphere self-assembly technique, which is fundamental to the large-scale metasurface fabrication technique in the following sections. To achieve the nanosphere self-assembly, the liquid-air interface self-assembly setup was used as

shown in Fig.4.1 (a), where the nanosphere solution was injected and self-assembled over the water surface[139, 140].

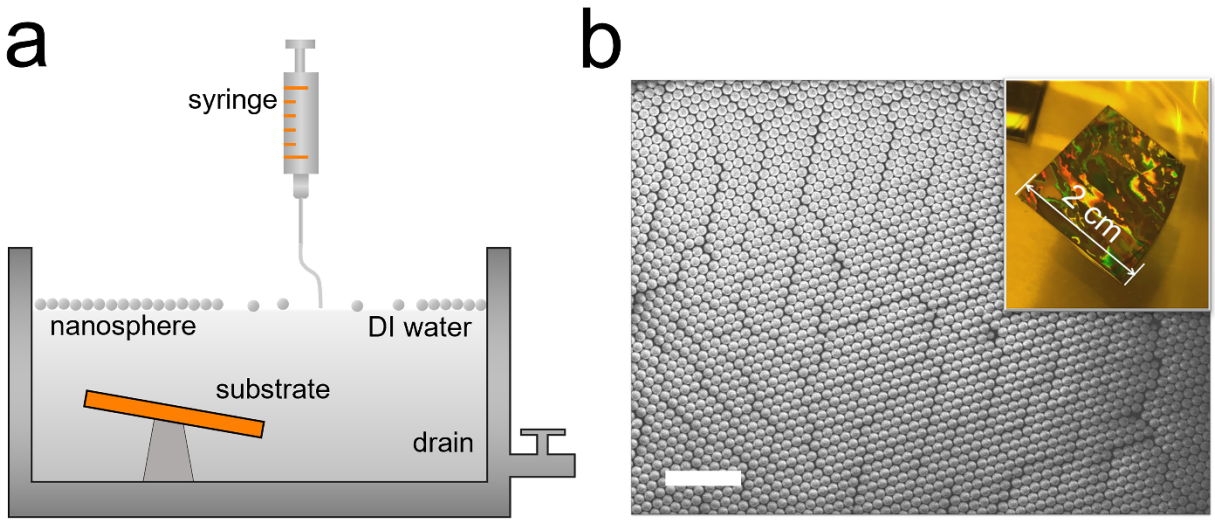

Figure 4.1 Schematics of nanosphere self-assembly process. (a) The liquid-air interface nanosphere self-assembly setup. (b) SEM image of self-assembled nanosphere array. Inset shows the optical image of the corresponding sample.

Firstly, the commercially available (EPRUI Biotech Co.) polystyrene nanosphere aqueous solution (10wt% and 3% CV) was mixed with an equal volume of methanol. Ten minutes of sonication was used to fully mix the solution before being injected onto the surface of the water using a syringe at a speed of 5μl/min. Then a Tygon tube with a diameter of 0.55mm was connected to the syringe needle, with the tube just touching the DI water surface, forming a meniscus onto which the nanospheres are deposited. Due to their hydrophobic surface, polystyrene nanospheres float on the surface of the water bath. Instead of using surfactant to accelerate the self-assembly process, which may cause nanospheres to fall from the surface, we used a flat gas nozzle to blow nitrogen onto the surface during self-assembly at a rate of 5L/min. The small perturbation on the water surface can help reorient the nanospheres into a large-scale hexagonal close-packaged monolayer[141]. The monolayer can fill most of the area of a 90mm diameter dish after around 15

minutes of self-assembly. The self-assembly process is finished by slowly draining the water to transfer the monolayer onto the substrate which has previously been placed in.

Due to size variation of the nanospheres, defects are unavoidable, leading to stress in the monolayer. In order to release the stress, during the transfer process the substrate was tilted by a 10° angle, which also helps to avoid formation of a multilayer structure[142]. Fig.4.1 (b) shows an SEM image of a transferred nanosphere monolayer and the inset corresponds to an optical image where the different colors correspond to domains with different crystal orientations. The size of the nanosphere lattices is ~2cm x 2cm in the samples presented in this paper. However, past demonstrations have shown scaling to sizes of 10cm x 10cm by using larger water baths, indicating the potential to fabricate wafer-scale devices.

4.3 Image Processing based on Large-scale Compound Meta-optic

Imaging processing is a critical and rapidly advancing technology for various science and engineering disciplines, with ever more complex digital tools opening the door to new avenues in biological imaging, three-dimensional reconstruction, and autonomous cars. Edge-based enhancement is particularly useful for data compression, object inspection, microscopy, and general computer vision. Edge-based enhancement is accomplished using spatial differentiation, which can be based on either electronic or optical architectures. Although digital circuits are able to perform complex data processing, there are limitations due to computation speed and power consumption. Optical analog computation, with the ability to process information directly using the optical signal, provides an alternative approach to performing large-scale and real-time data processing with minimal, if any, power consumption.

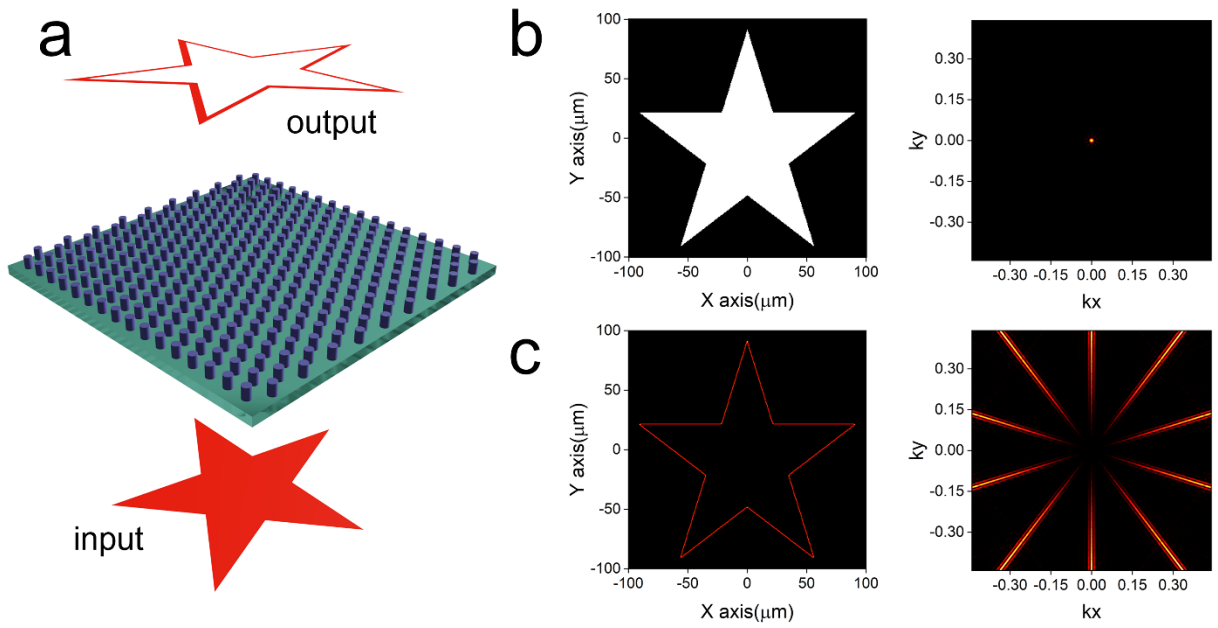

Figure 4.2 The diagram of edge detection based on non-local metasurface. (a) Edge detection process where metasurface serves as a k-space filter. (b) and (c) Image signal intensity distribution in real space (left) and k-space (right). (b) indicates a solid area signal from the pattern, while (c) exhibits the edge signal. The intensities have been normalized to respective maximums.

Traditionally, analog image differentiation has been performed using Fourier methods based on lenses and filter systems. However, the use of multiple conventional lenses, such as those found in 4*f* Fourier filtering, results in a large form factor that is not compatible with compact integrated systems. One option for significantly reducing the optical system size is to employ nanophotonic materials such as metasurfaces and photonic crystals for optical image processing. For example, it has been shown that multiple metasurfaces can be used to perform a range of mathematical operations, and there have been several theoretical proposals for image differentiation using single-layer nanophotonic materials. Furthermore, image differentiation has been experimentally demonstrated using photonic crystals, the spin Hall effect, surface plasmon-based devices, and the Pancharatnam-Berry phase. However, these past experimental approaches have been restricted to 1D and some require additional refractive elements (prisms or lenses) for either plasmon coupling or performing a Fourier transform, which negates the advantage of the

thin and flat elements.

In this section, I will introduce a metasurface-based method to perform the edge enhancement named differentiation over the pure optical signal as shown in Fig.4.2 (a). This differentiator consists of a α-Si nanopillar photonic crystal with an angular-dependent optical response, which can transmit the light with a high incident angle while blocking the low-k components. The proposed nanophotonic differentiator can be directly integrated into an optical microscope and onto a camera sensor, demonstrating the ease with which it can be vertically integrated into the existing imaging system. Such compact volume factor with cost-effective merit opens a new door for optical analog image processing in applications involving computer vision.

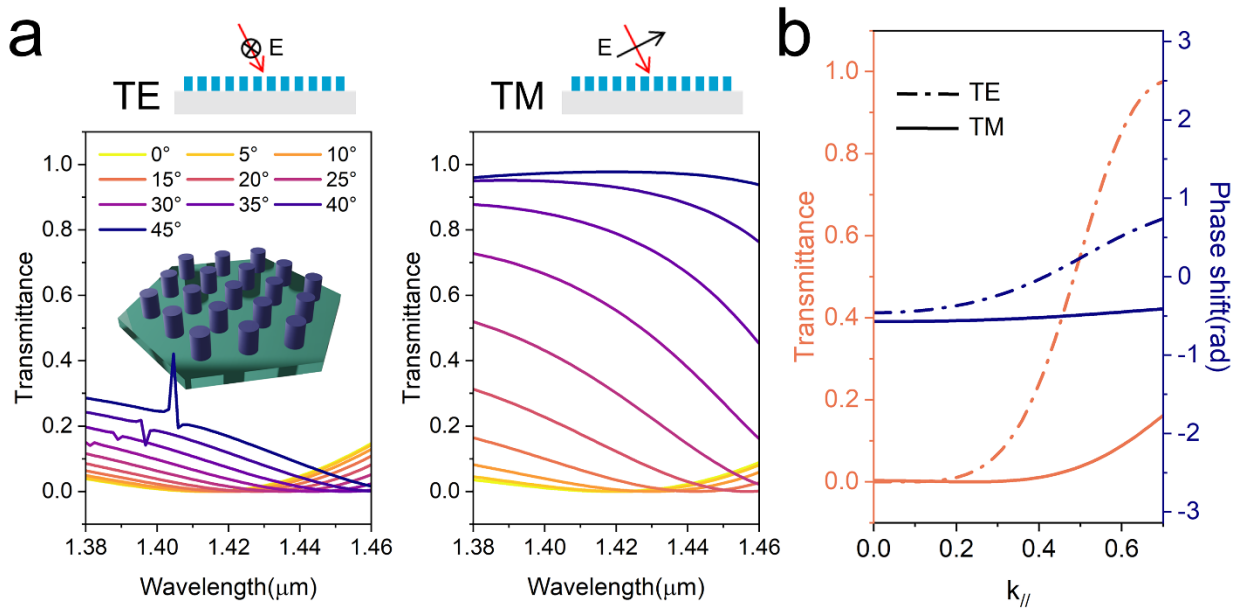

Figure 4.3 Simulated optical response of non-local metasurface. (a) and (b) The TE and TM modes based transmitted optical response of metasurface in terms of incident angle and wavelength. Inset shows the schematic of optical metasurface. (c) The transmittance and phase response of non-local metasurface as a function of incident angle. Dash line represents TE mode while solid line shows the TM mode response. For TM mode, the transmittance line indicates a high-k filter.

To perform the edge enhancement operations with nanophotonic, we need to understand the components of an image from the angular spectrum perspective (k space). Considering we

have an image with the amplitude distribution as a star and uniform phase profile, shown in Fig.4.2 (b) left, we can obtain the information distribution in k space by performing the Fourier transform over the spatial image. In this case, most of the signal comprising the solid area of the star focuses on the center of the k space map as shown in Fig.4.2 (b) right, indicating the light from the image with a low divergent angle forming the main solid area. However, if we extract the edge information of the original image with the same Fourier transformation operation, as exhibited in Fig.4.2 (c), the results indicate that the edge signal mainly comes from the light with a high divergent angle. It is worth noting that we only consider the original image with uniform phase distribution. Therefore, coherent illumination is required for the abovementioned optical image processing. In this case, a photonic structure that can only transmit the signal with high-k components is required for the edge enhancement operation.

To achieve the required angular-dependent optical response, we used a 2D photonic crystal composed of cylindrical Si nanopillars with a hexagonal lattice on a silicon dioxide substrate as shown in Fig.4.3 (a). The nanopillars have a height of 480nm, diameter of 340nm, and period of 740nm. Fig.4.3 (a) and (b) also exhibit the simulation transmission coefficient amplitude $|t(\lambda, \theta)|$ as a function of the wavelength, λ, as well as the incident angle, θ_{air}, along the $\Gamma - \mathrm{X}$ direction ($\varphi = 0^{\circ}$, where φ is the azimuthal angle in the horizontal plane) for TE and TM indecent state. It is worth noting that no polarization conversions occur for the transmitted light. At the normal incident, the transmission coefficient amplitude remains low for both TE and TM modes. However, with oblique incidence, the TM light starts to transmit the photonic crystal while the TE mode light stays blocked. This is because the dipole resonant frequency under TE mode remains unchanged as a function of incident angle, exhibiting angular-independent optical response. This resonance results in no transmitted light for TE mode input due to the impedance mismatch over the photonic

crystal surface. However, under TM mode illumination, with increase of the incident angle, the resonance mode begins to couple to free space, becoming quasi-guided with a finite lifetime, resulting in a rapid change in transmittance. Such angular-dependent properties offer the possibility to perform isotropic (2D) image edge enhancement with optic-only operations by a nanophotonic device.

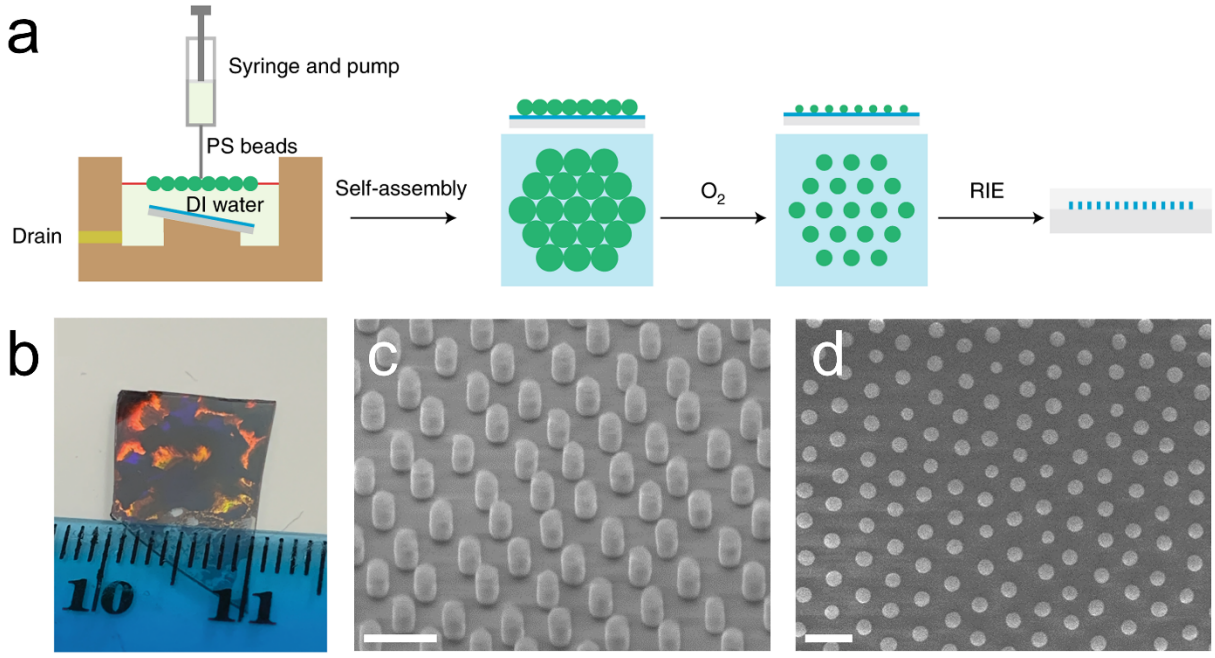

Figure 4.4 Fabrication of large-scale non-local metasurface. (a) The fabrication process based on nanosphere self-assembly technique. (b) The optical image of self-assembled nanosphere array. The diffracted color indicates various polycrystalline domains in the sample. (c) and (d) The SEM of fabricated non-local metasurface under tilted (c) and top-down (d) perspective. Scale bar: 1μm.

A large-scale photonic crystal based on nanosphere lithography technique was fabricated as shown in Fig.4.4, forming a polystyrene nanosphere array embedded in a hexagonal lattice over a silicon-on-silica substrate. The diameter of nanosphere was chosen as 740nm to match the period of the design. The polystyrene array was then treated with oxygen plasma to downscale the diameter and used as the etch mask during RIE to define the Si pillars. Fig.4.4 (b) presents an optical image of fabricated ~1cm×1cm image differentiator. The color variation corresponds to

different orientation domains, which does not affect the transmission at different incident angles. The SEM images in Fig.4.4 (c) and (d) show high-quality Si resonators and a well-defined hexagonal lattice over a large area. Such large-scale devices can be applied to traditional optical systems by integration into a camera sensor.

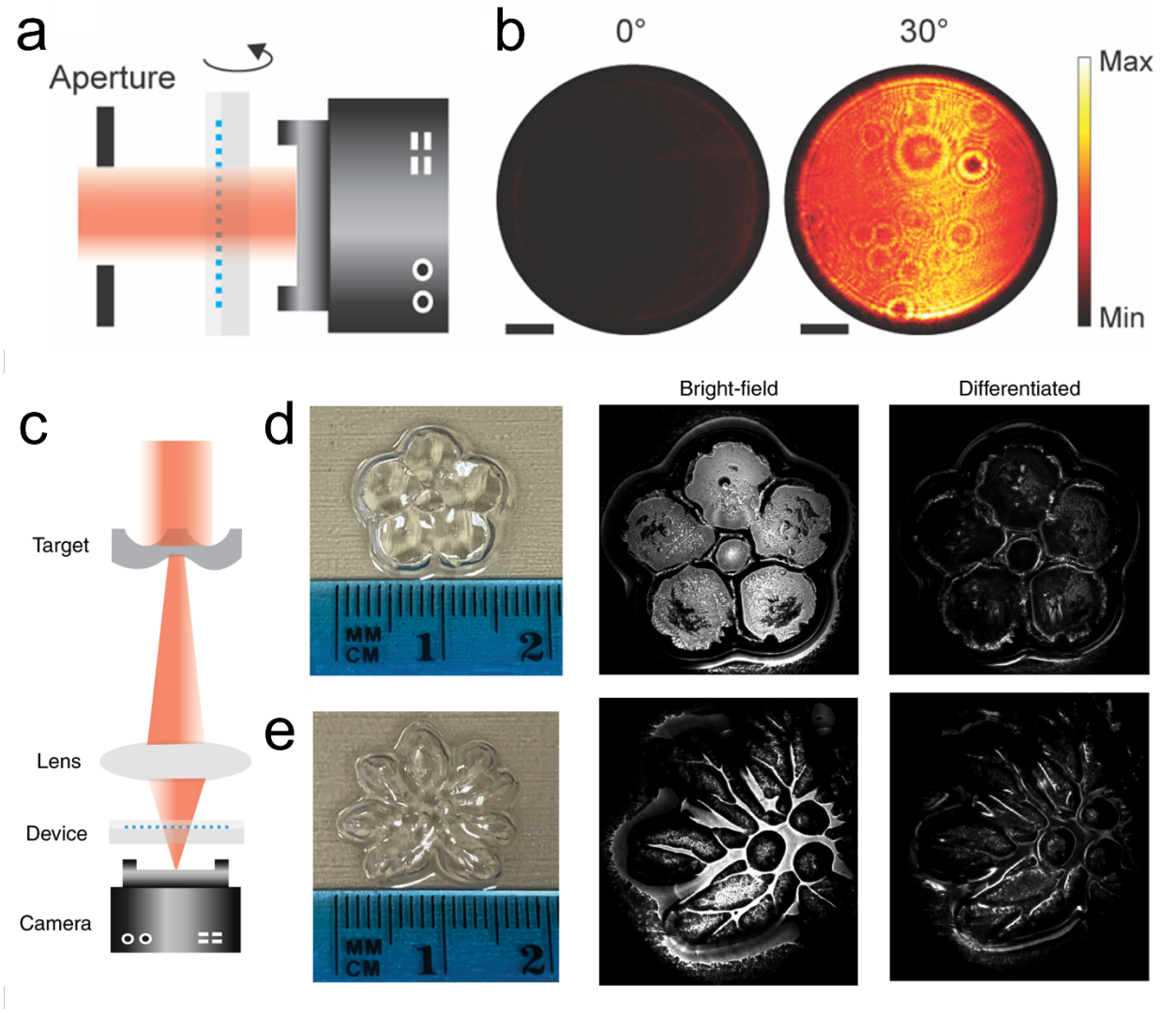

Figure 4.5 Large-scale image differentiator using nanosphere lithography. (a) Schematic of the transmission measurement setup for large-scale metasurface. The large-scale differentiator was placed directly in front of the camera for the measurements. (b) The captured intensity map when the filter is at normal and 30° incidence angle. Scale bar: 1μm. (c) Schematic of the imaging set-up for differentiation. The large-scale device is placed in front of a near-infrared (NIR) camera sensor. (d) Optical image of a plastic flower mould (left), which was used as a 3D macroscopic imaging target. The Bright-field (middle) and differentiated results (right) for the same target was captured without/with metasurface differentiator, respectively. (e) The same imaging results as in (d) on a second target.

The differentiator was characterized by the angular response measurement, where the device was mounted in front of a camera sensor as shown in Fig.4.5 (a). A randomly polarized laser at the wavelength of 1450nm was used as the input signal. The differentiator presents a high-k filter property since a dark and bright field was observed under normal and oblique incident light, respectively, as shown in Fig.4.5 (b). In order to mimic a configuration for computer vision applications, the large-scale spatial differentiator was placed directly in front of a NIR camera detector after the imaging lens, as shown in Fig.4.5 (c). For imaging targets, transparent centimeter-sized plastic flower moulds were used (Fig.4.5 (d) and (e)) due to their curved surfaces, which scatter light at large angles. Fig.4.5 (d) and (e) show the imaging results with and without the differentiator for two separate objects. Compared to the bright-field images, the edges of the flowers are revealed when applying the differentiator. Although we have not placed the differentiator directly on the sensor in this case, there is nothing that would prevent this level of integration in creating a monolithic edge-detecting sensor for computer vision applications.

4.4 Non-periodic Large-scale Metasurface Manufacture and Applications

Previous demonstrations of nanosphere lithography have demonstrated periodic structures such as perfect reflectors[143], absorbers[144, 145, 146], and photonic crystals[147, 148]. Adjusting the substrate surface tomography allows for aperiodic structures to be realized but only in relation to the position of the unit cells while the resonators remain the same[149]. To date, there has been no demonstration of a technique that is capable of fabricating metasurfaces with non-periodic phase profiles, such as those needed for lenses or holograms, using cost-effective self-assembly-based techniques.

Here, I will demonstrate a novel manufacturing technique based on grayscale nanosphere lithography that allows for metasurfaces with arbitrary, non-periodic phase profiles to be fabricated

in a cost-effective and scalable manner. To achieve non-periodic phase control, we combine nanosphere lithography with illumination from a spatial light modulator[150, 151, 152] that allows for the dose, and thus exposure size, to be spatially controlled as shown in Fig.4.6. Furthermore, in the method, the resonator size was encoded into an 8-bit grayscale pattern rather than defining the geometric parameters of each individual resonator. This significantly reduces the geometric data required to write a structure leading to dramatically reduced pattern file sizes, enabling structures without an underlying symmetry. As a testbed for the technique, we fabricated a series of large-scale (diameter of 1mm) metalenses working at a wavelength of 1.7μm, demonstrating diffraction-limited focusing and above 83% relative efficiency. I also illustrate how this technique can be used for realizing non-symmetric large-scale metasurface holograms within minimal mask sizes.

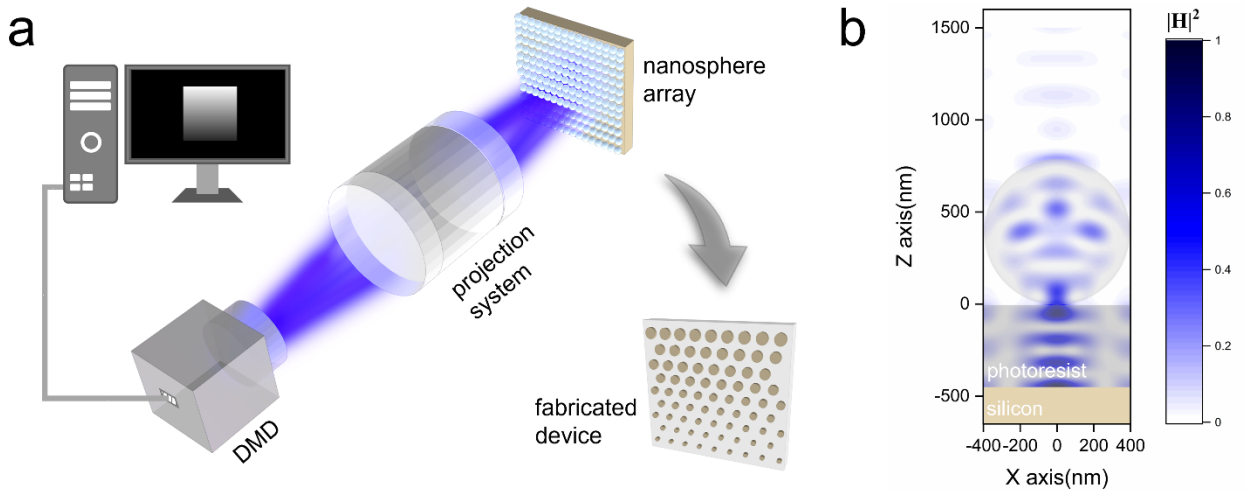

Figure 4.6 Self-assembly assisted large-scale metasurface fabrication platform. (a) A grayscale pattern is generated by the DMD system using a 365nm I-line UV light source which is transmitted by a projection system comprising an objective lens. The system illuminates nanospheres that have been self-assembled on the substrate and serve to focus the light. The grayscale intensity level is used for intensity manipulation over the substrate surface to accurately control the effective exposed area under each nanosphere. The exposed results are nonperiodic according to the exposure dosage control from grayscale pattern. (b) The photonic jet phenomenon, within a polystyrene nanosphere and exposure of the photoresist below. The diameter of nanosphere is 800nm in this simulation.

The fabrication approach presented here utilizes nanosphere lithography to form etch

masks for patterning silicon nanopillar unit cells. The processes start with generating a monolayer of self-assembled polystyrene nanospheres. The self-assembly process has been described in section 4.1, where the liquid-air interface self-assembly method was utilized. The wafer on which the metasurface will be fabricated, and onto which the spheres will be transferred, is placed within the water bath at the start of the process. The wafers comprise a quartz handle, a silicon device layer grown via low-pressure chemical vapor deposition (LPCVD), and a spin-coated photoresist layer. Transfer of the self-assembled nanosphere lattice is accomplished by slowly draining the water bath. Although the diffracted color indicates various polycrystalline domains in the nanosphere monolayer, in past work, it has been demonstrated, in the case of weakly coupled unit cells, the polycrystalline domain structure does not significantly affect metasurface performance.

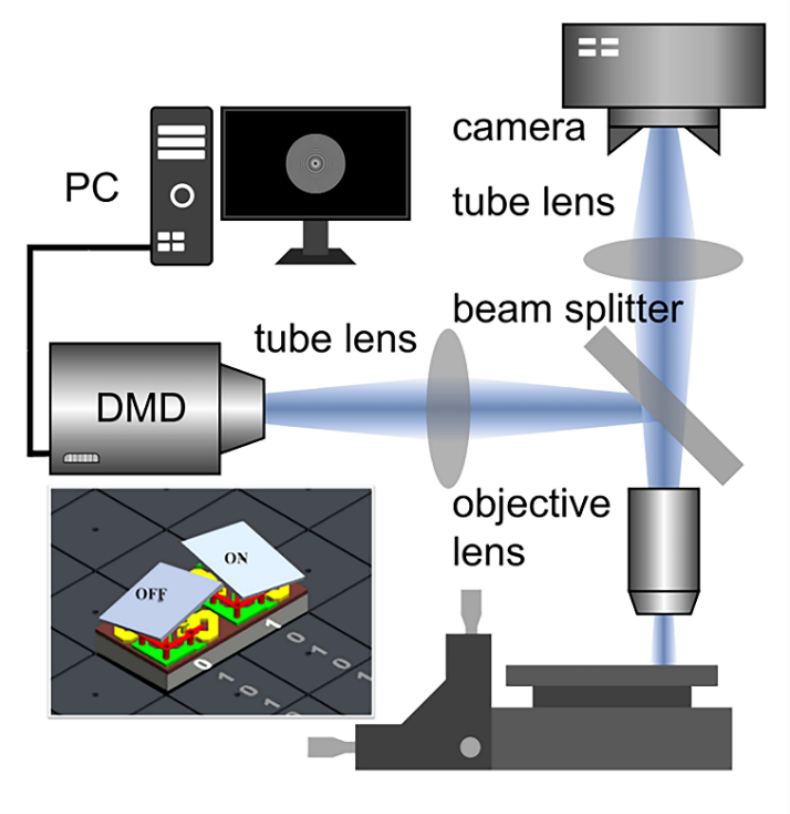

Figure 4.7 Schematic of grayscale lithography setup based on intensity control using a DMD

Once the nanosphere array is transferred, it then serves as a lens array for exposing the photoresist beneath. The focal spot from the nanosphere was used as the exposure pattern resulting in a circular exposure profile, but past work has demonstrated the use of patterned masks for realizing more complicated geometries[149]. Importantly, the size of the area exposed is dictated by the illumination dosage, which is a function of exposure intensity and time. To control the exposure area, and thus resonator size, I utilize a digital micro-mirror device (DMD) as a spatial light modulator. The effective exposure intensity is controlled via the duty cycle of the micro-mirrors, which yields 8-bit depth and 1.6μm spatial resolution. The spatial resolution dictates the resolution at which the grayscale pattern can be modulated, which is four nanospheres in the current system. A higher resolution could be achieved by either using either a DMD with more pixels or reducing the illumination area using higher numerical aperture (NA) projection optics. Appendix D.1 shows the detailed fabrication procedure for the nanosphere lithography platform.

The detailed schematic of the grayscale lithography system based on a digital micromirror device (DLP6500, Texas Instruments Inc.) is exhibited in Fig.4.7. The source lamp wavelength is fixed at 365nm, and the intensity can be controlled with 8-bit depth based on a grayscale pattern generated from a computer. The image will pass through a tube lens (TTL200, Thorlabs) and be deflected by a beam splitter (BSW21, Thorlabs). With a 5X demagnification by an objective lens (MY5X-822, Thorlabs), the grayscale pattern is illuminated over the nanosphere surface. In order to ensure the exposed pattern can be focused on the surface plane, the exposure is monitored by a charged-coupled-device (CCD) camera (DCU223M, Thorlabs) combined with a tube lens (AC254-100-C-ML Thorlabs). A calibration of the imaging system is applied to make sure the image plane from DMD is placed at the sample plane.

The dose-to-exposure size calibration curve, dictating the grayscale pattern for device

fabrication, on the other hand, was generated by depositing Al_2O_3 into the exposed photoresist patterns and measuring the diameter as a function of the grayscale level (0 to 255). The calibration curve, presented in Fig.4.8 (a), was fitted by a quadratic polynomial curve and the mean square deviation of the diameter, which was found to be below 5%, is included as the error bars.

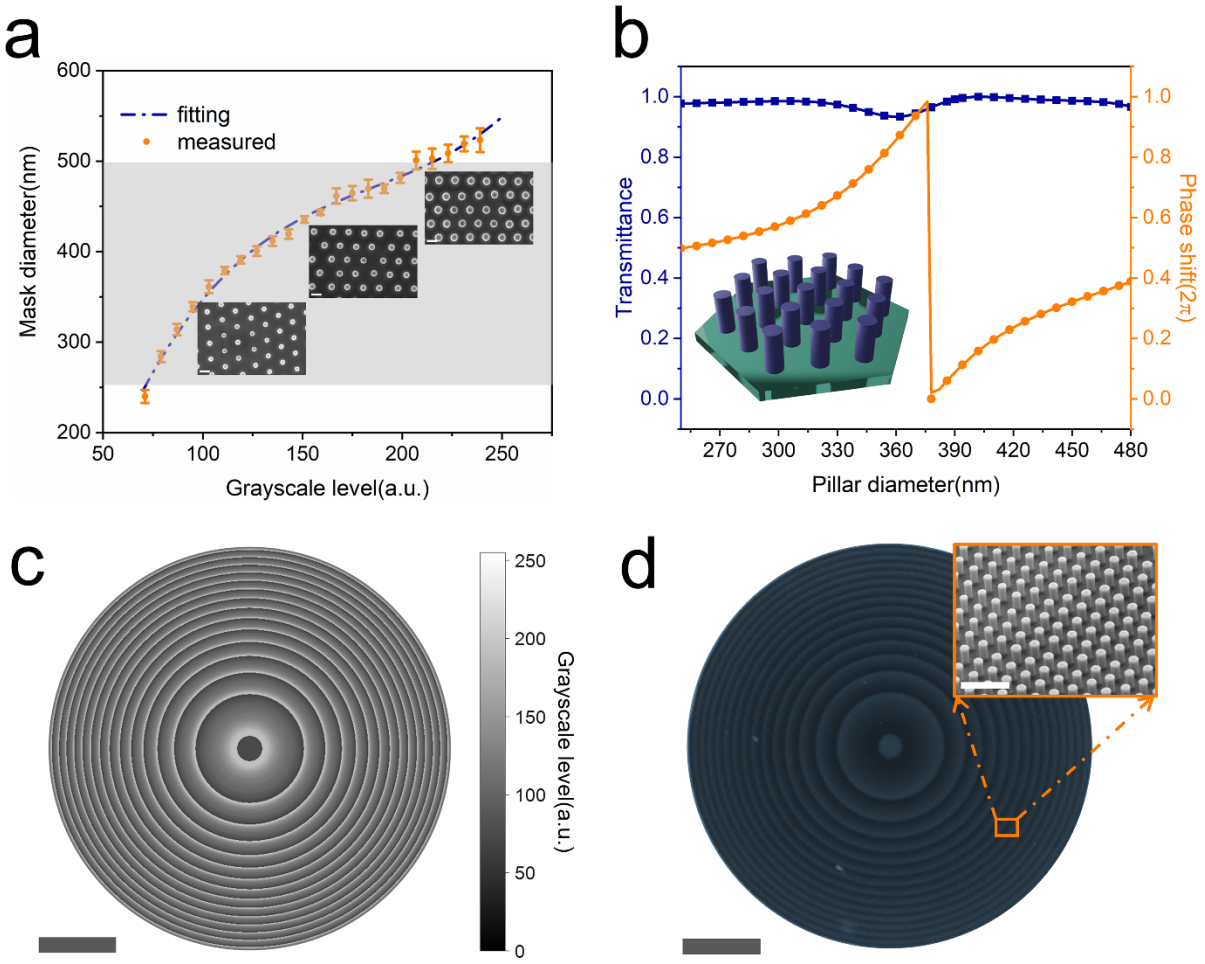

Figure 4.8 Fabrication results for large-scale metalenses based on grayscale lithography. (a) The relationship between the exposure dose, represented by grayscale level of the pattern, and the diameter of the Al_2O_3 hard mask after the lift-off process. Insets are SEM images of the hard mask with different exposure doses. Scale bar: 500nm. (b) The variation of transmission and phase shift with the diameter of the silicon nanopillars. The inset depicts the simulated unit cell arranged in a hexagonal lattice. (c) The grayscale pattern corresponds to the *f*/5 metalens. Scale bar: 200μm. (d) Optical image of the fabricated *f*/5 metalens. Scale bar: 200μm. Inset is a tilted SEM image showing the silicon nanopillars. Scale bar: 2.5μm.

As a testbed for the accuracy of this fabrication method, we first focus on the realization

of metasurface-based lenses as their performance can be quantitatively benchmarked against theoretical performance. The metalenses were designed with a hyperbolic phase profile, given by,

$$\phi(x,y) = k \times \left(f - \sqrt{x^2 + y^2 + f^2}\right) \tag{4.1}$$

where ϕ is the phase shift at a particular position, k is the wavenumber, and f is the focal length of designed metalens. This phase profile is converted into the grayscale pattern $G(x,y)$, where $G(x,y) = fit^{-1}\{D_\phi[\phi(x,y)]\}$ is the grayscale level, fit^{-1} is the inverse function of the fitted curve in Fig.4.8 (a) and D_ϕ is the diameter of the nano-post corresponding to the required phase. D_ϕ is acquired from extracting the phase delay from full-wave simulations of hexagonal lattices of silicon nano-posts as a function of diameter, as presented in Fig.4.8 (b). The shaded area in Fig.4.8 (a) illustrates the required diameter range for achieving a 2π phase shift, based on the full-wave simulations, indicating that it is well within the grayscale patterning range. From Fig.4.8 (a) and Fig.4.8 (b), we can generate the required grayscale exposure pattern, $G(x,y)$, which is shown in Fig.4.8 (c) for an *f*/5 metalens with a diameter of 1mm. This pattern was used for exposure of the S1805 photoresist below the self-assembled nanosphere array. The detailed fabrication process can be found in the Appendix. An optical image of the fabricated metalens is shown in Fig.4.8 (d) and an SEM image is in the inset.

In order to characterize the performance of fabricated metasurfaces, I customized an optical measurement setup with details shown in Appendix D.2. The optical measurement results for each metasurface device are exhibited in Fig.4.9 to indicate the fabrication quality. To evaluate the performance of each metalens, the theoretical focal spot profile was calculated based on a hyperbolic phase profile, generating diffraction-limited focal spots with full-width half maxima (FWHM) of 9.06μm and 5.66μm for *f*/5 and *f*/3 lenses, respectively (Fig.4.9 (a)). The measured

spot profiles closely match these theoretical curves, demonstrating diffraction-limited focusing. The focal spot profile along the axial axis was also recorded, which was found to closely match the theoretical performance with the results presented in Fig.4.9 (b) and (c). These measurements demonstrate that the designed hyperbolic phase profile has been accurately realized across the metalens.

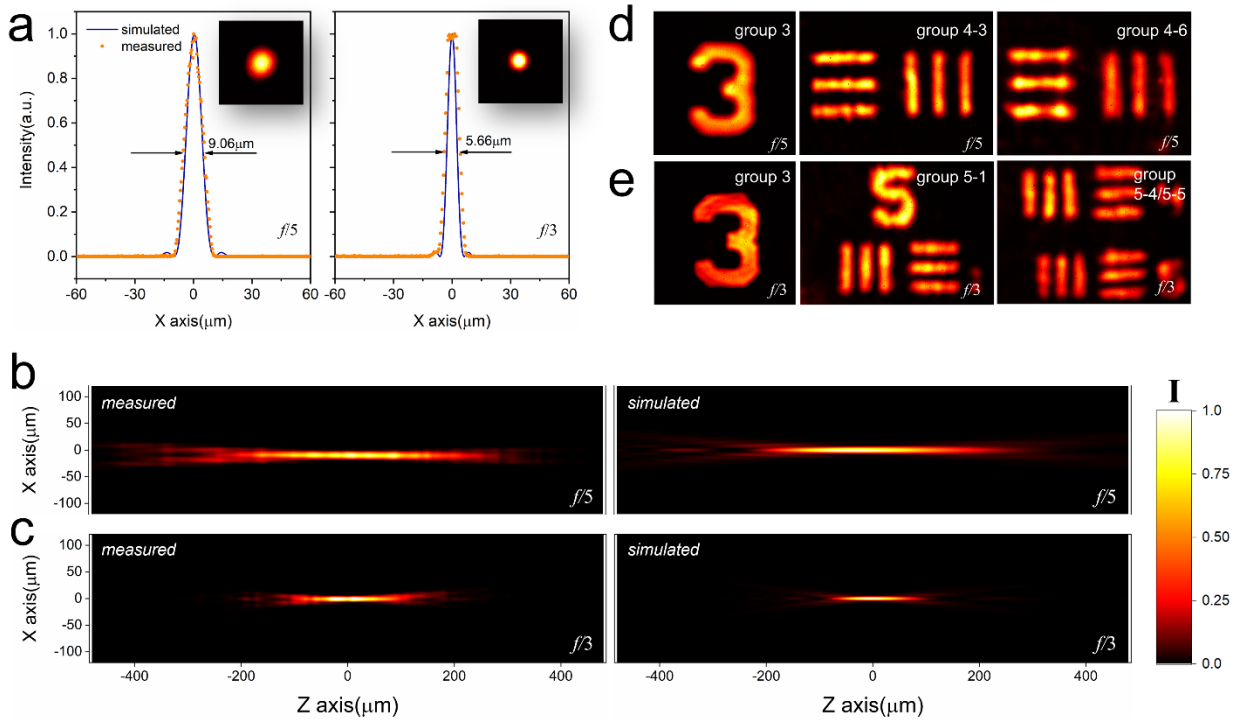

Figure 4.9 Experimental characterization of fabricated metalenses. (a) The measured and calculated focal spot profiles of fabricated metalenses with *f*/5(left) and *f*/3(right). Insets show the corresponding focal spot intensity distribution recorded by a NIR camera. (b) The measured (left) and experimental (right) focal spot profile along for optical axis for a metalens with *f*/5. (c) The measured (left) and simulated (right) focal spot profile along for optical axis for a metalens with *f*/3. (d) The imaging results of the USAF1951 standard test sample for the *f*/5 metalens (e) The imaging results of the USAF1951 standard test sample for the *f*/3 metalens.

The phase profile accuracy can be further verified by the imaging performance, which was characterized by imaging the standard 1951 United State Air Force (USAF) test chart (Thorlabs Inc.). The image from the metalens, recorded in combination with a tube lens, is shown in Fig.4.9 (d) and (e) and demonstrates minimal distortion. The increase in the numerical aperture of the *f*/3

lens results in an improvement in the image quality and resolution, with the ability to resolve group 4, element 6 (line width of 17.54μm), to group 5, element 5 (line width of 9.84μm). These results indicate the capability to fabricate large-scale metalenses in a single exposure shot. In this approach, the smallest *f*/# metalens that can be fabricated can be controlled via the magnification of the projection lens in combination with the DMD resolution.

The efficiency of the metalenses is the product of two factors, the relative focusing efficiency, defined as the intensity within the focal spot over all light passing through the metalens, and the transmission efficiency of the metalens. The fabricated metalenses were found to have relative focusing efficiencies of 88% and 83% for metalenses with *f*/5 and *f*/3, respectively, with a theoretical efficiency as high as 96% for the *f*/5 metalens. The drop in experimentally relative efficiency is ultimately induced by the presence of defects during self-assembly.

4.5 Robustness Analysis of Nanosphere Lithography

In the case of nanosphere self-assembly, defects arise due to the size variation of polystyrene nanospheres as well as incomplete self-assembly when the lattices are being formed, resulting in point defects and dislocations. To evaluate the drop in efficiency induced by these defects, we added a 5% random phase shift to each pixel to represent the standard deviation in the size of the nanospheres. Second, to represent point defects, 5% of the pixels, stochastically distributed, had their phase delay set to represent air. These defect levels result in relative focusing efficiencies that were found to best match the experimental efficiencies, as described in the next section. The images of the simulated and fabricated phase profiles are shown in Fig.4.10 (a) and (b), respectively, for comparison. The fabricated lenses have a lower point defect density with 2% of the spheres missing but also contain dislocations that have not been included in the simulated lenses.

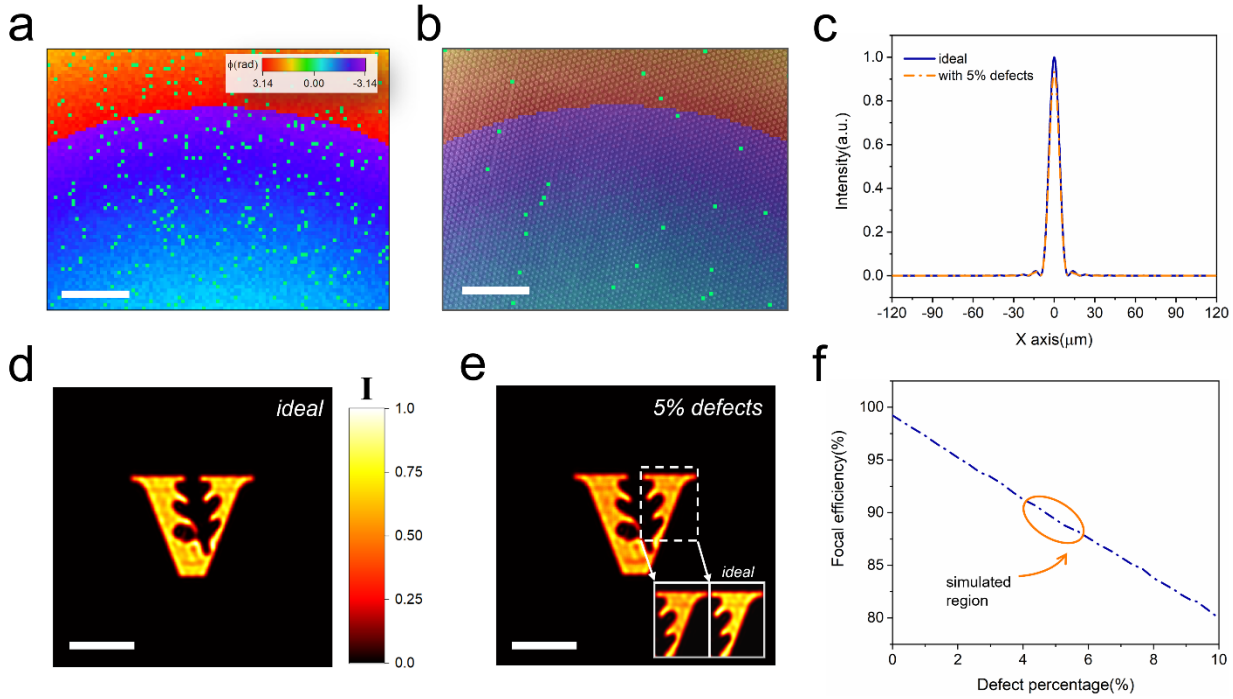

Figure 4.10 Roles of defects in metalens performance. (a) Phase shift profile of the designed metalens with a 5% defect density. Scale bar: 15μm. (b) SEM image of fabricated large-scale metalens. The imaged area is chosen to be close to (a) for comparison. Scale bar: 15μm. (c) The simulated focal spot profile of an ideal metalens (solid line) and one with 5% defect density (dash line), both are *f*/5. (d) Simulated imaging performance of ideal metalens with *f*/5. Scale bar: 250μm. (e) Simulated imaging performance of a metalens with the same parameters as (d) but with 5% defect density as well as a 5% phase variation. Inset: comparison of the magnified region from (d) and (e). Scale bar: 250μm. (f) The simulated focusing efficiency of a metalens with *f*/5 in terms of defect density. All lenses have a working wavelength of 1.7μm. Circles indicate the defects' density level in simulations.

The theoretical focal spot intensity profiles were calculated according to the Fresnel diffraction equation with the ideal phase profile taken as a reference. By adding a 5% defect density, as well the 5% phase shift noise into the ideal metalens phase profile, one can observe a drop of focusing efficiency to around 90% with minimal effect on the FWHM of the focal spot as shown in Fig.4.10 (c). The penalty in focusing efficiency is due to a transmission drop corresponding to light scattering from the defects. This scattering reduces the intensity of the image, as can be observed from the simulated images in Fig.4.10 (d) and (e). At the present defect density, the metalens has the same resolving power with a small decline in the signal-to-noise ratio. The global relationship between focal efficiency and defect density was calculated and exhibited in Fig. 4.10

(f). The focal efficiency can remain over 80% with a defect density of up to 10%. In the actual device, the point defect density is 2% which should result in a relative focusing efficiency of 95%. The difference between the measured (88%) and theoretical expectations most likely results from two factors. The first factor is the additional defects due to dislocations in the nanosphere lattice. The second factor is that the finite aperture of the projection system will blur the pattern profile, especially for the sharp intensity variation from the input pattern, which introduces a small phase aberration across the phase zone boundaries.

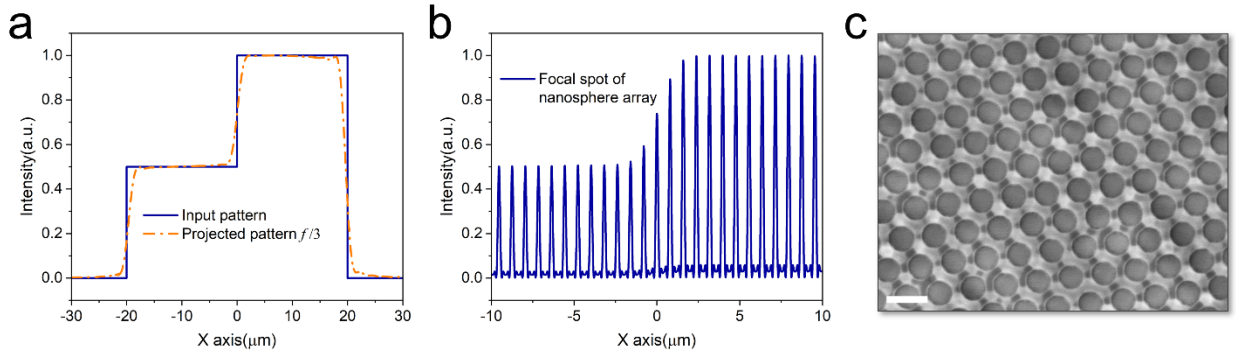

Figure 4.11 Projected pattern from a projection system with *f*/3. (a) The intensity profile of the intended pattern and the pattern projected onto the nanospheres. (b) The focal spot profile after the nanosphere array based on the projected pattern. The *f*/# and period of each nanosphere are set as 0.5 and 800nm. (c) SEM image of the developed photoresist. The photoresist was exposed to a large dose to reveal the diffracted pattern between nanospheres.

To demonstrate the effects of a sharp intensity variation in the projected pattern, I chose a step profile as the input pattern and calculated the steps in the projection process as shown in Fig.4.11 (a). We set the *f*/# of the projection system as *f*/3. Due to the finite aperture of the projection lens, the boundary of the step profile is blurred due to loss of some high spatial frequency information. Based on this imaging process, we also calculated the focal spot profile behind the nanosphere array with a blurred incident pattern from the projection system. Fig.4.11 (b) shows the profile from the nanosphere array that is projected onto the photoresist. Due to the blurring effects, the intensity of nanosphere focal spot will vary continuously over the step

resulting in a smooth transition of the meta-atom diameter between different phase zones. This variation will introduce a small aberration to the phase profile across the phase zone boundaries compared to the theoretical design, leading to a slight drop in efficiency. The aberration will be more pronounced for high numerical aperture metalenses with more zones. However, this is a relatively small aberration for our devices, evidenced by the fact that the *f/5* lens retains 88% relative efficiency.

There are also diffracted waves introduced by the periodic arrangement of nanospheres. This results in sidelobes adjacent to the main focal spot from each nanosphere. However, the intensity ratio of the main spot and the side lobe is more than 10, and thus these side lobes will not drastically affect the exposure due to the nonlinear reaction of photoresist to the dosage (an intensity threshold must be exceeded for exposure). This effect can be observed in Fig.4.11 (c) for the highest dosage employed in patterning, where dark spots appear between each primary exposure. The secondary exposure from the diffracted light is not sufficient to completely remove the photoresist during the development, thus there is no influence on the device morphology.

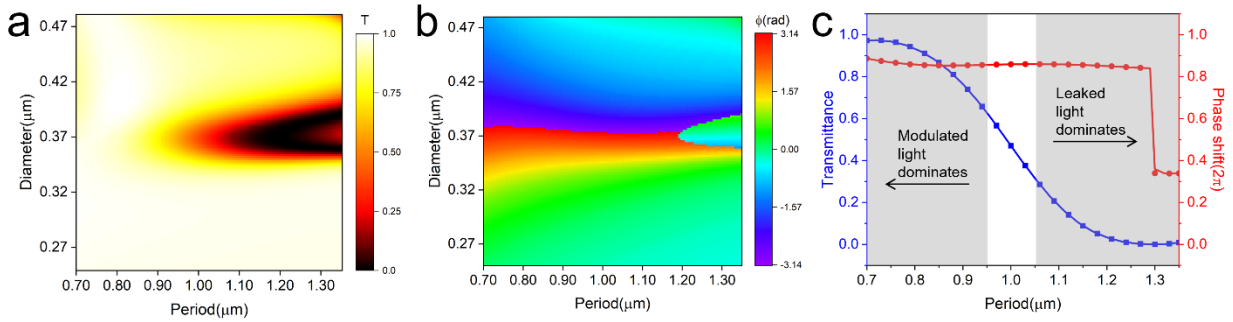

Figure 4.12 Zero-order complex transmission coefficient for unit cells with different periods and diameters. (a) The transmission as a function of period and diameter. The height of the pillars is fixed at 850nm. (b) The phase delay as a function of period and diameter. Periodic boundary conditions were used in the simulation. (c) The complex-transmission coefficient of unit-cells with fixed nanopillar diameter at 360nm as a function of lattice period.

The measured transmission efficiency was found to be 75% for both metalenses which can

be compared with a theoretical value of 97%. The drop in the experimental transmittance is due to variations in the local period during the self-assembly process. Especially at a larger period, there is a transmission dip for certain rod diameters that will reduce efficiency. Fig.4.12 demonstrates the complex transmission coefficient of meta-atoms in terms of the period. Each meta-atom was arranged in a hexagonal lattice in these simulations. The low-transmission area that occurs when the period is increased to around 1μm is due to the destructive interference between the scattered light, manipulated by silicon pillars, and leaked light that is directly transmitted through the array, not interacting with the pillars. At small periods, most of the incident light is concentrated in silicon pillars. However, as the period is increased (decreasing pillar density), the directly transmitted light leads to an interference effect with the light at is concentrated within the pillars. When the phase difference between the directly transmitted light and the light interacting with the pillars is close to π then destructive interference occurs, resulting in a low transmission area in Fig.4.12 (a). Note that the interference only occurs when the unit-cell diameter is close to 360nm as this corresponds to a π phase delay, as shown in Fig.4.12 (b). In the actual metasurface fabrication, the leaked light should be impressed since high-efficiency light manipulation is preferred for device. This issue can be solved with the assistance of additional surfactants during the self-assembly process[153, 154] or use of the Langmuir-Blodgett (LB) effect to obtain a more uniform nanosphere array[155, 156].

One technical issue associated with large-scale metasurfaces is the large amount of geometrical data needed for lithography masks. While data size reduction can be realized when patterning structures with underlying symmetry, such as metalenses, there is no general technique for metasurfaces lacking such symmetry. In order to demonstrate the flexibility of our proposed method for arbitrary large-scale meta-optics fabrication, a Fresnel hologram was designed with the

phase profile shown in Fig.4.13 (a).

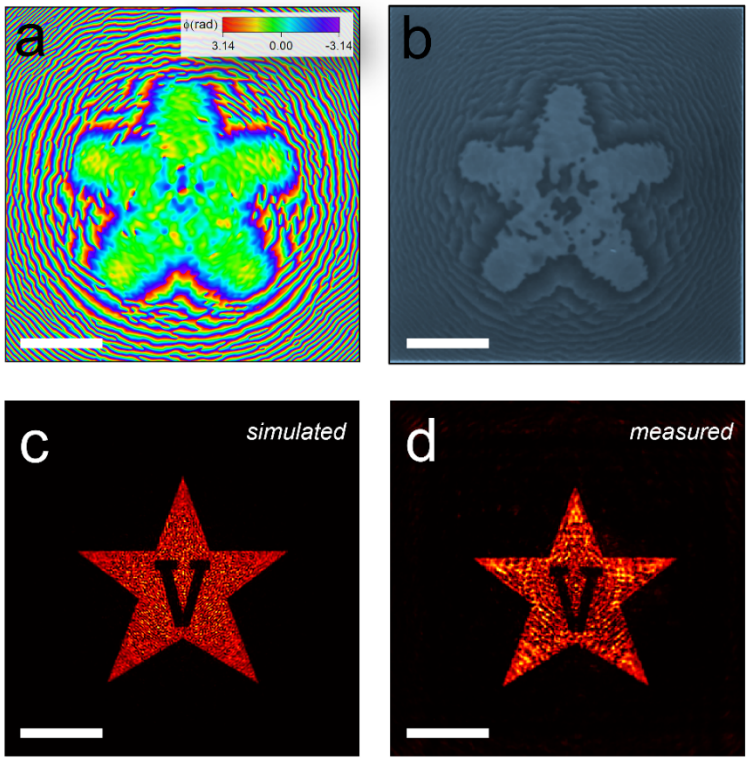

Figure 4.13 Demonstration of holograms. (a) The ideal phase profile of the Fresnel hologram. Scale bar: 300μm. (b) Optical image of fabricated hologram. Scale bar: 300μm. (c) Simulated hologram at the image plane. Scale bar: 300μm. (d) Measured hologram at the image plane. Scale bar: 300μm.

This hologram lacks the structural symmetry needed for compression and results in a 1GB/mm^2 GDSII file based on 72 nodes being used to define each circle. Encoding the phase information into a single grayscale pattern results in a decrease in the patterning file to 0.4MB/mm^2. The hologram was designed using the Gerchberg-Saxton algorithm resulting in a metasurface with only phase variations. An optical image of the fabricated hologram is shown in Fig.4.13 (b), which also demonstrates the highly aperiodic structure of the metasurface. The hologram was designed to correspond to the Vanderbilt University logo comprising a star with the letter V in the middle, the simulation of which is shown in Fig.4.13 (c). This hologram was measured using a normal

incident laser with the zeroth transmitted image captured by an objective lens. The resulting hologram is shown in Fig.4.13 (d) and demonstrates low background noise, indicating the high quality of the fabricated metasurface.

4.6 Conclusion

In this chapter, I discussed the nanosphere lithography technique for large-scale metasurface fabrication and relevant applications. To be specific, the metasurface-based imaging process, edge detection to be specific, has been demonstrated without any additional digital process. With the assistance of nanosphere lithography method, large-scale (wafer scale) periodic lattices with designed angular optical response can be readily achieved, which can serve as the optical signal processor for machine vision applications in the future. Meta-optics with a more complex k-space response could also be realized by employing multilayer architectures and inverse design for more complex optical analog computing and image filtering.

Moreover, I have developed a novel manufacturing method for nonperiodic, large-scale metasurfaces by combining grayscale lithography with nanosphere self-assembly. This technique allows spatially varying subwavelength nanostructures to be realized with metalenses being used as a proof of concept here, demonstrating diffraction-limited focusing performance. Although defects are unavoidable in self-assembly processes, the relative focusing efficiency of these lenses remained over 83%. Compared to conventional manufacturing platforms such as EBL and UV stepper-based lithography, our proposed method represents a cost-effective technique for large-scale device fabrication. Moreover, no reduction in mask size is necessary due to the encoding of structural variation in a grayscale pattern. The reduction in cost and patterning time associated with this technique could lead to new commercial markets where metasurface-based optics are viable.

Chapter 5

Conclusion and Outlook

5.1 Summary

This dissertation explores the wavefront manipulation ability of compound meta-optic platforms, where multiple metasurface elements were used to extend the engineering freedom. Due to the additional design flexibility, the compound meta-optics can loosen the constraints of traditional single-layer metasurface systems so as to multiplex various functionalities in the entire system. On the same time, compound meta-optics still keep a compact volume factor, allowing for integration with other optoelectronic parts to create an ultra-thin hybrid system. Furthermore, the emergence of a cost-effective manufacturing platform also leverages the potential for future commercial applications. The impacts of this thesis can be discussed from the following several aspects.

In **Chapter 2**, I presented a compound meta-optic system for complex wavefront control. Single-layer metasurface devices for amplitude control typically suffer inevitable efficiency degradation. However, a compound meta-optic system uses a secondary metasurface to shape the diffracted wavefront in order to achieve an independent amplitude and phase control, where phase-only manipulation is applied for the light redistributed between metasurface layers for amplitude manipulation. As a result, compound meta-optic devices offer high-quality and lossless control over field phase and amplitude. To prove the concept, I experimentally demonstrated a beam-former, splitter, and three-dimensional holograms with high field quality. In either case, the measured efficiency of the fabricated meta-optic devices ranged from 65% to 75%.

Furthermore, the birefringent property of meta-atoms was further included for polarization

manipulation in order to regulate the field thoroughly. A stochastic gradient descent based end-to-end optimization algorithm was developed for compound meta-optic system design. As proof of the concept, I experimentally demonstrated a mode division/multiplexer, a mode converter, and a vectorial hologram. The diffraction efficiency for each device reaches around 80%.

In **Chapter 3**, I demonstrated a meta-optic accelerator for multi-functional image classification. The technique is enabled by the unique design freedom afforded by metasurfaces, including the creation of multi-channel lenses to duplicate information and polarization-sensitive kernel layers, which allow for discrimination based on both the spatial intensity profile and the polarization state of the object. The use of polarization demonstrates how optical front-ends are able to access additional information channels usually lost in traditional imaging systems. Furthermore, by implementing end-to-end design, we improved the system's robustness to common noise sources, yielding ~94% experimental classification accuracy, which closely matches the theoretical prediction. The proposed meta-optic accelerators can be massively parallel and serve to bridge the gap between the natural object and digital neural network analysis. This approach can allow one to harness the strengths of both free-space and electronic or optical chip-based architectures.

Moreover, the ability to operate with incoherent illumination enables machine-vision applications with passive ambient lighting, which is incompatible with diffractive neural networks. Meanwhile, the end-to-end optimization also provides a robust platform to balance the trade-off between bandwidth and the aperture size for a meta-optic system. Ultimately, these advantages allow meta-optic accelerators to achieve superior processing speed while also lowering power consumption and thus could lead to advances in a wide range of compact, low-power, and high-speed computer vision systems.

In **Chapter 4**, I presented a large-scale metasurface manufacturing technique based on nanosphere lithography, which is applied to image processing applications. The periodic metasurface, which results in non-local effects between meta-atoms, functions as a high-*k* filter. Hence, only the light signal with a high incident angle can be filtered out with laser illumination, leading to an edge enhancement effect. Meanwhile, this large-scale metasurface device can be readily integrated with other conventional optics, which paves the avenue for small-footprint machine vision applications.

Besides, I also exhibited a novel manufacturing platform for non-periodic large-scale metasurfaces by combining grayscale lithography with nanosphere self-assembly method. This technique allows spatially varying subwavelength nanostructures to be realized with metalenses being used as proof of the concept here, demonstrating diffraction-limited focusing performance. Although defects are unavoidable in self-assembly processes, the relative focusing efficiency of these lenses remained over 83%. Compared to conventional manufacturing platforms such as EBL and UV stepper-based lithography, the proposed method represents a cost-effective technique for large-scale device fabrication. Furthermore, no reduction in mask size is necessary due to the encoding of structural variation in a grayscale pattern. The decreased cost and patterning time associated with this technique could lead to new commercial markets where metasurface-based optics are viable.

5.2 Prospects

The topic of metasurface-based optics has advanced rapidly in recent years. Dielectric metasurfaces can enhance the capabilities of optical systems by mimicking conventional optics in an ultra-compact form factor. The planar architecture further makes metasurfaces a flexible platform for tailoring functionalities by defining the meta-atoms that can be used for various

applications. To date, metasurfaces have been applied to imaging, molecular sensing, quantitative phase mapping, and image processing and have shown flexibility in phase, amplitude, and polarization manipulation. Besides, multi-functional meta-optic devices are also developed as a result of the endeavor to multiplex multiple functionalities into a single device without increasing the device's footprint and manufacturing cost. The emergence of compound meta-optics further provides additional engineering freedom allowing for denser functionalities and superior manipulation abilities.

Meta-optics with planar structures can be easily integrated with other conventional optics to create hybrid systems that offer novel optical functionalities, albeit constrained by diffraction aberrations. In this situation, inverse designing the meta-optic system using an end-to-end optimization platform can considerably improve the device's performance. Besides, a massive, cost-effective manufacturing approach is still needed in order to commercialize metasurface devices in the future. Nowadays, the parallel exposure lithography technique in the semiconductor industry has been explored for meta-optics commercial manufacturing. However, as the optics market is not comparable to that of chips, the fabrication cost is still questionable. In this dissertation, I covered the extra engineering freedom that compound meta-optics offer and their applications in creating sophisticated systems. In addition, I illustrated a cost-effective approach for fabricating metasurfaces. Despite these advances presented in this thesis, there are still plenty of ways to improve the capabilities and functionalities of meta-optic systems. Hereby, I will list some potential opportunities and challenges for compound meta-optics in the future.

One of the significant challenges for compound meta-optics is to further extend engineering freedom. In this dissertation, I have demonstrated that compound meta-optics are capable of complete and lossless field control at a single wavelength. Further increasing the layer

number can barely leverage the freedom of design since multiple planar optics are essentially linear systems. Compound meta-optics, however, still exhibit superior potential as the next-generation multi-functional platform compared to the single-layer metasurface. For instance, single-layer metasurfaces that use angular multiplexing for multi-channel information processing suffer comatic aberration that limits the field of view (FOV). Instead, compound meta-optics could provide wavefront correction by the secondary metasurface to mitigate device aberration.

The precision of the alignment process, particularly for large-scale devices, presents another challenge for compound meta-optics. In this dissertation, I have shown a sub-μm resolution based on an in-situ alignment setup. Nevertheless, such an alignment procedure has a high cost and low efficiency, making it unsuitable for industrial applications. A potential solution is to develop a monolithic fabrication technique to lessen misalignment from manual intervention. Simultaneously, the optimization algorithm can be improved to enhance the alignment tolerance of each layer. In this scenario, a more memory-efficient algorithm should be developed since the calculating system is severely hampered by billions of meta-atoms present in metasurfaces.

Apart from the challenges, metasurface devices can be utilized for various applications due to their multifunctional capabilities. One of the most intriguing areas is optical signal processing. In this paper, I discussed the use of compound meta-optics to accelerate the neural network system. However, the hybrid system is still limited by the digital operations, which are used to provide the nonlinear activation function for signal sorting since a typical metasurface device barely exhibits nonlinear effects at low power excitation. The emergence of volatile phase change materials, such as vanadium dioxide (VO2), offers a chance for all-optical neural network architectures with nonlinear activation operations. Future efforts might be devoted to integrating meta-optics with other phase change materials and optoelectronic components to form more advanced optical neural

network architectures.

Finally, the commercialization of metasurfaces, in my opinion, still possesses tremendous potential, for which a more affordable, parallel manufacturing platform should be developed. In this thesis, I presented a fabrication method based on nanosphere-assisted grayscale lithography, while the nanosphere mask cannot be recycled. Besides, nanosphere dislocation is inevitable during self-assembly, leading to defects in metasurfaces. One potential solution to overcome these limitations is to combine interference and grayscale lithography, where the incident angles of multiple laser beams can precisely dictate the lattice of metasurfaces. This approach can be potentially applied to the widespread production of metasurface devices.

Appendix A

Fundamentals of Metasurfaces

A.1 Sampling Rule for Metasurfaces

The sampling of metasurfaces obeys the Nyquist criterion, which requires that the minimum sampling rate should be twice the maximum object spatial frequency, which means for the single zone with phase variation from 0 to 2π, there must include at least two meta-atoms. Assume the metasurface has a lattice constant of P, then it should satisfy the following equation:

$$\max\big(\phi(x+P)-\phi(x)\big) \le \pi \tag{A.1}$$

When P is small enough, the numerical differentiation can be calculated as follows:

$$P \cdot \max\left(\lim_{P\to 0}\frac{\phi(x+P)-\phi(x)}{P}\right) = P \cdot \max\left(\frac{d\phi}{dx}\right) \le \pi \tag{A.2}$$

A.2 Jones Calculus for Birefringent Metasurfaces

Polarization conversion is a unique property of metasurfaces arising from the birefringent meta-atoms structure. By designing anisotropic meta-atoms, cylindroids, for instance, the phase response along the orthogonal direction can be independently controlled by the length of elliptical axes. The control process of birefringent meta-atoms can be described by the Jones calculus. Consider a polarization-sensitive input electrical field, the output field can be represented by the following equation:

$$\begin{bmatrix}E_{x,out}\\E_{y,out}\end{bmatrix} = \begin{bmatrix}cos(\theta) & -sin(\theta)\\sin(\theta) & cos(\theta)\end{bmatrix}\begin{bmatrix}e^{i\phi_x} & 0\\0 & e^{i\phi_y}\end{bmatrix}\begin{bmatrix}cos(\theta) & sin(\theta)\\-sin(\theta) & cos(\theta)\end{bmatrix}\begin{bmatrix}E_{x,in}\\E_{y,in}\end{bmatrix} \tag{A3}$$

where $E_{x,in}$, $E_{y,in}$ and $E_{x,out}$, $E_{y,out}$ are the x and y polarized incident and transmitted amplitude.

ϕ_x and ϕ_y are the phase shifts provided by the resonator for *x* and *y* polarization. θ is the pillar rotation angle, which is the variable of a rotation matrix:

$$R(\theta) = \begin{bmatrix} cos(\theta) & -sin(\theta) \\ sin(\theta) & cos(\theta) \end{bmatrix} \tag{A4}$$

Therefore, the output field can be analytically represented by:

$$\begin{bmatrix} E_{x,out} \\ E_{y,out} \end{bmatrix} = \begin{bmatrix} e^{i\phi_x}cos^2(\theta) + e^{i\phi_y}sin^2(\theta) & \frac{1}{2}\left(e^{i\phi_x} - e^{i\phi_y}\right)sin(2\theta) \\ \frac{1}{2}\left(e^{i\phi_x} - e^{i\phi_y}\right)sin(2\theta) & e^{i\phi_x}sin^2(\theta) + e^{i\phi_y}cox^2(\theta) \end{bmatrix} \begin{bmatrix} E_{x,in} \\ E_{y,in} \end{bmatrix} \tag{A5}$$

If we only consider *x*-polarized light input and *y*-polarized output, the transmission can be simplified as follows:

$$E_{y,out} = \left(e^{i\phi_x} - e^{i\phi_y}\right)sin(\theta)cos(\theta)E_{x,in} \tag{A6}$$

After a simple algebraic transformation, we can get,

$$E_{y,out} = \frac{1}{2}e^{i\phi_x}\left[1 - e^{i(\phi_y - \phi_x)}\right]sin(2\theta)E_{x,in} \tag{A7}$$

If the condition $\phi_y - \phi_x = \pi$ is satisfied for arbitrary ϕ_x, then the final transmission is described by,

$$E_{y,out} = e^{i\phi_x}sin(2\theta)E_{x,in} \tag{A8}$$

Eq.A8 demonstrates the amplitude and phase of the output field can be independently controlled by ϕ_x and the rotation of angle meta-atoms, θ, leading to a complex-valued manipulation.

A.3 Refractive Index of Silicon

The optical properties of silicon used in the paper were characterized by the ellipsometry method. Two kinds of silicon are involved: low-pressure (LPCVD), and plasma-enhanced

(PECVD) chemical vapor deposited silicon. The refractive index, as well as extinction ratio, are shown in Fig.A.1, which exhibits lossless performance at the working wavelength designed in this paper.

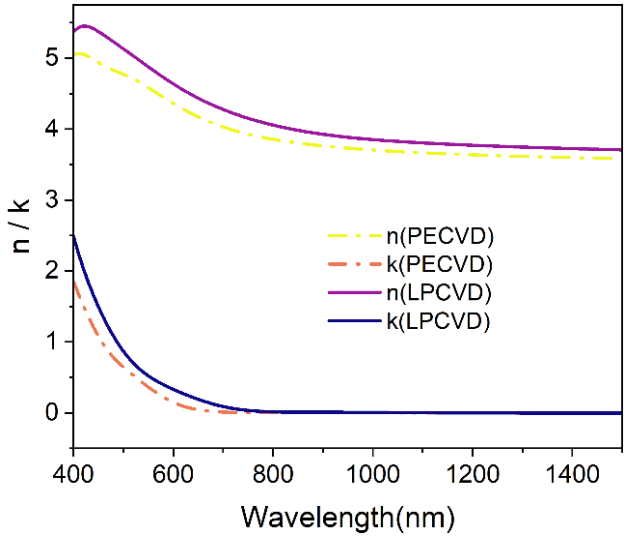

Figure A.1 Optical properties of low-pressure (LPCVD) and plasma-enhanced (PECVD) chemical vapor deposited Si films.

A.4 Angular Spectrum Propagation Method

The light propagation behavior in free space can be theoretically described by the angular spectrum expansion method, for which a complex amplitude $U(x, y, z)$ will be decomposed into a series of plane waves $A(f_X, f_Y; z)$ with various spatial frequency f_X and f_Y by Fourier transformation. The complex amplitude can be retrieved from the inverse Fourier transformation over angular spectrum components. Therefore, consider a coherent light propagates in free space from $z|_{z=0}$ to $z|_{z=z}$, the angular component at $z|_{z=0}$ can be described as:

$$A(f_X, f_Y; 0) = \iint_{-\infty}^{\infty} U(x, y, 0) e^{-i2\pi(f_X x + f_Y y)} dx dy = \mathcal{F}\{U(x, y, 0)\} \tag{A9}$$

$$U(x, y; 0) = \iint_{-\infty}^{\infty} A(f_X, f_Y; 0) e^{i2\pi(f_X x + f_Y y)} df_X df_Y = \mathcal{F}^{-1}\{A(f_X, f_Y; 0)\} \tag{A10}$$

Consider one of the components within the angular spectrum, which is a plane wave propagating

along a particular direction, the propagation behavior correlated to spatial frequency can also be described by direction cosine α, β, γ. According to the definition of spatial frequency: $\alpha = \lambda f_X, \beta = \lambda f_Y$ and $\gamma = \sqrt{1-\alpha^2-\beta^2}$, the plane wave with a specific spatial frequency can be described as:

$$A(f_X, f_Y; 0) = ae^{i2\pi(f_X x + f_Y y)} = ae^{i2\pi\left(\frac{\alpha}{\lambda}x + \frac{\beta}{\lambda}y\right)} = A\left(\frac{\alpha}{\lambda}, \frac{\beta}{\lambda}; 0\right) \tag{A11}$$

where a is the amplitude of the plane wave. Therefore, the angular spectrum at $z|_{z=0}$ and $z|_{z=z}$ can be written as:

$$A\left(\frac{\alpha}{\lambda}, \frac{\beta}{\lambda}; 0\right) = \iint_{-\infty}^{\infty} U(x, y, 0) e^{-i2\pi\left(\frac{\alpha}{\lambda}x + \frac{\beta}{\lambda}y\right)} d\frac{\alpha}{\lambda} d\frac{\beta}{\lambda} = \mathcal{F}\{U(x, y, 0)\} \tag{A12}$$

$$A\left(\frac{\alpha}{\lambda}, \frac{\beta}{\lambda}; z\right) = \iint_{-\infty}^{\infty} U(x, y, z) e^{-i2\pi\left(\frac{\alpha}{\lambda}x + \frac{\beta}{\lambda}y\right)} d\frac{\alpha}{\lambda} d\frac{\beta}{\lambda} = \mathcal{F}\{U(x, y, z)\} \tag{A13}$$

Hence, the interested complex amplitude at $z|_{z=z}$ in free space is:

$$U(x, y; z) = \iint_{-\infty}^{\infty} A\left(\frac{\alpha}{\lambda}, \frac{\beta}{\lambda}; z\right) e^{i2\pi\left(\frac{\alpha}{\lambda}x + \frac{\beta}{\lambda}y\right)} d\frac{\alpha}{\lambda} d\frac{\beta}{\lambda} = \mathcal{F}^{-1}\left\{A\left(\frac{\alpha}{\lambda}, \frac{\beta}{\lambda}; z\right)\right\} \tag{A14}$$

For every point in free space, the complex amplitude must obey the constriction of the Helmholtz equation:

$$\nabla^2 U + \boldsymbol{k}^2 U = 0 \tag{A15}$$

where $\boldsymbol{k} = \frac{2\pi}{\lambda}(\alpha \boldsymbol{x} + \gamma \boldsymbol{y} + \beta \boldsymbol{z})$ is the wavenumber in free space. Apply constriction (A15) to (A14), $A\left(\frac{\alpha}{\lambda}, \frac{\beta}{\lambda}; z\right)$ must obey the following equation:

$$\frac{d^2}{dz^2} A\left(\frac{\alpha}{\lambda}, \frac{\beta}{\lambda}; z\right) + \left(\frac{2\pi}{\lambda}\right)^2 [1 - \alpha^2 - \beta^2] A\left(\frac{\alpha}{\lambda}, \frac{\beta}{\lambda}; z\right) = 0 \tag{A16}$$

which has the eigensolution:

$$A\left(\frac{\alpha}{\lambda},\frac{\beta}{\lambda};z\right)=A\left(\frac{\alpha}{\lambda},\frac{\beta}{\lambda};0\right)e^{i\frac{2\pi}{\lambda}\sqrt{1-\alpha^2-\beta^2}z} \tag{A17}$$

Therefore, provided the complex amplitude $U(x,y;0)$, the field $U(x,y,z)$ after light propagating by a distance of z can be derived by:

$$U(x,y,z)=\iint_{-\infty}^{\infty}A\left(\frac{\alpha}{\lambda},\frac{\beta}{\lambda};0\right)e^{i\frac{2\pi}{\lambda}\sqrt{1-\alpha^2-\beta^2}z}\times circ\left(\sqrt{\alpha^2+\beta^2}\right)e^{i2\pi\left(\frac{\alpha}{\lambda}x+\frac{\beta}{\lambda}y\right)}d\frac{\alpha}{\lambda}d\frac{\beta}{\lambda} \tag{A18}$$

$$U(x,y,z)=\mathcal{F}^{-1}\left\{\mathcal{F}\{U(x,y,0)\}\times e^{i\frac{2\pi}{\lambda}\sqrt{1-\alpha^2-\beta^2}z}\times circ\left(\sqrt{\alpha^2+\beta^2}\right)\right\} \tag{A19}$$

where *circ* is the circular region function, which can omit the evanescent components during light propagation.

Appendix B

Compound Meta-optics for Field Control

B.1 Gerchberg-Saxton Algorithm

The Gerchberg-Saxton (GS) algorithm, proposed by Gerchberg and Saxton in 1972, is a kind of iterative phase retrieval algorithm for computer-generated hologram applications. The algorithm shown in Fig.B.1 retrieves the phase distribution at a specific plane while generating the hologram at the designed plane, which is the Fresnel hologram. Compared to Fraunhofer hologram requiring Fourier transform to obtain the desired amplitude distribution, Fresnel hologram can utilize the light propagation behavior in free space to generate the field without any extra optics involved, which can be applied to redistribute the incident field intensity.

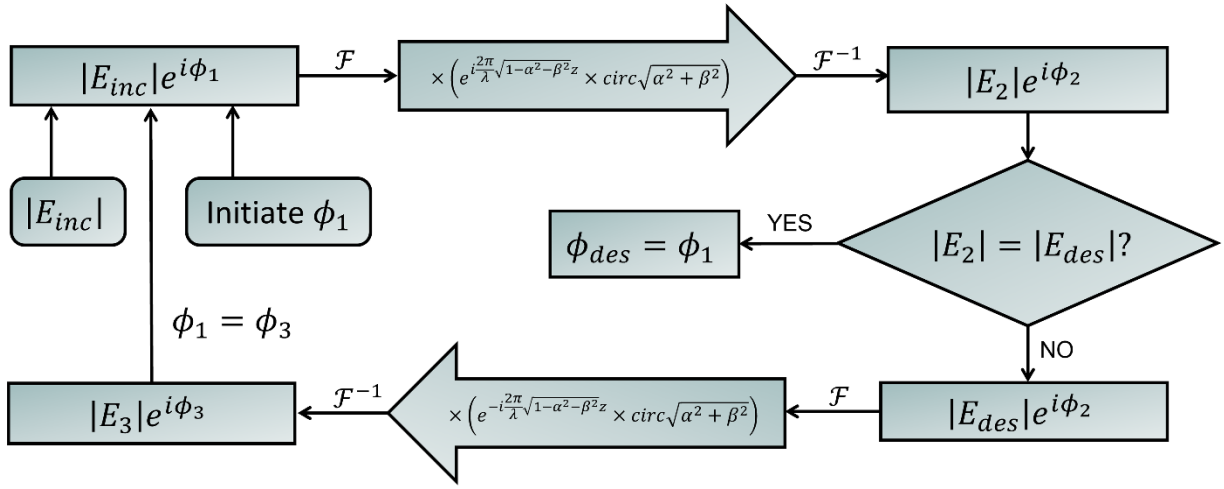

Figure B.1 The schematics of Gerchberg-Saxton algorithm to generate phase-only hologram.

In order to achieve the Fresnel hologram by GS algorithm, a uniform amplitude with a random phase distribution was used as the input field as shown in Fig.B.1. The light propagation

between two planes with a certain distance z can be described by the angular spectrum propagation process, where the light field will be converted into an angular spectrum by Fourier transformation, with modulation by the transfer function over a series of plane waves, light distribution can be spatially reconstructed by inverse Fourier transformation (see details in Appendix A.3). The amplitude of revamped field was then replaced by the desired value as the constraint while maintaining the phase distribution. Then, a backpropagation operation was performed over the reconstructed light resulting in a retrieved phase profile as well as the non-useful amplitude distribution, which the amplitude of incident field will further replace. After tens of iterations, the amplitude distribution of the output field will match well with the designed value, while the retrieved phase became the target to generate the desired hologram.

Since the hologram generated by GS algorithm is based on light propagation and the constraint over the amplitude distribution at the target plane, the hologram phase distribution cannot be well controlled. Therefore, such hologram always suffers speckles due to the interference from the undesired phase distribution, leading to non-uniform and low-quality field distribution. However, an extra metasurface layer can correct the undesired phase distribution in the compound optic system, resulting in fully complex-amplitude control and high-quality holograms.

B.2 In-situ Alignment System for Compound Meta-optics

During the alignment process of compound meta-optics, the bottom metasurface layer was mounted on a rotation stage held by a vacuum pump. The top layer was attached to a glass slide suspended by an XYZ translation stage, as shown in Fig.B.2 (a) and (b). A drop of uncured PDMS was applied in between as an index-matched layer. The samples were then illuminated from the bottom by a collimated supercontinuum laser that was passed through a monochromator set at the

designed working wavelength. The far-field images after the bilayer metasurface were recorded by a near-infrared (NIR) camera through an imaging system consisting of a 20X objective and a tube lens. The holograms were then aligned by tuning the XYZ translation and rotation stage.

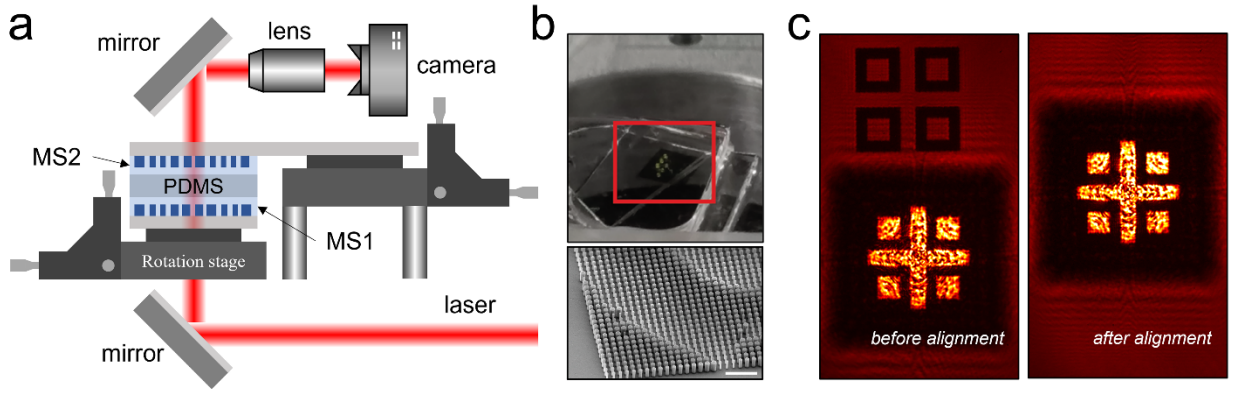

Figure B.2 In-situ bilayer metasurfaces alignment setup. (a) Schematic of the meta-optic assembly, alignment, and characterization process. Each metasurface is fabricated individually and then aligned to form the meta-optic device. (b) Top: an optical image of the manufactured meta-optic device, where the two metasurface layers are being aligned. Bottom: a scanning electron microscope (SEM) image of a portion of one metasurface, showing the array of silicon nanopillars. Scale bar: 3μm. (c) The alignment hologram is used to assist the vertical and lateral alignment process.

Accurate alignment between the two metasurfaces ($< 1\mu m$ lateral misalignment) is necessary to obtain the desired complex-valued field transformation. To achieve this, we developed hologram alignment marks formed by silicon arrays fabricated near each of the two metasurfaces. The array near metasurface 1 was designed using the GS algorithm to create a cross-shaped intensity pattern at the desired distance of metasurface 2 as shown in Fig.B.2 (c). As a result, the hologram transfers location information from layer 1 to the same plane as layer 2. The nanopillar array near metasurface 2 contains a pattern of low transmission nanopillars tracing the alignment hologram outline. Since the alignment hologram was fabricated through the EBL system, the displacement error, dictated by the stitching error from the exposure system, can be below 20nm. The two metasurfaces are accurately aligned by positioning layer 2 so that the low-

transmission outline is not visible when illuminated by the alignment hologram. After spatial alignment was achieved with the alignment marks, the alignment was further adjusted until the desired intensity image was formed at a distance beyond the meta-optic output. Misalignment introduces phase error to the output field distribution, and the output field phase defines the propagation behavior of the wave, so the alignment improves as the observed intensity image improves.

B.3 Methods for Birefringent and Complex-valued Field Control

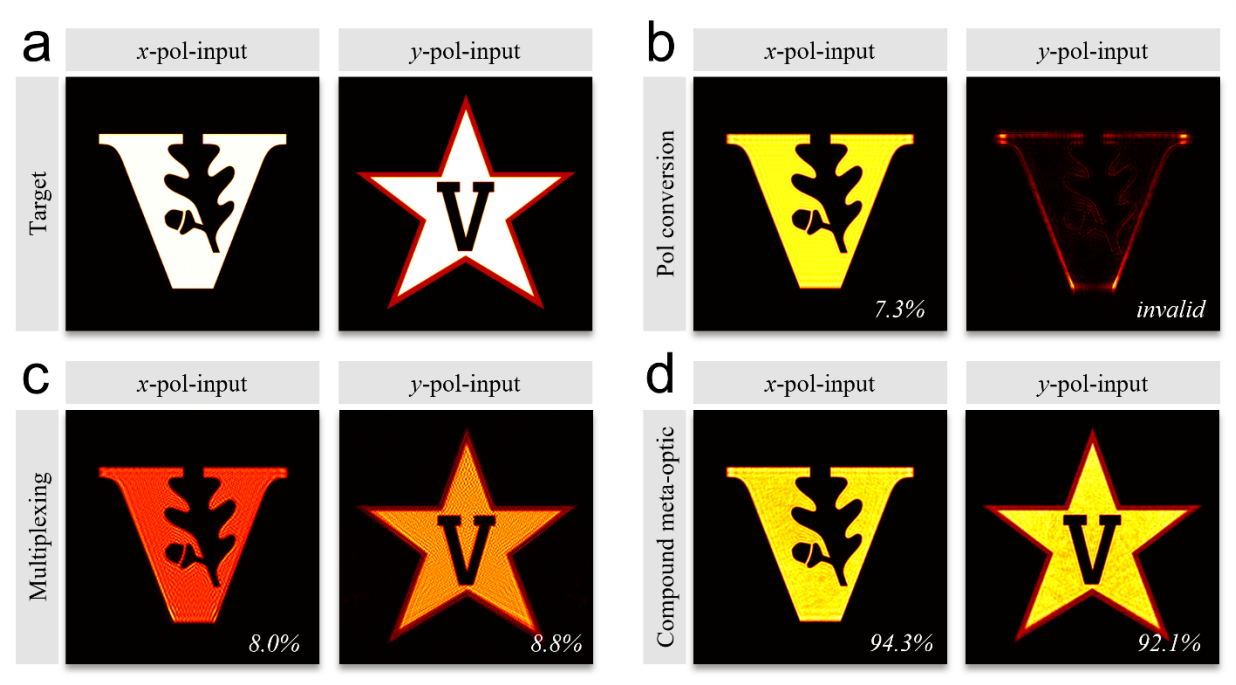

Figure B.3 Comparison of the birefringent manipulation abilities of different methods. (a) The target field for different polarization channels. (b) The manipulation results are based on the polarization conversion process from a single-layer metasurface. (c) The manipulation results are based on the spatial multiplexing method from a single-layer metasurface. (d) The manipulation results from a bilayer meta-optic system. All the amplitude profile is normalized to their maximum.

A comparison of different methods for birefringent complex-field control is shown in Fig.B.3. Here, I designed a polarization multiplexed multi-channel hologram device. The target

hologram is shown in Fig.B.3 (a) and comprises a "V" logo for *x*-polarized illumination and a star logo for *y*-polarized illumination.

Fig.B.3 (b) illustrates the simulated hologram results formed by the polarization conversion method, where an exact complex-valued field is provided by a single-layer metasurface. By controlling the birefringent property of meta-atoms, shown in the manuscript, the complex-valued transmission coefficient for each meta-atom is given by,

$$E_{y,\,out} = \left(e^{i\phi_y} - e^{i\phi_x}\right)\sin(\theta)\cos(\theta)E_{x,\,in} \tag{B1}$$

where θ is the rotation angle of the nano-pillar meta-atom, ϕ_x and ϕ_y are the phase delay induced by the meta-atom along the *x* and *y*-axis. The amplitude and phase of the field can be independently manipulated using this method. However, the optical response is polarization sensitive, and due to the polarization conversion process, and the required polarizers, the efficiency drops to 7.3%.

The spatial multiplexing method can provide polarization-insensitive control as shown in Fig.B.3 (c). In this method, the supercell structure, which includes independent unit cells in neighboring lattices, was used to achieve complex-valued control. The transmissive coefficient for each supercell is given by,

$$E_{out} = \frac{1}{2}\left(e^{i\phi_y} + e^{i\phi_x}\right)E_{in} \tag{B2}$$

Here, independent amplitude and phase control for unpolarized light can be achieved. However, the supercell architecture will generate higher diffraction orders resulting in low device efficiency.

The compound meta-optic utilizes light redistribution during propagation, which can provide independent control over amplitude and phase while maintaining an overall device efficiency of over 90% as shown in Fig.B.3 (d). Moreover, the meta-optic is polarization insensitive, providing more design freedom for optical systems.

B.4 Role of *k*-space Filter in the End-to-end Optimization Platform

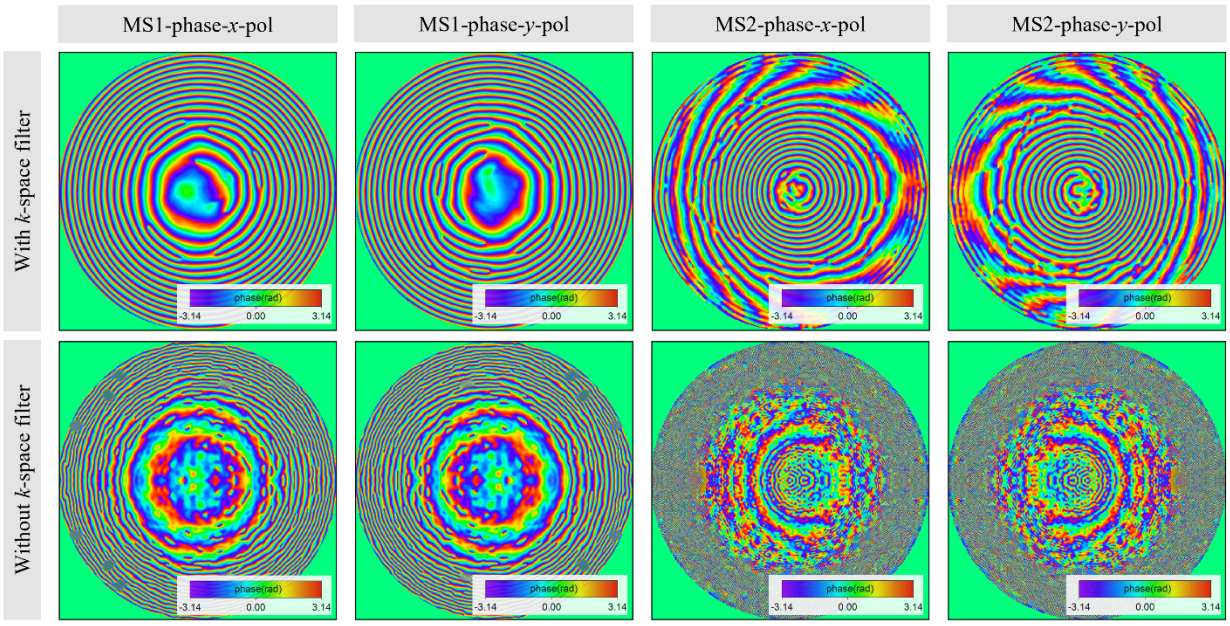

Figure B.4 Comparison of compound meta-optic phase profiles. The phase profiles for spatial mode division/multiplexing with (upper row) and without (bottom row) a *k*-space filter used during the optimization process.

Fig.B.4 shows the phase profile for spatial division/multiplexing after optimization with (upper row) and without (bottom row) the *k*-space constraints. The *k*-space constraint filters out light with a large divergent angle, leading to a smoother phase profile.

B.5 Target Fields of Meta-optics for Complete Field Control

In order to simulate the optical response to unpolarized light, the light was divided into two orthogonal linear-polarized states with equal intensity. For each state, the optical response of the meta-optic was calculated using the following equation,

$$E(x, y, p_{out}) = \mathcal{R}(d_2)\mathcal{M}(\phi_{x2}, \phi_{y2}, \theta_2)\mathcal{R}(d_1)\mathcal{M}(\phi_{x1}, \phi_{y1}, \theta_1)E(x, y, p_{in}) \quad \text{(B3)}$$

where p is the polarization state, $\mathcal{R}$ is the light propagation in free space, $\mathcal{M}$ is the metasurface manipulation dictating the phase discontinuity and polarization conversion process, and E is the

complex-valued output field containing all polarization states. The optical response to each linear-polarized input was calculated separately. Since the input light is incoherent due to orthogonality, no interference occurs between the two output fields. Hence, the final field was calculated by summing the optical intensity of the two independent light sources.

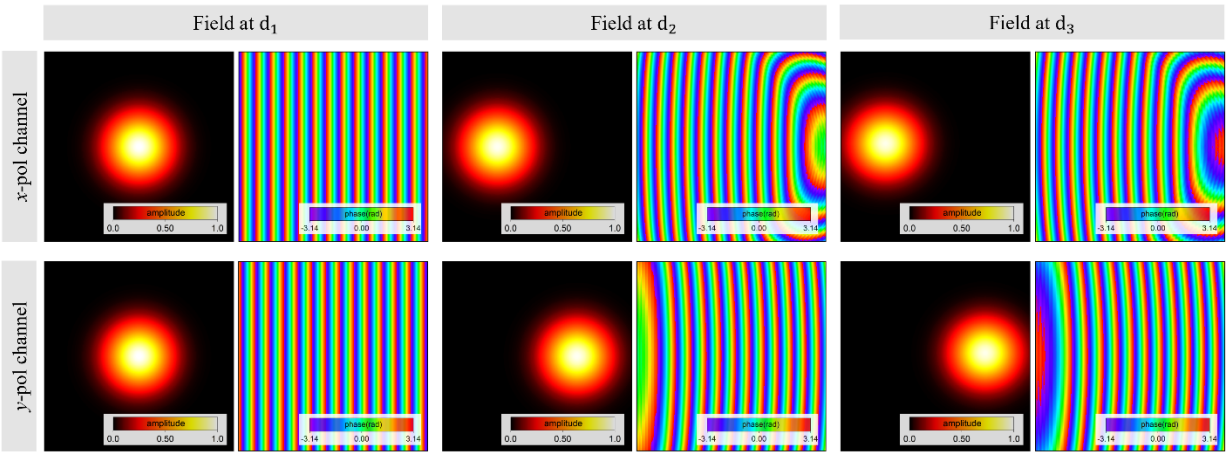

Figure B.5 Target fields for spatial mode division/multiplexing. The target field comprises multiple complex-valued profiles at different propagation depths, d, from the second metasurface. The output field was separated into different polarization channels. $d_1 = 0$, $d_2 = 2000\mu m$, $d_3 = 2500\mu m$.

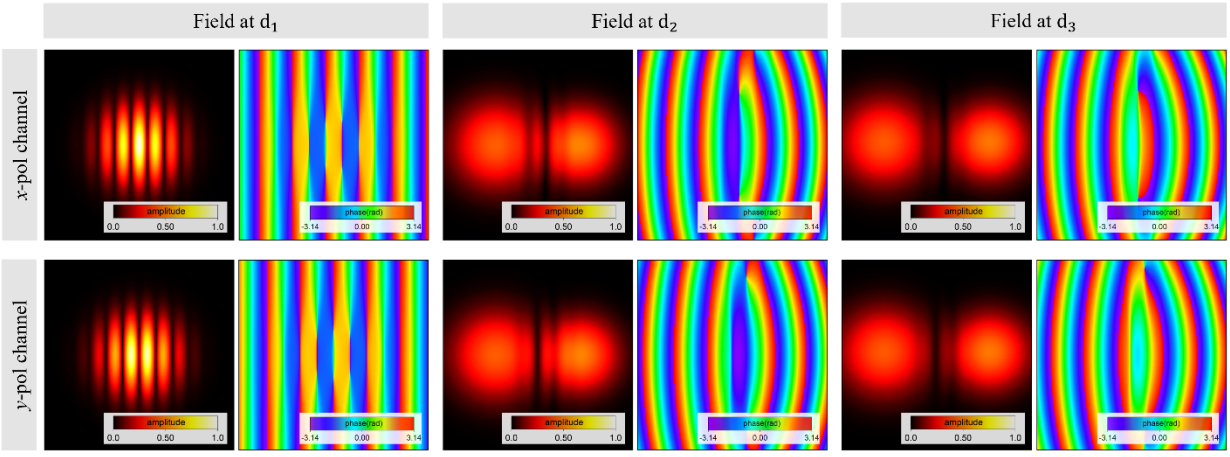

Figure B.6 Target fields for the spatial mode converter. The target field comprises multiple complex-valued profiles at different propagation depths, d, from the second metasurface. The field was separated into different polarization channels. Only an x-polarized plane wave was used as the input field. Polarization conversion was used in the design process. $d_1 = 0$, $d_2 = 2000\mu m$, $d_3 = 2500\mu m$.

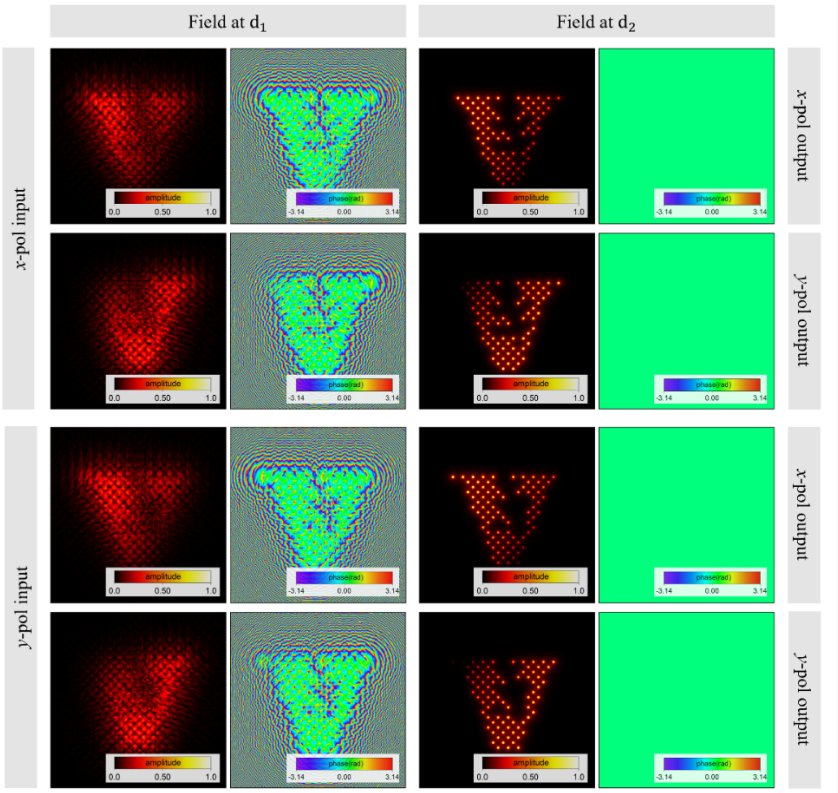

Figure B.7 Target fields for the universal vectorial hologram. The target field comprises multiple complex-valued profiles at different propagation depths, d, from the second metasurface. The field was separated into different polarization channels according to input field states. Polarization conversion was used in the design process. $d_1 = 0$, $d_2 = 125\lambda_0$.

B.6 Arbitrary Mode Conversion Using Compound Meta-optics

Here, we demonstrate a multi-channel mode converter, which can convert an x-polarized plane wave into multiple channels with arbitrary polarization states. The target amplitude for the mode converter is described as follows:

$$\begin{bmatrix} E_x \\ E_y \end{bmatrix} = \tag{B4}$$

$$\begin{bmatrix} e^{ik_0\left(xsin(-2^\circ)+ysin(3^\circ)\right)} & e^{ik_0\left(xsin(3^\circ)+ysin(0^\circ)\right)}e^{i\pi/2} & e^{ik_0\left(xsin(-2^\circ)+ysin(-2.5^\circ)\right)}e^{i3\pi/4} \\ e^{ik_0\left(xsin(-2^\circ)+ysin(3^\circ)\right)} & e^{ik_0\left(xsin(3^\circ)+ysin(0^\circ)\right)} & e^{ik_0\left(xsin(-2^\circ)+ysin(-2.5^\circ)\right)} \end{bmatrix} \begin{bmatrix} 0.8e^{-(r/15\lambda_0)^2} \\ e^{-(r/20\lambda_0)^2} \\ 1.5e^{-(r/25\lambda_0)^2} \end{bmatrix}$$

Eq.B4 gives the analytical description of the complex-valued target field for the compound meta-optic, which consists of three independent Gaussian beams with different deflection angles.

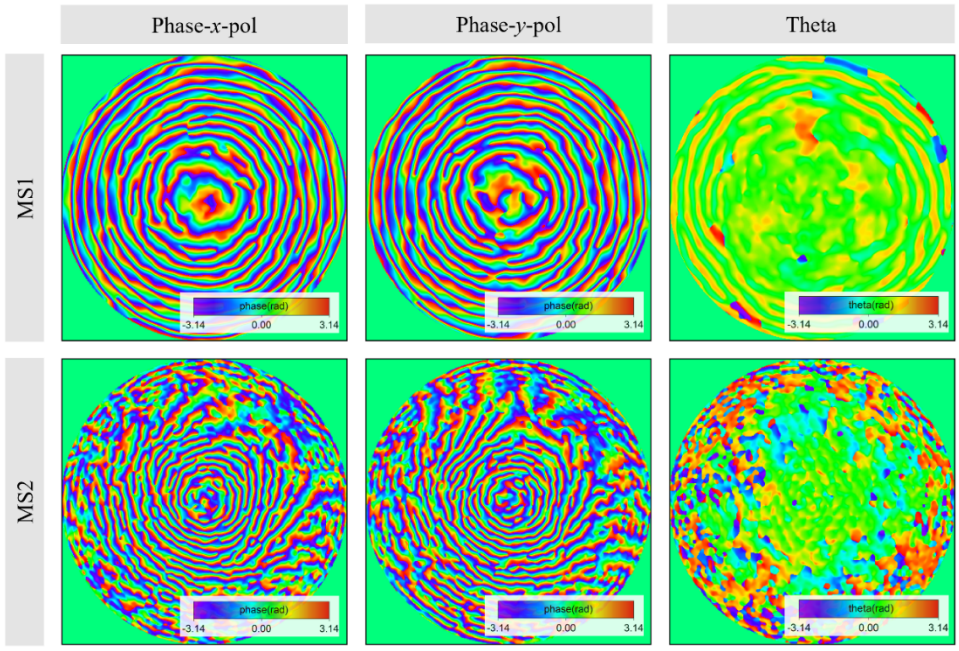

Figure B.8 Phase profiles for the multi-channel mode converter.

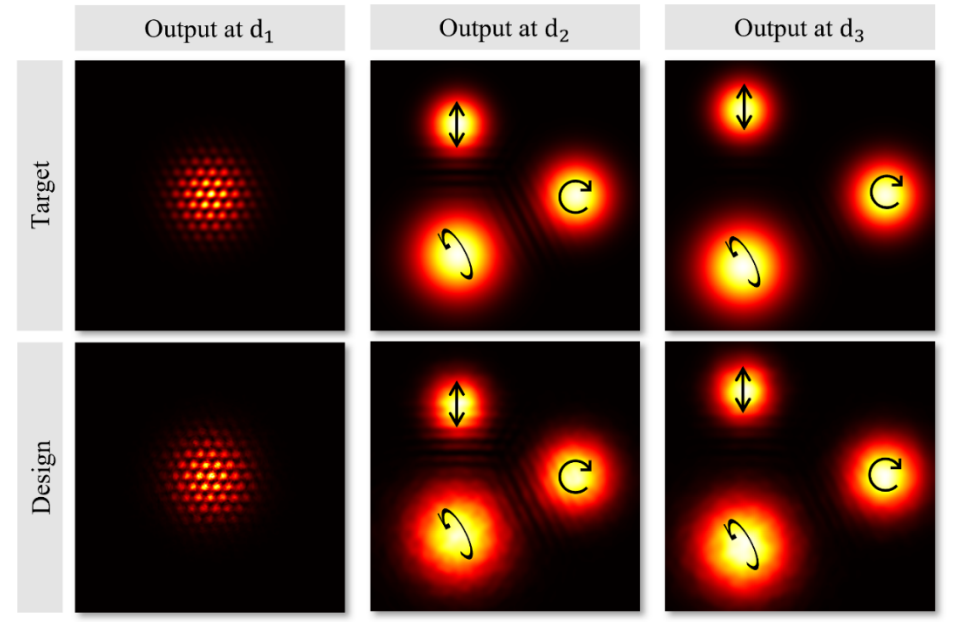

Figure B.9 Comparison of the multi-channel mode converter's target and simulated intensity profiles.

Each Gaussian beam carries an independent polarization state, including linear, circular, and elliptical polarizations. Fig.B.8 shows the optimized phase and rotation angle profiles of the metasurfaces arising from the end-to-end inverse design platform described in the manuscript. The

comparison of the target and optimized output intensity profiles are provided in Fig.B.9, which exhibits excellent agreement. The theoretical diffraction efficiency is 95.9%.

Appendix C

Meta-optic Accelerators for Object Classifiers

C.1 Meta-atoms for Meta-optic Accelerators

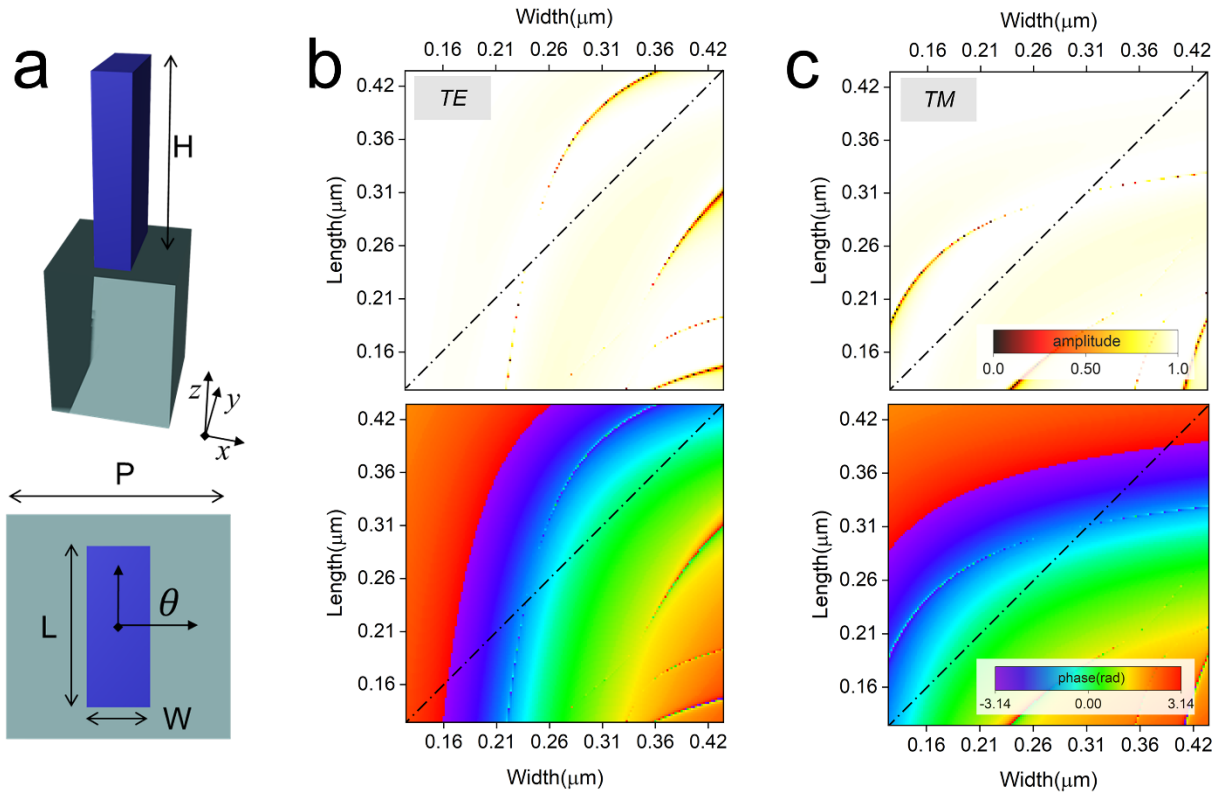

Figure C.1 The simulation results of meta-atoms used in the manuscript. (a) The schematics of birefringent meta-atom composed of silicon nanopillar on glass. The height was fixed at 880nm with a period of 600nm at a working wavelength of 1.3μm. θ is set as 0 to extract the fundamental mode response under TE and TM excitation. (b) The amplitude and phase profile as a function of the width and length of silicon nanopillar. The input light is polarized in TE mode (along y-axis). (c) The amplitude and phase profile under TM mode (along x-axis) excitation.

In order to design the metasurface, the α-silicon based nanopillars were chosen as the basic meta-atoms. The complex transmission coefficient of nanopillar meta-atoms was calculated using rigorous coupled wave analysis (RCWA) with a schematic of the unit cell displayed in Fig.C.1 (a). The height and period of the silicon structure were fixed at 880nm and 600nm, respectively, with

a material index of 3.62 and an illumination wavelength of 1.3μm. Considering the subwavelength period, only the fundamental (zeroth) transmission mode (both TM and TE) was extracted from the simulation. During the parameter (width and length) scanning, the rotation angle, θ, was set as 0, which forms the birefringent optical response map shown in (b) and (c). The dash lines in (b) and (c) indicate the isotropic optical response (polarization insensitive), which was used for the multi-channel metalens design.

C.2 Optical Characterization Setup for Meta-optic Accelerators

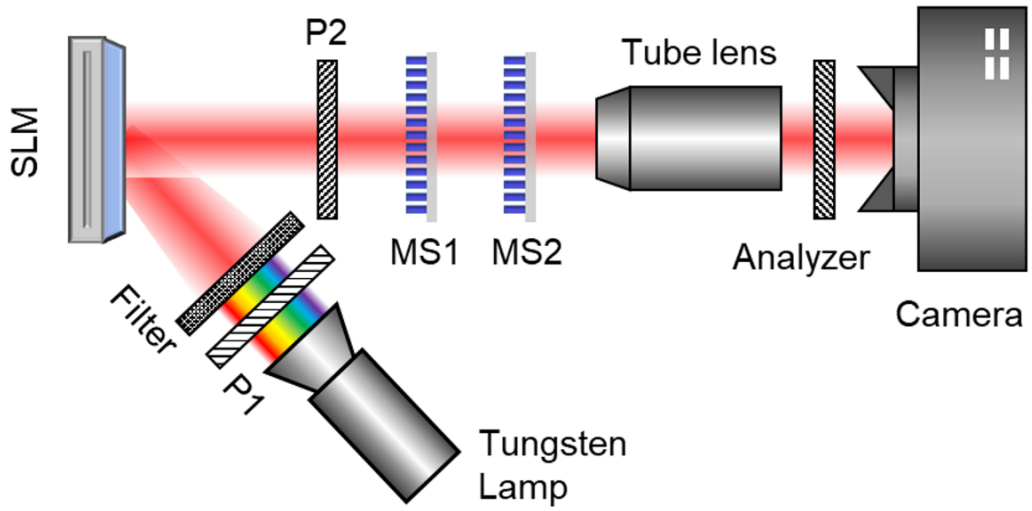

Figure C.2 The characterization setup of optical neural network. P means the polarizer. MS is the metasurface.

For proof of the concept, the proposed compound metasurface system was characterized based on a customized optical setup, as shown in Fig.C.2. A commercial liquid-crystal-based SLM (PLUTO-2.1-Phase-only, Holoeye) was used to create the optical images using illumination from an incoherent light source (66997-100Q-R085, Newport) with a band-pass filter (FB1300-30, Thorlabs). The SLM modulates the polarization state of the light, which is converted into amplitude control by using a polarizer and analyzer before and after the SLM. The multi-channel

metasurface system was then used to project and modulate the image, whose feature map was recorded by the camera using a tube lens and a polarizer placed in front.

C.3 Meta-optic Accelerators for Complex Signal Recognition

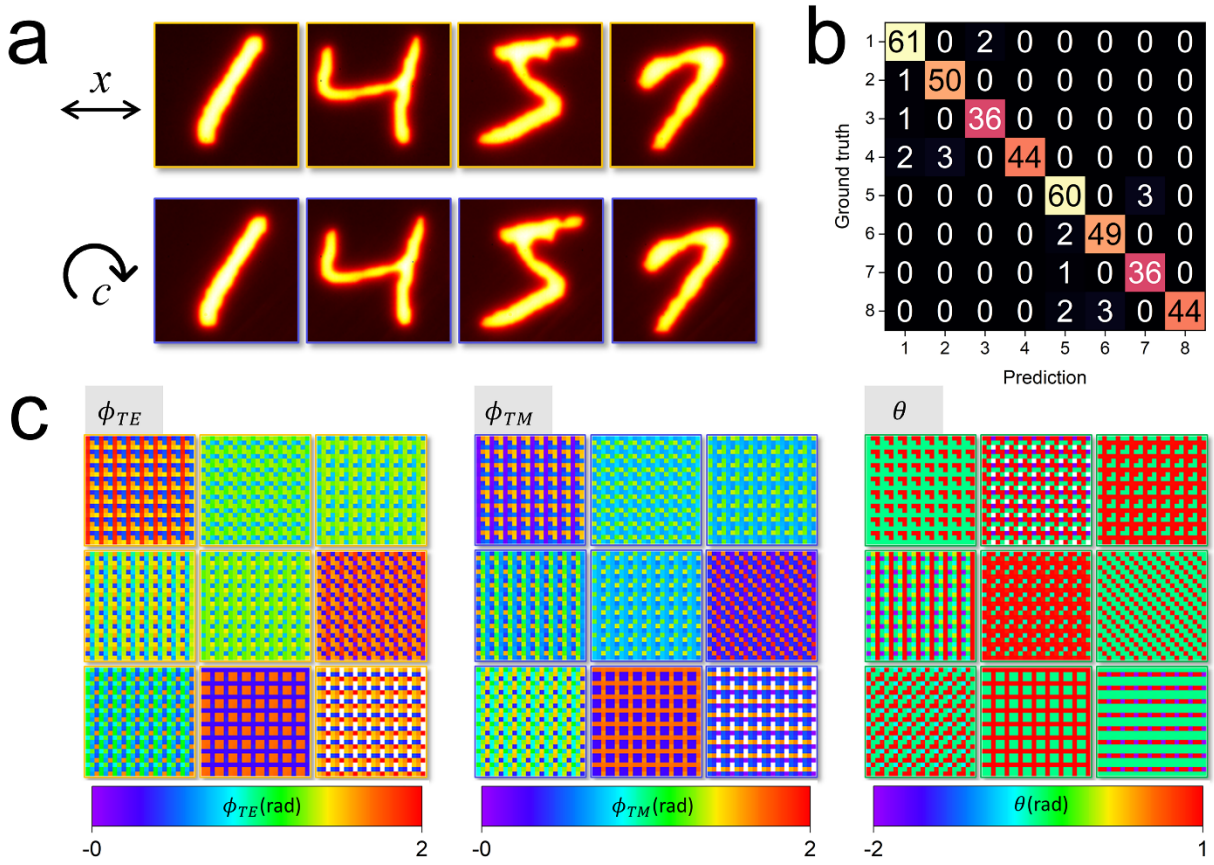

Figure C.3 Demonstration of complex polarization states classification. (a) The data library is trained for the multifunctional neural network. The amplitude information contains four categories. Each category includes two different polarization states, one is linear and another is circular-polarized. (b) The tested confusion matrix is based on the pre-trained neural network. (c) The pre-trained metasurface kernel layers are represented by the phase and rotation map.

A more complex, non-orthogonal signal classification can also be achieved using this approach as shown in Fig.C.3. Here, four different amplitude objects were employed with each object having two different polarization states, linear and circularly polarized. Apart from intensity

control, a metasurface kernel also needs to convert the polarization state into a unique intensity value, where phase manipulation along orthogonal directions is necessary. Hence, during the end-to-end optimization process, I designed not only the rotation angle of meta-atoms but also the width and length, indicating phase control, in the unit cell. The confusion matrix is presented in Fig.C.3 (b) and demonstrates 95% accuracy. Fig.C.3 (c) also gives the pre-trained parameters of the metasurface kernel layer containing the phase and rotation map.

Appendix D

Nanosphere Lithography based Large-scale Metasurfaces

D.1 Nanosphere Lithography Procedure

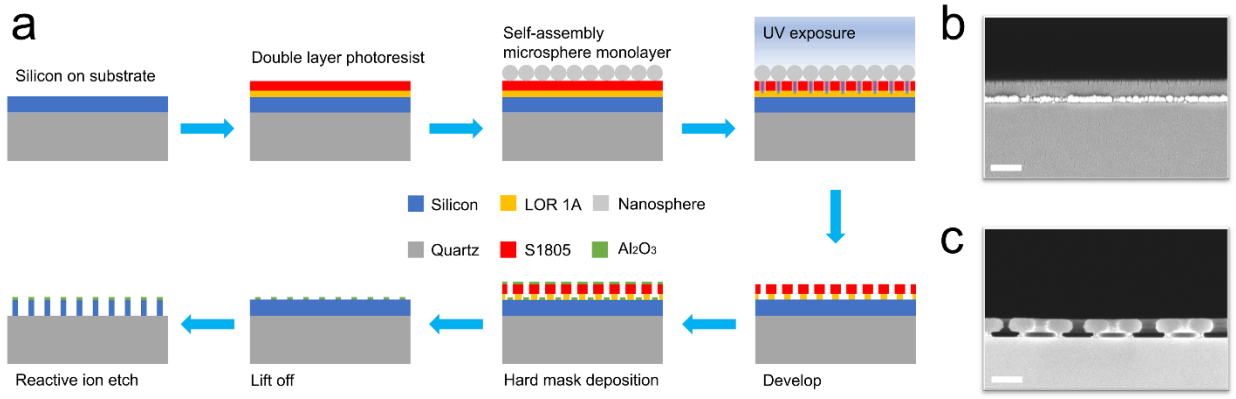

Figure D.1 Schematic of the nanosphere self-assembly assisted grayscale lithography process. (a) Illustration of each fabrication step. (b) Side-view SEM image of bilayer photoresist structure. Scale bar: 400nm. (c) SEM cross-section of the undercut structure resulting from the bilayer photoresist. Scale bar: 400nm.

The detailed fabrication process based on nanosphere lithography is exhibited in Fig.D.1. Starting with amorphous silicon (850nm) on a quartz substrate, the bilayer layer photoresist comprising LOR 1A (Kayaku Advanced Materials, Inc.) and Microposit S1805 was spun coat successively at 6000 rpm for 45s as shown in Fig.D.1 (b). The bilayer photoresist creates an undercut structure, shown in Fig.D.1 (c), that makes it easier to lift off the hard mask material. After spin coating, a 2-minute soft bake at 230C° and 115C° was used to cure the bottom and top layers. The nanosphere monolayer was then self-assembled and transferred onto the substrate as a nano lens array for exposure. The designed pattern, either grayscale or uniform, was then illuminated over the nanosphere surface, with the exposed area under each nanosphere controlled

by the illumination intensity. The total exposure time was fixed at 1.25s. The nanosphere array was then removed from the substrate by immersing it in deionized (DI) water with sonication. A 2-minute post-bake at 115℃ is performed to strengthen the photoresist before developing in Tetramethylammonium hydroxide-based developer (Microposit MF-319). Next, 40nm of Al_2O_3 was thermally deposited at a rate of 0.5 Å/s as the hard mask. The final device was completed using reactive ion etching (RIE) to form silicon pillars.

D.2 Optical Characterization Setup for Large-scale Metasurfaces

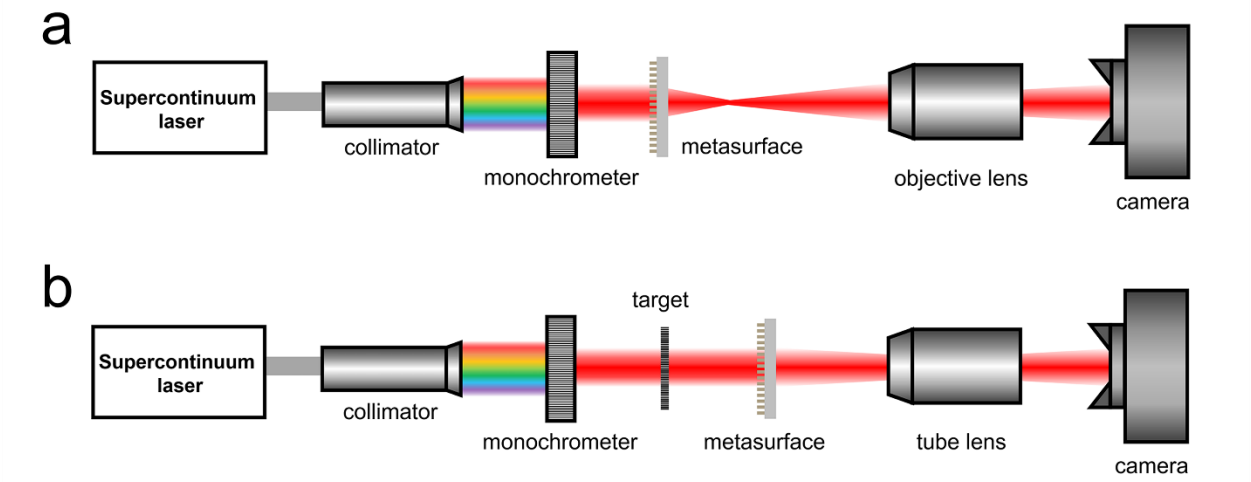

Figure D.2 Optical characterization setup. (a) The characterization setup for focal spot profile and hologram measurements. (b) The setup for imaging performance characterization with the USAF 1951 target sample.

In order to gauge the accuracy and precision of the fabrication technique, the optical properties and image performance of metalenses with *f*/5 and *f*/3 were characterized at a wavelength of 1.7μm. To achieve this characterization, we customized an optical measurement setup with the detailed diagram shown in Fig.D.2. This setup was built using a 20× objective (Mitutoyo Plan Apo, NA=0.4) for focal spot, hologram, and imaging performance characterization. Illumination was provided by a supercontinuum laser (Fianium WhiteLase) passing through a

monochromator (Cornerstone 130 1/8m). The light intensity was recorded by a NIR camera (Xeva-1.7-640) with background noise subtraction. Before recording the lateral focal spot profile and hologram, a standard test chart (USAF1951, R1DS1N, Thorlabs) was imaged to characterize the magnification of the optical system. To characterize the focal spot profile along the optical axis, the metalens was mounted on a translation stage with a step size of 10μm. With around 150 image slices obtained, the light intensity passing through the center of the focal spot at each image slice was rearranged along the propagating axis to form the profile image. The imaging characterization is based on the same optical system, with the USAF1951 standard test chart as the imaging target.

REFERENCES

(1) Shelby, R. A.; Smith, D. R.; Schultz, S. Experimental Verification of a Negative Index of Refraction. *Science.* **2001**, *292* (5514), 77–79.

(2) Zhang, S.; Fan, W.; Panoiu, N. C.; Malloy, K. J.; Osgood, R. M.; Brueck, S. R. J. Experimental Demonstration of Near-Infrared Negative-Index Metamaterials. *Phys. Rev. Lett.* **2005**, *95* (13), 1–4.

(3) Shalaev, V. M.; Cai, W.; Chettiar, U.; Yuan, H. K.; Sarychev, A. K.; Drachev, V. P.; Kildishev, A. V. Negative Index of Refraction in Optical Metamaterials. *Opt. InfoBase Conf. Pap.* **2005**, *30* (24), 3356–3358.

(4) Valentine, J.; Zhang, S.; Zentgraf, T.; Ulin-Avila, E.; Genov, D. A.; Bartal, G.; Zhang, X. Three-Dimensional Optical Metamaterial with a Negative Refractive Index. *Nature* **2008**, *455* (7211), 376–379.

(5) Silveirinha, M.; Engheta, N. Tunneling of Electromagnetic Energy through Subwavelength Channels and Bends Using ε-near-Zero Materials. *Phys. Rev. Lett.* **2006**, *97* (15), 1–4.

(6) Alù, A.; Silveirinha, M. G.; Salandrino, A.; Engheta, N. Epsilon-near-Zero Metamaterials and Electromagnetic Sources: Tailoring the Radiation Phase Pattern. *Phys. Rev. B - Condens. Matter Mater. Phys.* **2007**, *75* (15), 1–13.

(7) Liu, R.; Cheng, Q.; Hand, T.; Mock, J. J.; Cui, T. J.; Cummer, S. A.; Smith, D. R. Experimental Demonstration of Electromagnetic Tunneling through an Epsilon-near-Zero Metamaterial at Microwave Frequencies. *Phys. Rev. Lett.* **2008**, *100* (2), 1–4.

(8) Choi, M.; Lee, S. H.; Kim, Y.; Kang, S. B.; Shin, J.; Kwak, M. H.; Kang, K. Y.; Lee, Y. H.; Park, N.; Min, B. A Terahertz Metamaterial with Unnaturally High Refractive Index. *Nature* **2011**, *470* (7334), 369–373.

(9) Pendry, J. B. Negative Refraction Makes a Perfect Lens. *Phys. Rev. Lett.* **2000**, *85* (18), 3966–3969.

(10) Schurig, D.; Mock, J. J.; Justice, B. J.; Cummer, S. A.; Pendry, J. B.; Starr, A. F.; Smith, D. R. Metamaterial Electromagnetic Cloak at Microwave Frequencies. *Science.* **2006**, *314* (5801), 977–980.

(11) Valentine, J.; Li, J.; Zentgraf, T.; Bartal, G.; Zhang, X. An Optical Cloak Made of Dielectrics. *Nat. Mater.* **2009**, *8* (7), 568–571.

(12) Zhao, L.; Wang, J.; Liu, J.; Xu, Y.; Gu, B. L.; Xue, Q. K.; Duan, W. Electronic Analog of Chiral Metamaterial: Helicity-Resolved Filtering and Focusing of Dirac Fermions in Thin Films of Topological Materials. *Phys. Rev. B - Condens. Matter Mater. Phys.* **2015**, *92* (4), 1–5.

(13) Fernandez-Corbaton, I.; Rockstuhl, C.; Ziemke, P.; Gumbsch, P.; Albiez, A.; Schwaiger, R.; Frenzel, T.; Kadic, M.; Wegener, M. New Twists of 3D Chiral Metamaterials. *Adv. Mater.* **2019**, *31* (26), 1–7.

(14) She, A.; Zhang, S.; Shian, S.; Clarke, D. R.; Capasso, F. Large Area Metalenses: Design, Characterization, and Mass Manufacturing. *Opt. Express* **2018**, *26* (2), 1573.

(15) Park, J. S.; Zhang, S.; She, A.; Chen, W. T.; Lin, P.; Yousef, K. M. A.; Cheng, J. X.; Capasso, F. All-Glass, Large Metalens at Visible Wavelength Using Deep-Ultraviolet Projection Lithography. *Nano Lett.* **2019**, *19* (12), 8673–8682.

(16) Li, N.; Xu, Z.; Dong, Y.; Hu, T.; Zhong, Q.; Fu, Y. H.; Zhu, S.; Singh, N. Large-Area Metasurface on CMOS-Compatible Fabrication Platform: Driving Flat Optics from Lab to Fab. *Nanophotonics* **2020**, *9* (10), 3071–3087.

(17) Yu, N.; Genevet, P.; Kats, M. a; Aieta, F.; Tetienne, J.-P.; Capasso, F.; Gaburro, Z. Light Propagation with Phase Reflection and Refraction. *Science* . **2011**, *334* (October), 333–337.

(18) Khorasaninejad, M.; Chen, W. T.; Devlin, R. C.; Oh, J.; Zhu, A. Y.; Capasso, F. Metalenses at Visible Wavelengths: Diffraction-Limited Focusing and Subwavelength Resolution Imaging. *Science.* **2016**, *352* (6290), 1190–1194.

(19) Khorasaninejad, M.; Zhu, A. Y.; Roques-Carmes, C.; Chen, W. T.; Oh, J.; Mishra, I.; Devlin,

R. C.; Capasso, F. Polarization-Insensitive Metalenses at Visible Wavelengths. *Nano Lett.* **2016**, *16* (11), 7229–7234.

(20) Chen, W. T.; Zhu, A. Y.; Sisler, J.; Huang, Y. W.; Yousef, K. M. A.; Lee, E.; Qiu, C. W.; Capasso, F. Broadband Achromatic Metasurface-Refractive Optics. *Nano Lett.* **2018**, *18* (12), 7801–7808.

(21) Zhan, A.; Colburn, S.; Trivedi, R.; Fryett, T. K.; Dodson, C. M.; Majumdar, A. Low-Contrast Dielectric Metasurface Optics. *ACS Photonics* **2016**, *3* (2), 209–214.

(22) Fan, Z. Bin; Shao, Z. K.; Xie, M. Y.; Pang, X. N.; Ruan, W. S.; Zhao, F. L.; Chen, Y. J.; Yu, S. Y.; Dong, J. W. Silicon Nitride Metalenses for Unpolarized High-NA Visible Imaging. *2018 Conf. Lasers Electro-Optics, CLEO 2018 - Proc.* **2018**, *10* (1), 1.

(23) Fan, Z. Bin; Qiu, H. Y.; Zhang, H. Le; Pang, X. N.; Zhou, L. D.; Liu, L.; Ren, H.; Wang, Q. H.; Dong, J. W. A Broadband Achromatic Metalens Array for Integral Imaging in the Visible. *Light Sci. Appl.* **2019**, *8* (1).

(24) Arbabi, A.; Horie, Y.; Bagheri, M.; Faraon, A. Dielectric Metasurfaces for Complete Control of Phase and Polarization with Subwavelength Spatial Resolution and High Transmission. *Nat. Nanotechnol.* **2015**, *10* (11), 937–943.

(25) Kamali, S. M.; Arbabi, A.; Arbabi, E.; Horie, Y.; Faraon, A. Decoupling Optical Function and Geometrical Form Using Conformal Flexible Dielectric Metasurfaces. *Nat. Commun.* **2016**, *7* (May), 1–7.

(26) Kamali, S. M.; Arbabi, E.; Arbabi, A.; Horie, Y.; Faraji-Dana, M. S.; Faraon, A. Angle-Multiplexed Metasurfaces: Encoding Independent Wavefronts in a Single Metasurface under Different Illumination Angles. *Phys. Rev. X.* **2017**, *7* (4), 1–9.

(27) Decker, M.; Staude, I.; Falkner, M.; Dominguez, J.; Neshev, D. N.; Brener, I.; Pertsch, T.; Kivshar, Y. S. High-Efficiency Dielectric Huygens' Surfaces. *Adv. Opt. Mater.* **2015**, *3* (6), 813–820.

(28) Lalanne, P.; Astilean, S.; Chavel, P.; Cambril, E.; Launois, H. Blazed Binary

Subwavelength Gratings with Efficiencies Larger than Those of Conventional Échelette Gratings. *Opt. Lett.* **1998**, *23* (14), 1081.

(29) Lalanne, P.; Astilean, S.; Chavel, P.; Cambril, E.; Launois, H. Design and Fabrication of Blazed Binary Diffractive Elements with Sampling Periods Smaller than the Structural Cutoff. *J. Opt. Soc. Am. A.* **1999**, *16* (5), 1143.

(30) Lalanne, P. Waveguiding in Blazed-Binary Diffractive Elements. *J. Opt. Soc. Am. A.* **1999**, *16* (10), 2517.

(31) Arbabi, A.; Horie, Y.; Ball, A. J.; Bagheri, M.; Faraon, A. Subwavelength-Thick Lenses with High Numerical Apertures and Large Efficiency Based on High-Contrast Transmitarrays. *Nat. Commun.* **2015**, *6* (May), 2–7.

(32) Zhou, Y.; Kravchenko, I. I.; Wang, H.; Nolen, J. R.; Gu, G.; Valentine, J. Multilayer Noninteracting Dielectric Metasurfaces for Multiwavelength Metaoptics. *Nano Lett.* **2018**, *18* (12), 7529–7537.

(33) Liu, L.; Zhang, X.; Kenney, M.; Su, X.; Xu, N.; Ouyang, C.; Shi, Y.; Han, J.; Zhang, W.; Zhang, S. Broadband Metasurfaces with Simultaneous Control of Phase and Amplitude. *Adv. Mater.* **2014**, *26* (29), 5031–5036.

(34) Zhang, D.; Ren, M.; Wu, W.; Gao, N.; Yu, X.; Cai, W.; Zhang, X.; Xu, J. Nanoscale Beam Splitters Based on Gradient Metasurfaces. *Opt. Lett.* **2018**, *43* (2), 267.

(35) Zhang, X.; Deng, R.; Yang, F.; Jiang, C.; Xu, S.; Li, M. Metasurface-Based Ultrathin Beam Splitter with Variable Split Angle and Power Distribution. *ACS Photonics* **2018**, *5* (8), 2997–3002.

(36) Song, X.; Huang, L.; Tang, C.; Li, J.; Li, X.; Liu, J.; Wang, Y.; Zentgraf, T. Selective Diffraction with Complex Amplitude Modulation by Dielectric Metasurfaces. *Adv. Opt. Mater.* **2018**, *6* (4), 1–8.

(37) Song, Q.; Baroni, A.; Sawant, R.; Ni, P.; Brandli, V.; Chenot, S.; Vézian, S.; Damilano, B.; de Mierry, P.; Khadir, S.; Ferrand, P.; Genevet, P. Ptychography Retrieval of Fully

Polarized Holograms from Geometric-Phase Metasurfaces. *Nat. Commun.* **2020**, *11* (1), 1–8.

(38) Ni, X.; Kildishev, A. V.; Shalaev, V. M. Metasurface Holograms for Visible Light. *Nat. Commun.* **2013**, *4*.

(39) Zheng, G.; Mühlenbernd, H.; Kenney, M.; Li, G.; Zentgraf, T.; Zhang, S. Metasurface Holograms Reaching 80% Efficiency. *Nat. Nanotechnol.* **2015**, *10* (4), 308–312.

(40) Huang, L.; Chen, X.; Mühlenbernd, H.; Zhang, H.; Chen, S.; Bai, B.; Tan, Q.; Jin, G.; Cheah, K. W.; Qiu, C. W.; Li, J.; Zentgraf, T.; Zhang, S. Three-Dimensional Optical Holography Using a Plasmonic Metasurface. *Nat. Commun.* **2013**, *4* (May), 1–8.

(41) Huang, L.; Zhang, S.; Zentgraf, T. Metasurface Holography: From Fundamentals to Applications. *Nanophotonics* **2018**, *7* (6), 1169–1190.

(42) Lee, G. Y.; Hong, J. Y.; Hwang, S. H.; Moon, S.; Kang, H.; Jeon, S.; Kim, H.; Jeong, J. H.; Lee, B. Metasurface Eyepiece for Augmented Reality. *Nat. Commun.* **2018**, *9* (1), 1–10.

(43) Li, Z.; Lin, P.; Huang, Y. W.; Park, J. S.; Chen, W. T.; Shi, Z.; Qiu, C. W.; Cheng, J. X.; Capasso, F. Meta-Optics Achieves RGB-Achromatic Focusing for Virtual Reality. *Sci. Adv.* **2021**, *7* (5), 1–9.

(44) Joo, W. J.; Kyoung, J.; Esfandyarpour, M.; Lee, S. H.; Koo, H.; Song, S.; Kwon, Y. N.; Ho Song, S.; Bae, J. C.; Jo, A.; Kwon, M. J.; Han, S. H.; Kim, S. H.; Hwang, S.; Brongersma, M. L. Metasurface-Driven OLED Displays beyond 10,000 Pixels per Inch. *Science.* **2020**, *370* (6515), 459–463.

(45) Zhao, R.; Sain, B.; Wei, Q.; Tang, C.; Li, X.; Weiss, T.; Huang, L.; Wang, Y.; Zentgraf, T. Multichannel Vectorial Holographic Display and Encryption. *Light Sci. Appl.* **2018**, *7* (1).

(46) Zhou, Y.; Zheng, H.; Kravchenko, I. I.; Valentine, J. Flat Optics for Image Differentiation. *Nat. Photonics* **2020**, *14* (5), 316–323.

(47) Zhu, T.; Zhou, Y.; Lou, Y.; Ye, H.; Qiu, M.; Ruan, Z.; Fan, S. Plasmonic Computing of

Spatial Differentiation. *Nat. Commun.* **2017**, *8* (May), 1–6.

(48) Guo, C.; Xiao, M.; Minkov, M.; Shi, Y.; Fan, S. Photonic Crystal Slab Laplace Operator for Image Differentiation. *Optica* **2018**, *5* (3), 251.

(49) Faraji-Dana, M. S.; Arbabi, E.; Arbabi, A.; Kamali, S. M.; Kwon, H.; Faraon, A. Compact Folded Metasurface Spectrometer. *Nat. Commun.* **2018**, *9* (1).

(50) Reshef, O.; DelMastro, M. P.; Bearne, K. K. M.; Alhulaymi, A. H.; Giner, L.; Boyd, R. W.; Lundeen, J. S. An Optic to Replace Space and Its Application towards Ultra-Thin Imaging Systems. *Nat. Commun.* **2021**, *12* (1), 8–15.

(51) Sell, D.; Yang, J.; Doshay, S.; Yang, R.; Fan, J. A. Large-Angle, Multifunctional Metagratings Based on Freeform Multimode Geometries. *Nano Lett.* **2017**, *17* (6), 3752–3757.

(52) Zhou, M.; Liu, D.; Belling, S. W.; Cheng, H.; Kats, M. A.; Fan, S.; Povinelli, M. L.; Yu, Z. Inverse Design of Metasurfaces Based on Coupled-Mode Theory and Adjoint Optimization. *ACS Photonics* **2021**, *8* (8), 2265–2273.

(53) Zhu, R.; Qiu, T.; Wang, J.; Sui, S.; Hao, C.; Liu, T.; Li, Y.; Feng, M.; Zhang, A.; Qiu, C. W.; Qu, S. Phase-to-Pattern Inverse Design Paradigm for Fast Realization of Functional Metasurfaces via Transfer Learning. *Nat. Commun.* **2021**, *12* (1).

(54) Li, Z.; Pestourie, R.; Park, J. S.; Huang, Y. W.; Johnson, S. G.; Capasso, F. Inverse Design Enables Large-Scale High-Performance Meta-Optics Reshaping Virtual Reality. *Nat. Commun.* **2022**, *13* (1), 1–11.

(55) Li, Z.; Pestourie, R.; Lin, Z.; Johnson, S. G.; Capasso, F. Empowering Metasurfaces with Inverse Design: Principles and Applications. *ACS Photonics* **2022**, *9* (7), 2178–2192.

(56) Shrestha, S.; Overvig, A. C.; Lu, M.; Stein, A.; Yu, N. Broadband Achromatic Dielectric Metalenses. *Light Sci. Appl.* **2018**, *7* (1).

(57) Kim, W.; Yoon, G.; Kim, J.; Jeong, H.; Kim, Y.; Choi, H.; Badloe, T.; Rho, J.; Lee, H.

Thermally-Curable Nanocomposite Printing for the Scalable Manufacturing of Dielectric Metasurfaces. *Microsystems Nanoeng.* **2022**, *8* (1).

(58) Huang, X.; Yuan, W.; Holman, A.; Kwon, M.; Masson, S. J.; Gutierrez-Jauregui, R.; Asenjo-Garcia, A.; Will, S.; Yu, N. Metasurface Holographic Optical Traps for Ultracold Atoms. *arXiv*. **2022**, 1–36.

(59) Overvig, A. C.; Shrestha, S.; Malek, S. C.; Lu, M.; Stein, A.; Zheng, C.; Yu, N. Dielectric Metasurfaces for Complete and Independent Control of the Optical Amplitude and Phase. *Light Sci. Appl.* **2019**, *8* (1).

(60) Song, Q.; Liu, X.; Qiu, C. W.; Genevet, P. Vectorial Metasurface Holography. *Appl. Phys. Rev.* **2022**, *9* (1).

(61) Khorasaninejad, M.; Chen, W. T.; Zhu, A. Y.; Oh, J.; Devlin, R. C.; Rousso, D.; Capasso, F. Multispectral Chiral Imaging with a Metalens. *Nano Lett.* **2016**, *16* (7), 4595–4600.

(62) Tanaka, K.; Arslan, D.; Fasold, S.; Steinert, M.; Ju.rgen Sautter; Falkner, M.; Pertsch, T.; Decker, M.; Staude, I. Chiral Bilayer All-Dielectric Metasurfaces. *ACS Nano* **2020**, *14* (11), 15926–15935.

(63) Arbabi, E.; Kamali, S. M.; Arbabi, A.; Faraon, A. Full-Stokes Imaging Polarimetry Using Dielectric Metasurfaces. *ACS Photonics* **2018**, *5* (8), 3132–3140.

(64) Arbabi, A.; Arbabi, E.; Kamali, S. M.; Horie, Y.; Han, S.; Faraon, A. Miniature Optical Planar Camera Based on a Wide-Angle Metasurface Doublet Corrected for Monochromatic Aberrations. *Nat. Commun.* **2016**, *7*, 1–9.

(65) Zhou, Y.; Kravchenko, I. I.; Wang, H.; Zheng, H.; Gu, G.; Valentine, J. Multifunctional Metaoptics Based on Bilayer Metasurfaces. *Light Sci. Appl.* **2019**, *8* (1).

(66) Kwon, H.; Arbabi, E.; Kamali, S. M.; Faraji-Dana, M. S.; Faraon, A. Single-Shot Quantitative Phase Gradient Microscopy Using a System of Multifunctional Metasurfaces. *Nat. Photonics* **2020**, *14* (2), 109–114.

(67) Yu, N.; Capasso, F. Flat Optics with Designer Metasurfaces. *Nat. Mater.* **2014**, *13* (2), 139–150.

(68) Staude, I.; Schilling, J. Metamaterial-Inspired Silicon Nanophotonics. *Nat. Photonics* **2017**, *11* (5), 274–284.

(69) He, Q.; Sun, S.; Xiao, S.; Zhou, L. High-Efficiency Metasurfaces: Principles, Realizations, and Applications. *Adv. Opt. Mater.* **2018**, *6* (19), 1–23.

(70) Kamali, S. M.; Arbabi, E.; Arbabi, A.; Faraon, A. A Review of Dielectric Optical Metasurfaces for Wavefront Control. *Nanophotonics* **2018**, *7* (6), 1041–1068.

(71) Lee, G. Y.; Yoon, G.; Lee, S. Y.; Yun, H.; Cho, J.; Lee, K.; Kim, H.; Rho, J.; Lee, B. Complete Amplitude and Phase Control of Light Using Broadband Holographic Metasurfaces. *Nanoscale* **2018**, *10* (9), 4237–4245.

(72) Ren, H.; Fang, X.; Jang, J.; Bürger, J.; Rho, J.; Maier, S. A. Complex-Amplitude Metasurface-Based Orbital Angular Momentum Holography in Momentum Space. *Nat. Nanotechnol.* **2020**, *15* (11), 948–955.

(73) Wang, Q.; Zhang, X.; Xu, Y.; Gu, J.; Li, Y.; Tian, Z.; Singh, R.; Zhang, S.; Han, J.; Zhang, W. Broadband Metasurface Holograms: Toward Complete Phase and Amplitude Engineering. *Sci. Rep.* **2016**, *6*, 4–13.

(74) Lung, S.; Wang, K.; Kamali, K. Z.; Zhang, J.; Rahmani, M.; Neshev, D. N.; Sukhorukov, A. A. Complex-Birefringent Dielectric Metasurfaces for Arbitrary Polarization-Pair Transformations. *ACS Photonics* **2020**, *7* (11), 3015–3022.

(75) Zhou, Y.; Kravchenko, I. I.; Wang, H.; Zheng, H.; Gu, G.; Valentine, J. Multifunctional Metaoptics Based on Bilayer Metasurfaces. *Light Sci. Appl.* **2019**, *8* (1).

(76) Ansouree, M. A. M.; Won, H. Y. K.; Rbabi, E. H. A.; Ndrew, A.; Lung, M. C. C.; Araon, A. N. F.; Rbabi, A. M. I. R. A. Multifunctional 2.5D Metastructures Enabled by Adjoint Optimization. *Optica* **2020**, *i* (1), 1–11.

(77) Raeker, B. O.; Grbic, A. Lossless Complex-Valued Optical-Field Control with Compound Metaoptics. *Phys. Rev. Appl.* **2021**, *15* (5), 1–13.

(78) Raeker, B. O.; Grbic, A. Compound Metaoptics for Amplitude and Phase Control of Wave Fronts. *Phys. Rev. Lett.* **2019**, *122* (11), 113901.

(79) Kruk, S.; Ferreira, F.; Mac Suibhne, N.; Tsekrekos, C.; Kravchenko, I.; Ellis, A.; Neshev, D.; Turitsyn, S.; Kivshar, Y. Transparent Dielectric Metasurfaces for Spatial Mode Multiplexing. *Laser Photonics Rev.* **2018**, *12* (8), 1–5.

(80) Nazemosadat, E.; Mazur, M.; Kruk, S.; Kravchenko, I.; Carpenter, J.; Schröder, J.; Andrekson, P. A.; Karlsson, M.; Kivshar, Y. Dielectric Broadband Metasurfaces for Fiber Mode-Multiplexed Communications. *Adv. Opt. Mater.* **2019**, *7* (14), 1–7.

(81) Xie, Y. Y.; Ni, P. N.; Wang, Q. H.; Kan, Q.; Briere, G.; Chen, P. P.; Zhao, Z. Z.; Delga, A.; Ren, H. R.; Chen, H. Da; Xu, C.; Genevet, P. Metasurface-Integrated Vertical Cavity Surface-Emitting Lasers for Programmable Directional Lasing Emissions. *Nat. Nanotechnol.* **2020**, *15* (February).

(82) Liu, W.; Yang, Q.; Xu, Q.; Jiang, X.; Wu, T.; Wang, K.; Gu, J.; Han, J.; Zhang, W. Multifunctional All-Dielectric Metasurfaces for Terahertz Multiplexing. *Adv. Opt. Mater.* **2021**, *9* (19), 1–8.

(83) Raeker, B. O.; Zheng, H.; Zhou, Y.; Kravchenko, I. I.; Valentine, J.; Grbic, A. All-Dielectric Meta-Optics for High-Efficiency Independent Amplitude and Phase Manipulation. *Adv. Photonics Res.* **2022**, *3* (3), 2100285.

(84) Kingma, D. P.; Ba, J. L. Adam: A Method for Stochastic Optimization. *3rd Int. Conf. Learn. Represent. ICLR 2015 - Conf. Track Proc.* **2015**, 1–15.

(85) Kulce, O.; Mengu, D.; Rivenson, Y.; Ozcan, A. All-Optical Synthesis of an Arbitrary Linear Transformation Using Diffractive Surfaces. *Light Sci. Appl.* **2021**, *10* (1).

(86) Arbabi, E.; Kamali, S. M.; Arbabi, A.; Faraon, A. Vectorial Holograms with a Dielectric Metasurface: Ultimate Polarization Pattern Generation. *ACS Photonics* **2019**, *6* (11), 2712–

2718.

(87) Wen, D.; Cadusch, J. J.; Meng, J.; Crozier, K. B. Vectorial Holograms with Spatially Continuous Polarization Distributions. *Nano Lett.* **2021**, *21* (4), 1735–1741.

(88) Zheng, H.; Liu, Q.; Zhou, Y.; Kravchenko, I. I.; Huo, Y.; Valentine, J. Meta-Optic Accelerators for Object Classifiers. *Sci. Adv.* **2022**, *6410* (July), 1–9.

(89) Stav, T.; Faerman, A.; Maguid, E.; Oren, D.; Kleiner, V.; Hasman, E.; Segev, M. Quantum Entanglement of the Spin and Orbital Angular Momentum of Photons Using Metamaterials. *Science.* **2018**, *361* (6407), 1101–1104.

(90) Georgi, P.; Qunshuo, W.; Sain, B.; Schlickriede, C.; Wang, Y.; Huang, L.; Zentgraf, T. Cascaded Metasurface Holograms for Optical Secret Sharing. *Sci. Adv.* **2021**, *7* (7), 1–5.

(91) Kim, I.; Jang, J.; Kim, G.; Lee, J.; Badloe, T.; Mun, J.; Rho, J. Pixelated Bifunctional Metasurface-Driven Dynamic Vectorial Holographic Color Prints for Photonic Security Platform. *Nat. Commun.* **2021**, *12* (1), 1–9.

(92) Simonyan, K.; Zisserman, A. Very Deep Convolutional Networks for Large-Scale Image Recognition. *3rd Int. Conf. Learn. Represent. ICLR 2015 - Conf. Track Proc.* **2015**, 1–14.

(93) Wang, G.; Li, W.; Zuluaga, M. A.; Pratt, R.; Patel, P. A.; Aertsen, M.; Doel, T.; David, A. L.; Deprest, J.; Ourselin, S.; Vercauteren, T. Interactive Medical Image Segmentation Using Deep Learning with Image-Specific Fine Tuning. *IEEE Trans. Med. Imaging* **2018**, *37* (7), 1562–1573.

(94) Furui, S.; Deng, L.; Gales, M.; Ney, H.; Tokuda, K. Fundamental Technologies in Modern Speech Recognition. *IEEE Signal Process. Mag.* **2012**, *29* (6), 16–17.

(95) Sak, H.; Senior, A.; Rao, K.; Beaufays, F. Fast and Accurate Recurrent Neural Network Acoustic Models for Speech Recognition. *Proc. Annu. Conf. Int. Speech Commun. Assoc. INTERSPEECH* **2015**, *2015-Janua*, 1468–1472.

(96) Devlin, J.; Chang, M. W.; Lee, K.; Toutanova, K. BERT: Pre-Training of Deep

Bidirectional Transformers for Language Understanding. *NAACL HLT 2019 - 2019 Conf. North Am. Chapter Assoc. Comput. Linguist. Hum. Lang. Technol. - Proc. Conf.* **2019**, *1* (Mlm), 4171–4186.

(97) Lecun, Y.; Bengio, Y.; Hinton, G. Deep Learning. *Nature* **2015**, *521* (7553), 436–444.

(98) Wetzstein, G.; Ozcan, A.; Gigan, S.; Fan, S.; Englund, D.; Soljačić, M.; Denz, C.; Miller, D. A. B.; Psaltis, D. Inference in Artificial Intelligence with Deep Optics and Photonics. *Nature* **2020**, *588* (7836), 39–47.

(99) Shastri, B. J.; Tait, A. N.; Ferreira de Lima, T.; Pernice, W. H. P.; Bhaskaran, H.; Wright, C. D.; Prucnal, P. R. Photonics for Artificial Intelligence and Neuromorphic Computing. *Nat. Photonics* **2021**, *15* (2), 102–114.

(100) Wang, T.; Ma, S.-Y.; Wright, L. G.; Onodera, T.; Richard, B.; McMahon, P. L. An Optical Neural Network Using Less than 1 Photon per Multiplication. *arXiv*. **2021**, No. 2022, 1–8.

(101) Xu, X.; Tan, M.; Corcoran, B.; Wu, J.; Boes, A.; Nguyen, T. G.; Chu, S. T.; Little, B. E.; Hicks, D. G.; Morandotti, R.; Mitchell, A.; Moss, D. J. 11 TOPS Photonic Convolutional Accelerator for Optical Neural Networks. *Nature* **2021**, *589* (7840), 44–51.

(102) Feldmann, J.; Youngblood, N.; Karpov, M.; Gehring, H.; Li, X.; Stappers, M.; Le Gallo, M.; Fu, X.; Lukashchuk, A.; Raja, A. S.; Liu, J.; Wright, C. D.; Sebastian, A.; Kippenberg, T. J.; Pernice, W. H. P.; Bhaskaran, H. Parallel Convolutional Processing Using an Integrated Photonic Tensor Core. *Nature* **2021**, *589* (7840), 52–58.

(103) Chen, Y. H.; Krishna, T.; Emer, J. S.; Sze, V. Eyeriss: An Energy-Efficient Reconfigurable Accelerator for Deep Convolutional Neural Networks. *IEEE J. Solid-State Circuits* **2017**, *52* (1), 127–138.

(104) Neshatpour, K.; Homayoun, H.; Sasan, A. ICNN: The Iterative Convolutional Neural Network. *ACM Trans. Embed. Comput. Syst.* **2019**, *18* (6).

(105) Hamerly, R.; Bernstein, L.; Sludds, A.; Soljačić, M.; Englund, D. Large-Scale Optical Neural Networks Based on Photoelectric Multiplication. *Phys. Rev. X* **2019**, *9* (2), 1–12.

(106) Mennel, L.; Symonowicz, J.; Wachter, S.; Polyushkin, D. K.; Molina-Mendoza, A. J.; Mueller, T. Ultrafast Machine Vision with 2D Material Neural Network Image Sensors. *Nature* **2020**, *579* (7797), 62–66.

(107) del Hougne, P.; Imani, M. F.; Diebold, A. V.; Horstmeyer, R.; Smith, D. R. Learned Integrated Sensing Pipeline: Reconfigurable Metasurface Transceivers as Trainable Physical Layer in an Artificial Neural Network. *Adv. Sci.* **2020**, *7* (3), 1–8.

(108) Wu, C.; Yu, H.; Lee, S.; Peng, R.; Takeuchi, I.; Li, M. Programmable Phase-Change Metasurfaces on Waveguides for Multimode Photonic Convolutional Neural Network. *Nat. Commun.* **2021**, *12* (1), 1–8.

(109) Zhang, H.; Gu, M.; Jiang, X. D.; Thompson, J.; Cai, H.; Paesani, S.; Santagati, R.; Laing, A.; Zhang, Y.; Yung, M. H.; Shi, Y. Z.; Muhammad, F. K.; Lo, G. Q.; Luo, X. S.; Dong, B.; Kwong, D. L.; Kwek, L. C.; Liu, A. Q. An Optical Neural Chip for Implementing Complex-Valued Neural Network. *Nat. Commun.* **2021**, *12* (1), 1–11.

(110) Wang, X.; Diáz-Rubio, A.; Tretyakov, S. A. Independent Control of Multiple Channels in Metasurface Devices. *Phys. Rev. Appl.* **2020**, *14* (2), 1.

(111) Lin, Z.; Pestourie, R.; Roques-Carmes, C.; Li, Z.; Capasso, F.; Soljačić, M.; Johnson, S. G. End-to-End Metasurface Inverse Design for Single-Shot Multi-Channel Imaging. *ArXiv*. **2021**, 1–17.

(112) Li, L.; Wang, J.; Kang, L.; Liu, W.; Yu, L.; Zheng, B.; Brongersma, M. L.; Werner, D. H.; Lan, S.; Shi, Y.; Xu, Y.; Wang, X. Monolithic Full-Stokes Near-Infrared Polarimetry with Chiral Plasmonic Metasurface Integrated Graphene-Silicon Photodetector. *ACS Nano* **2020**, *14* (12), 16634–16642.

(113) Chang, J.; Sitzmann, V.; Dun, X.; Heidrich, W.; Wetzstein, G. Hybrid Optical-Electronic Convolutional Neural Networks with Optimized Diffractive Optics for Image Classification. *Sci. Rep.* **2018**, *8* (1), 1–10.

(114) Yan, T.; Wu, J.; Zhou, T.; Xie, H.; Xu, F.; Fan, J.; Fang, L.; Lin, X.; Dai, Q. Fourier-Space Diffractive Deep Neural Network. *Phys. Rev. Lett.* **2019**, *123* (2), 23901.

(115) Colburn, S.; Chu, Y.; Shilzerman, E.; Majumdar, A. Optical Frontend for a Convolutional Neural Network. *Appl. Opt.* **2019**, *58* (12), 3179.

(116) Zhou, T.; Lin, X.; Wu, J.; Chen, Y.; Xie, H.; Li, Y.; Fan, J.; Wu, H.; Fang, L.; Dai, Q. Large-Scale Neuromorphic Optoelectronic Computing with a Reconfigurable Diffractive Processing Unit. *Nat. Photonics* **2021**, *15* (5), 367–373.

(117) Lin, X.; Rivenson, Y.; Yardimci, N. T.; Veli, M.; Luo, Y.; Jarrahi, M.; Ozcan, A. All-Optical Machine Learning Using Diffractive Deep Neural Networks. *Science.* **2018**, *361* (6406), 1004–1008.

(118) Qian, C.; Lin, X.; Lin, X.; Xu, J.; Sun, Y.; Li, E.; Zhang, B.; Chen, H. Performing Optical Logic Operations by a Diffractive Neural Network. *Light Sci. Appl.* **2020**, *9* (1).

(119) Luo, X.; Hu, Y.; Li, X.; Ou, X.; Lai, J.; Liu, N. Metasurface-Enabled On-Chip Multiplexed Diffractive Neural Networks in the Visible. *arXiv*. **2022**

(120) Rubin, N. A.; D'Aversa, G.; Chevalier, P.; Shi, Z.; Chen, W. T.; Capasso, F. Matrix Fourier Optics Enables a Compact Full-Stokes Polarization Camera. *Science.* **2019**, *364* (6448).

(121) Shalaev, M. I.; Sun, J.; Tsukernik, A.; Pandey, A.; Nikolskiy, K.; Litchinitser, N. M. High-Efficiency All-Dielectric Metasurfaces for Ultracompact Beam Manipulation in Transmission Mode. *Nano Lett.* **2015**, *15* (9), 6261–6266.

(122) Yu, Y. F.; Zhu, A. Y.; Paniagua-Domínguez, R.; Fu, Y. H.; Luk'yanchuk, B.; Kuznetsov, A. I. High-Transmission Dielectric Metasurface with 2π Phase Control at Visible Wavelengths. *Laser Photonics Rev.* **2015**, *9* (4), 412–418.

(123) Cordaro, A.; Kwon, H.; Sounas, D.; Koenderink, A. F.; Alù, A.; Polman, A. High-Index Dielectric Metasurfaces Performing Mathematical Operations. *Nano Lett.* **2019**, *19* (12), 8418–8423.

(124) Zhou, J.; Qian, H.; Chen, C. F.; Zhao, J.; Li, G.; Wu, Q.; Luo, H.; Wen, S.; Liu, Z. Optical Edge Detection Based on High-Efficiency Dielectric Metasurface. *Proc. Natl. Acad. Sci. U. S. A.* **2019**, *166* (23), 11137–11140.

(125) Leitis, A.; Tittl, A.; Liu, M.; Lee, B. H.; Gu, M. B.; Kivshar, Y. S.; Altug, H. Angle-Multiplexed All-Dielectric Metasurfaces for Broadband Molecular Fingerprint Retrieval. *Sci. Adv.* **2019**, *5* (5), 1–9.

(126) Yesilkoy, F.; Arvelo, E. R.; Jahani, Y.; Liu, M.; Tittl, A.; Cevher, V.; Kivshar, Y.; Altug, H. Ultrasensitive Hyperspectral Imaging and Biodetection Enabled by Dielectric Metasurfaces. *Nat. Photonics* **2019**, *13* (6), 390–396.

(127) Zhang, L.; Ding, J.; Zheng, H.; An, S.; Lin, H.; Zheng, B.; Du, Q.; Yin, G.; Michon, J.; Zhang, Y.; Fang, Z.; Shalaginov, M. Y.; Deng, L.; Gu, T.; Zhang, H.; Hu, J. Ultra-Thin High-Efficiency Mid-Infrared Transmissive Huygens Meta-Optics. *Nat. Commun.* **2018**, *9* (1), 1–9.

(128) Vieu, C.; Carcenac, F.; Pépin, A.; Chen, Y.; Mejias, M.; Lebib, A.; Manin-Ferlazzo, L.; Couraud, L.; Launois, H. Electron Beam Lithography: Resolution Limits and Applications. *Appl. Surf. Sci.* **2000**, *164* (1–4), 111–117.

(129) Fay, B. Advanced Optical Lithography Development, from UV to EUV. *Microelectron. Eng.* **2002**, *61–62*, 11–24.

(130) She, A.; Zhang, S.; Shian, S.; Clarke, D. R.; Capasso, F. Large Area Metalenses: Design, Characterization, and Mass Manufacturing. *arXiv* **2017**, *26* (2), 1190–1194.

(131) Mai, Y.; Eisenberg, A. Self-Assembly of Block Copolymers. *Chem. Soc. Rev.* **2012**, *41* (18), 5969–5985.

(132) Yan, H.; Park, S. H.; Finkelstein, G.; Reif, J. H.; LaBean, T. H. DNA-Templated Self-Assembly of Protein Arrays and Highly Conductive Nanowires. *Science.* **2003**, *301* (5641), 1882–1884.

(133) Reches, M.; Gazit, E. Casting Metal Nanowires within Discrete Self-Assembled Peptide Nanotubes. *Science.* **2003**, *300* (5619), 625–627.

(134) Haynes, C. L.; Van Duyne, R. P. Nanosphere Lithography: A Versatile Nanofabrication Tool for Studies of Size-Dependent Nanoparticle Optics. *J. Phys. Chem. B* **2001**, *105* (24),

5599–5611.

(135) Kosiorek, A.; Kandulski, W.; Glaczynska, H.; Giersig, M. Fabrication of Nanoscale Rings, Dots, and Rods by Combining Shadow Nanosphere Lithography and Annealed Polystyrene Nanosphere Masks. *Small* **2005**, *1* (4), 439–444.

(136) Kosiorek, A.; Kandulski, W.; Chudzinski, P.; Kempa, K.; Giersig, M. Shadow Nanosphere Lithography: Simulation and Experiment. *Nano Lett.* **2004**, *4* (7), 1359–1363.

(137) Zheng, H.; Zhou, Y.; Ugwu, C. F.; Du, A.; Kravchenko, I. I.; Valentine, J. G. Large-Scale Metasurfaces Based on Grayscale Nanosphere Lithography. *ACS Photonics* **2021**, *8* (6), 1824–1831.

(138) Bonakdar, A.; Rezaei, M.; Brown, R. L.; Fathipour, V.; Dexheimer, E.; Jang, S. J.; Mohseni, H. Deep-UV Microsphere Projection Lithography. *Opt. Lett.* **2015**, *40* (11), 2537.

(139) McGorty, R.; Fung, J.; Kaz, D.; Manoharan, V. N. Colloidal Self-Assembly at an Interface. *Mater. Today* **2010**, *13* (6), 34–42.

(140) Zhang, J.; Li, Y.; Zhang, X.; Yang, B. Colloidal Self-Assembly Meets Nanofabrication: From Two-Dimensional Colloidal Crystals to Nanostructure Arrays. *Adv. Mater.* **2010**, *22* (38), 4249–4269.

(141) Meng, X.; Qiu, D. Gas-Flow-Induced Reorientation to Centimeter-Sized Two-Dimensional Colloidal Single Crystal of Polystyrene Particle. *Langmuir* **2014**, *30* (11), 3019–3023.

(142) Stavroulakis, P. I.; Christou, N.; Bagnall, D. Improved Deposition of Large Scale Ordered Nanosphere Monolayers via Liquid Surface Self-Assembly. *Mater. Sci. Eng. B Solid-State Mater. Adv. Technol.* **2009**, *165* (3), 186–189.

(143) Moitra, P.; Slovick, B. A.; Li, W.; Kravchencko, I. I.; Briggs, D. P.; Krishnamurthy, S.; Valentine, J. Large-Scale All-Dielectric Metamaterial Perfect Reflectors. *ACS Photonics* **2015**, *2* (6), 692–698.

(144) Gwinner, M. C.; Koroknay, E.; Liwei, F.; Patoka, P.; Kandulski, W.; Giersig, M.; Giessen,

H. Periodic Large-Area Metallic Split-Ring Resonator Metamaterial Fabrication Based on Shadow Nanosphere Lithography. *Small* **2009**, *5* (3), 400–406.

(145) Walter, R.; Tittl, A.; Berrier, A.; Sterl, F.; Weiss, T.; Giessen, H. Large-Area Low-Cost Tunable Plasmonic Perfect Absorber in the near Infrared by Colloidal Etching Lithography. *Adv. Opt. Mater.* **2015**, *3* (3), 398–403.

(146) Qu, C.; Kinzel, E. C. Polycrystalline Metasurface Perfect Absorbers Fabricated Using Microsphere Photolithography. *Opt. Lett.* **2016**, *41* (15), 3399.

(147) Han, S.; Hao, Z.; Wang, J.; Luo, Y. Controllable Two-Dimensional Photonic Crystal Patterns Fabricated by Nanosphere Lithography. *J. Vac. Sci. Technol. B Microelectron. Nanom. Struct.* **2005**, *23* (4), 1585.

(148) Oh, J. R.; Moon, J. H.; Yoon, S.; Park, C. R.; Do, Y. R. Fabrication of Wafer-Scale Polystyrene Photonic Crystal Multilayers via the Layer-by-Layer Scooping Transfer Technique. *J. Mater. Chem.* **2011**, *21* (37), 14167–14172..

(149) Gonidec, M.; Hamedi, M. M.; Nemiroski, A.; Rubio, L. M.; Torres, C.; Whitesides, G. M. Fabrication of Nonperiodic Metasurfaces by Microlens Projection Lithography. *Nano Lett.* **2016**, *16* (7), 4125–4132.

(150) Dudley, D.; Duncan, W. M.; Slaughter, J. Emerging Digital Micromirror Device (DMD) Applications. *MOEMS Disp. Imaging Syst.* **2003**, *4985* (January 2003), 14.

(151) Rammohan, A.; Dwivedi, P. K.; Martinez-Duarte, R.; Katepalli, H.; Madou, M. J.; Sharma, A. One-Step Maskless Grayscale Lithography for the Fabrication of 3-Dimensional Structures in SU-8. *Sensors Actuators, B Chem.* **2011**, *153* (1), 125–134.

(152) Sun, C.; Fang, N.; Wu, D. M.; Zhang, X. Projection Micro-Stereolithography Using Digital Micro-Mirror Dynamic Mask. *Sensors Actuators, A Phys.* **2005**, *121* (1), 113–120.

(153) Ye, X.; Huang, J.; Zeng, Y.; Sun, L. X.; Geng, F.; Liu, H. J.; Wang, F. R.; Jiang, X. D.; Wu, W. D.; Zheng, W. G. Monolayer Colloidal Crystals by Modified Air-Water Interface Self-Assembly Approach. *Nanomaterials* **2017**, *7* (10), 1–11.

(154) Zhang, C.; Cvetanovic, S.; Pearce, J. M. Fabricating Ordered 2-D Nano-Structured Arrays Using Nanosphere Lithography. *MethodsX* **2017**, *4*, 229–242.

(155) Parchine, M.; McGrath, J.; Bardosova, M.; Pemble, M. E. Large Area 2D and 3D Colloidal Photonic Crystals Fabricated by a Roll-to-Roll Langmuir-Blodgett Method. *Langmuir* **2016**, *32* (23), 5862–5869.

(156) Gao, P.; He, J.; Zhou, S.; Yang, X.; Li, S.; Sheng, J.; Wang, D.; Yu, T.; Ye, J.; Cui, Y. Large-Area Nanosphere Self-Assembly by a Micro-Propulsive Injection Method for High Throughput Periodic Surface Nanotexturing. *Nano Lett.* **2015**, *15* (7), 4591–4598.